QUANTUM ENGINEERING IN DIAMOND

A Dissertation

by

JESON CHEN

Submitted to the Office of Graduate and Professional Studies of
Texas A&M University
in partial fulfillment of the requirements for the degree of

DOCTOR OF PHILOSOPHY

Chair of Committee,	Philip Hemmer
Co-Chair of Committee,	Alexei Sokolov
Committee Members,	Edward Fry
	Joseph Ross
Head of Department,	George R. Welch

August 2015

Major Subject: Physics

ABSTRACT

Solid-state technologies for quantum mechanical application require delicate materials that can operate stably with a long coherence time. Nitrogen vacancy (NV) centers in diamond is one of the most promising candidates for quantum physics, with applications such as single photon emitters, quantum computation, and magnetic sensor.

To fully exploit the capability of defect centers in diamond for opto-electronics and quantum engineering, a number of improvements are needed. Among these are optimization of the NV centers yield in bulk diamond, nanodiamond (ND) size reduction, photocurrent study of the defect band-trap electronic structure in diamonds, and optimization of high-speed NV qubit control. For NV centers yield optimization, both the experimental magnetic sensitivity optimization as well as theoretical simulation of NV concentration are implemented. For NDs size characterization, we analyzed the size and photon autocorrelation function of NV in NDs after air oxidation treatment using a combined atomic force microscopy/confocal system. To study defect band-trap electronic structure in diamond, excitation and quenching as well as the recovery of the quenched photocurrent was investigated to better understand photocurrent dynamics in diamond. For qubit high-speed control optimization, a microwave pulse based on a nonlinear numeric solution of the Schrodinger equation is used to rotate the NV spin faster than the ordinary Rabi flip rate. Together these approaches promise to significantly speed up the development of diamond for quantum engineering applications.

ACKNOWLEDGEMENTS

I would like to thank my advisor Dr. Hemmer for his guidance, patience, and support for my graduate research. I would also want to thank my committee co-chairs, Dr. Alexei Sokolov, my committee members, Dr. Joseph Ross, and to Dr. Edward Fry, and research cooperation partners, Dr. Andrejs Jarmola, Dr. Boris Naydenov, Dr. Charles Santori, Dr. Dmitry Budker, Dr. Fedor Jelezko, Dr. James Rabeau, Dr. Jorg Wrachtrup, Dr. Jan Mejier, Louis Bouchard, Dr. Milos Nesladek, Dr. Torsten Gabeau, Alexander Petrajtis, Carlo Bradac, Kristine Rezai, Pauli Kehayias, for their help and suggestion throughout the course of this research. Thanks also go to my friends and colleagues and the department faculty and staff for making my time at Texas A&M University a great experience.

Finally, I want to thank my family. I could not have accomplished my degree without their love and patience. I want to thank my grandparents for raising me up in a warm and stable house. Their optimism always inspire me. I want to thanks my aunts and uncles for their teaching, counseling, and unconditional support. They nurture me with their positive characters. I also want to thank my parents-in-law for their understanding and encouragement. Last but not least, I want to thank my wife Cathy for her support and care. She always stands by my side and gives me wise suggestions. My life in graduate school becomes colorful after meeting her. I am blessed to have met her at Texas A&M University.

NOMENCLATURE

AFM   Atomic Force Microscopy

APD   Avalanche Photodiode

CCD   Charge Coupled Device

CVD   Chemical Vapor Deposition

CW   Continuous Wave

DC   Direct Current

ESR   Electron Spin Resonance

FID   Free Induction Decay

HBT   Hanbury Brown and Twiss

MW   Microwave

ND   Nanodiamond

NV   Nitrogen Vacancy Center (negatively charged)

ODMR   Optical Detected Magnetic Resonance

Qubit   Quantum bit

TEM   Transmission Electron Microscopy

T1   Spin-Lattice Relaxation Time

T2   Spin-spin Relaxation Time

ZFS   Zero Field Splitting

TABLE OF CONTENTS

Page

LIST OF FIGURES

LIST OF TABLES

CHAPTER I

INTRODUCTION

Improvement in the technology to probe and sense small objects as well as quantities in nature usually leads to major science breakthroughs in human history. Robert Hooke's invention of microscopy in 1665 [1] opened up the era of micrometer imaging, which also led to the discovery of cells. Afterward, the invention of atomic force microscopy in 1986 [2] pushed the boundary of distance measurement to the angstrom scale. The invention of superconducting quantum interference device in 1964 [3] led to the magnetic sensing in the sub-nanotesla range.

In general, nanoscale sensors measure only one quantity per sensor, but it is desirable to have a multi-functional sensor. In recent years, the development of diamond based sensors has shown that the nitrogen vacancy (NV) centers in diamonds are promising all-purpose detectors. Due to the fact that the NV centers' spin state can be optically detected at room temperature [4], all the physical quantities coupled to the NV centers' spins are thus optically measurable. The NV centers are capable of optically detecting magnetic field [5], electric field [6], strain force [7], and temperature [8]. As non-bleaching, non-toxic, single photon emitters, the NV centers in nanodiamonds (NDs) can also find applications in the super-resolution imaging techniques such as stimulated emission depletion microscopy (STED) [9], deterministic emitter switch microscopy (DESM) [10],

and stochastic optical reconstruction microscopy (STORM) [11]. In addition, the NV centers in diamonds have long coherence time, thus are also an excellent candidates for quantum computation [12], quantum communication [13], and quantum cryptography [14].

Although the NV centers have been produced and studied for 30 years [15], the recipe for high concentration production and optimum sensitivity has not yet been systematically studied. In addition, a high concentration of the NV centers for the biological applications is needed in small NDs [16][17].

In chapter II, we demonstrate the method of producing high concentration NV centers in both the theoretical and experimental studies. First, we examine the optical and magnetic properties of the NV centers with various doses and temperatures, and then obtain an optimum recipe for NV centers production in bulk diamonds. Moreover, the size shrinking and fluorescence enhancement effects are found in the NV centers of NDs for eventual biological applications.

In chapter III, we study the photoconductance dynamics such as the optical quenching and recovery of photocurrent measurement in diamonds to explore the possibility of the photocurrent detected magnetic resonance in NV centers, and investigate the electronic level structure of bulk diamonds. We also propose a defect-trap model for the optically quenched photocurrent effect in diamonds.

In chapter IV, we design a microwave pulse to control the NV centers' spins and find the speed of spin control is faster than ordinary Rabi flopping. For given transition energy, the Rabi frequency is proportional to the applied microwave field at low power. However,

the Rabi rotation becomes non-linear and uncontrollable with the microwave field when the driving microwave frequency is close to the spin transition frequency. To improve the driving speed of spin based qubit at high driving power, the new pulse was designed by numerically solving the Schrödinger equation. The result from our new microwave pulse was generated through the arbitrary wave form generator and gave high fidelity and provided faster speed than Rabi control.

1.1 Diamond properties

A diamond is a transparent crystal and consists of carbon, which exhibits extremely high hardness, electric resistivity and thermal conductivity. Table. 1-1 summarizes the properties of diamonds:

The face-centered cubic with sp3 covalent bonds in a diamond's crystal structure make a diamond hard and chemically inert. Using strong acid to clean a diamond allows for the removal of most dirt, some amorphous carbon, and graphite on the surface without eroding the diamond. The high bond strength of a diamond also allow heating in vacuum at high temperature up to 1700℃, and can be baked in air up to 700℃ before converting to graphite. The surface of bulk diamonds and NDs are usually covered with graphite, amorphous carbon, and the functional chemical groups such as C=O, O-H, and C-H. To remove the surface layers of graphite and amorphous carbon, diamonds are either oxidized with acid such as a boiling piranha solution (H_2SO_4:H_2O_2=3:1) at 500℃ for 2 hours, oxidized in mixed acid solution (sulfuric acid: nitric acid : perchloric acid =1 : 1 : 1) at 90℃ for 3.5 hours, or baked in ambient air at 400℃ for a few hours. After oxidation, C-

H groups are completely removed, but most of the C=O and O-H groups on the surface

remain [18][19].

Table. 1-1 Common properties of diamond

Mohs hardness	10
Molar mass	12.01 g/mol
Chemical formula	C
Crystal structure	Octahedral
Density	3.52 g/cm^3
Refractive index	2.418
Thermal conductivity	900-2320 w/m $\cdot$ K
Optical transmission	225 nm to IR
Debye Temperature	2200 K
Displacement energy	43 to 46 eV
Binding energy	7.3 eV
Electrical Resistivity	100 G$\Omega \cdot$ m

1.2 Synthesized diamonds and classification

Ordinary bulk diamonds contain impurities which cause variations in color. In Table.

1-2, the types of bulk diamond type are classified. To produce diamond, there are some

common methods:

- High pressure high temperature synthesis (HPHT) diamonds are produced

from a pure carbon source at temperature around 1500℃ under 5 GPa pressure. The diamonds produced in this method contain nitrogen impurities and are mostly type Ib diamonds [21].

- Chemical vapor deposition (CVD) diamonds are formed with ionized

methane and hydrogen gas where the growth completes with the plasma etching (shown in Fig. 1-1). The diamonds produced in this method can be easily grown with selected impurities. The CVD diamonds are the main source of ultrapure diamond (type IIa) [20].

Table. 1-2 Different types of diamond

Classification				Color
Type I	Nitrogen impurity	Type IA	Clusters of nitrogen impurities.	Pale yellow or colorless
		Type IB	Single nitrogen atom impurities dispersed in diamond	Dark yellow or brown
Type II	No nitrogen impurity	Type IIA	Almost or entirely devoid of impurity	colorless
		Type IIB	Boron impurity	Light blue or grey
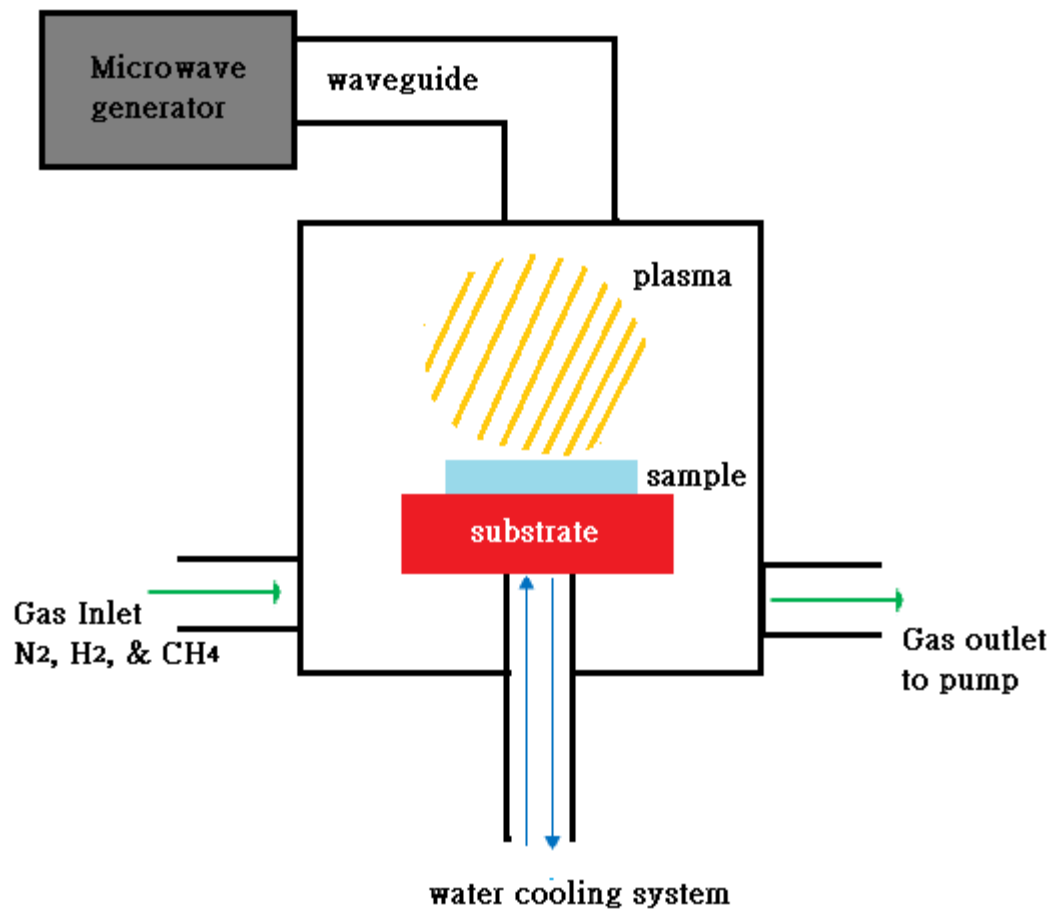
Fig. 1-1 Schematics of the formation of chemical vapor deposition diamonds.

● Detonation NDs originate from the detonation of a mixture

of trinitrotoluene and hexogen. The typical diamond particle size produced in

this method is around 5~8 nm [22].

1.3 Semiconductor properties of diamond

The energy gap between the conduction band and the valence band of an undoped diamond is around 5.4 eV, which makes undoped diamond an electronic insulator. However, as a semiconductor, a diamond is like silicon which can be doped with electron donor impurities or acceptor impurities to form the n-type or p-type semiconductor. For example, when a diamond is doped with nitrogen impurities, a diamond with substitutional nitrogen defects becomes a n-type semiconductor due to a broad electron donor band reducing the effective gap to around 1.7 eV as shown in Fig. 1-2, which is taken from [23, 24].

Charge carriers like mobile electrons in the conduction band of the n-type diamond or holes in the valence band of the p-type diamond can be considered as particles moving in a crystal. When applied with an electric field, the velocity of charge carriers $\vec{v_c}$ can be decomposed into the thermal velocity $\vec{v_{th}}$ and the drift velocity $\vec{v_d}$, given by

$\vec{v_c} = \vec{v_{th}} + \vec{v_d}$. The randomness of thermal motion makes the thermal velocity averaged to zero, and only the drift velocity $\vec{v_d}$ left in $\vec{v_c}$.
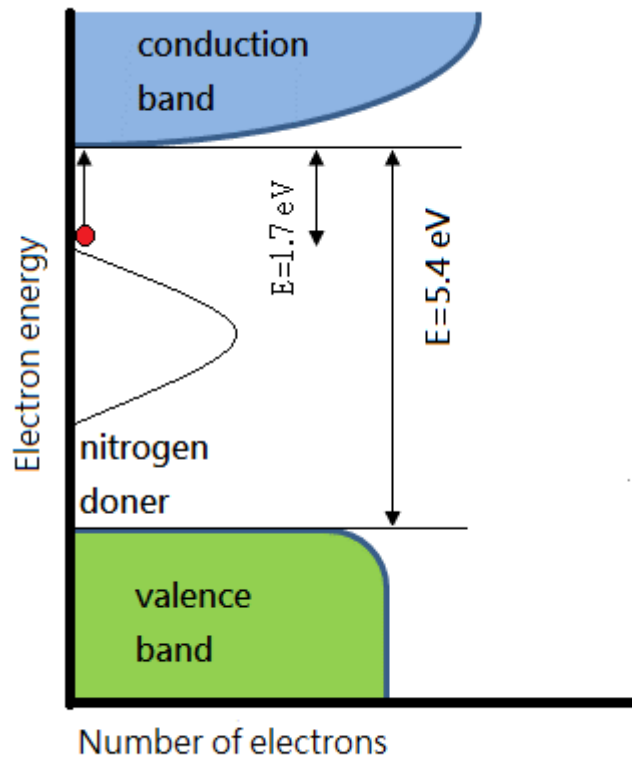
Fig. 1-2 Diamond electronic structure. The band gap between valence band to conduction band is 5.4 eV, and nitrogen donor reduce the effective band gap to 1.7 eV.

For a small electric field E, the drift velocity is proportional to the applied field:

$$\vec{v_d} = \mu\vec{E}, \tag{1.1}$$

where μ is the charge carrier mobility. By multiplying equation (1.1) with unit charge e and carrier density n, we get the equation for the current density in diamond:

$$j = en\mu E = en\mu V/d, \tag{1.2}$$

where j is the carrier current density, V the bias voltage, and d the electrodes separation distance. The same equation also applies to the photocurrent in diamonds excited by a laser. In the case of the photocurrent in a diamond plate with a low absorption coefficient, the carrier concentration n is given by [25]:

$$n = \tau\, \eta\, \varphi(1 - R)\alpha, \tag{1.3}$$

where τ is the excitation life time, η the photon to electron quantum efficiency, φ the photon flux, R the reflectivity, and α the absorption coefficient. In the end, the photocurrent density in a diamond may be expressed as:

$$j = e\mu\tau\, \eta\, \varphi(1 - R)\alpha\, V/d \tag{1.4}$$

1.4 Defect centers in diamond

The most common defects in crystalline solids are vacancy and interstitial centers. When atoms in crystal are dislocated, vacancy-interstitial pairs are generated. The dislocated atom is called interstitial, and the empty crystal location is called vacancy as shown in Fig. 1-3. In the synthetic IIA diamonds, imperfections in the production procedure leaves a vacancy, interstitial, and single substiutional nitrogen (p1 center) as the main defect centers.
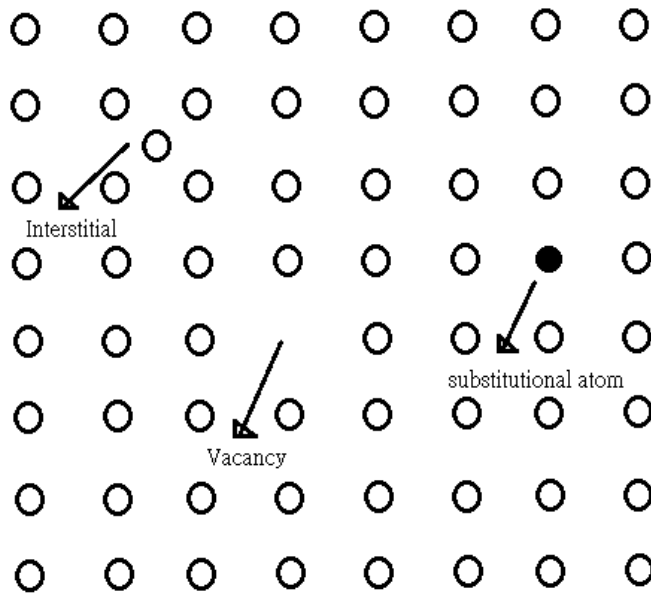
Fig. 1-3 Common crystallographic defect in diamond. Interstitials are atoms trapped outside lattice, vacancies are void crystal locations, and substitutional defects are crystal atoms replaced by exotic atoms.

The main vacancy related centers in diamonds are V^0 and V^- centers. V^0 is the neutral monovacancy with optical zero phonon line centered at 740.9 nm (abbreviated as GR1 center in optical absorption spectra), and V^- is the negative monovacancy (abbreviated as ND1 center in optical absorption spectra) with spin 3/2 and optical zero phonon line centered at 396 nm. The concentration of V^- in diamonds is highly dependent on the substitutional nitrogen centers and V^- is interchangable with V^0 under light illumination or annealing process [26]. Most of the V^0 and V^- centers anneal out above 600℃ to form color centers like NV, non-radiative ESR centers like the divacancy V_2 and higher ordered complex vacancies V_x [27].

10

Most of the interstitial related centers in diamonds are neutral interstitial I^0 centers with spin 1 and an optical zero phonon line centered at 736 nm. I^0 centers are mobile at room temperature during irradiation or implantation with an activation energy of 0.6 eV. Above 400°C, I^0 centers begin to form another spin 1 ESR center the I_2 di-interstitial [28].

For measurement in untreated diamonds, common spin centers include V^-, single substitutional N (P1), I^0, ^{13}C (carbon 13 isotope), and NV center. To reduce the spin noise in diamonds, annealing at 1200°C could eliminate most of the ESR centers except ^{13}C while the NV center concentration remains unchanged [29].

1.5 The NV centers in diamond

The substitutional nitrogen impurity with a carbon vacancy nearby in diamonds is called an NV center as shown in Fig. 1-4. The NV centers, belonging to the C_{3V} pyramidal symmetric group, can be found in both natural and synthesized diamonds, and the two charge states, $N - V^0$ and $N - V^-$, have optical zero phonon lines centered at 575 nm and 637 nm, respectively [30].
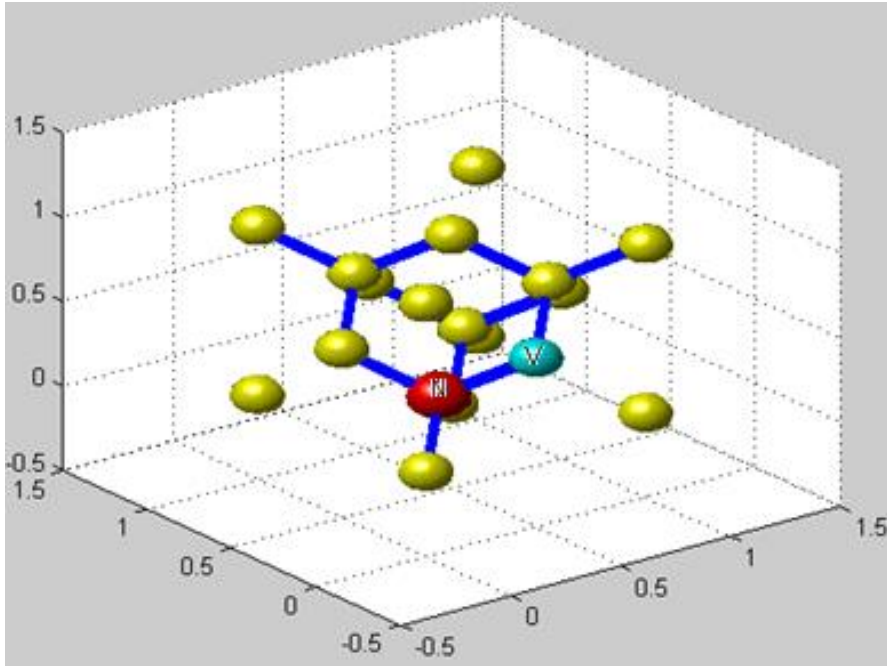
Fig. 1-4 Schematic of nitrogen-vacancy center in diamond. The units on the axis are diamond lattice constant (3.567 Å). The red sphere is the nitrogen atom and cyan sphere is the vacancy site nearby.

In the vacancy site of the $N - V^0$ centers, there are 4 electrons with the vacancy and one electron from the nitrogen atom. For $N - V^-$, there is an extra electron. In this work, only negatively charged nitrogen vacancy centers will be discussed and simply abbreviated as NV.

The two unpaired electrons in the NV centers form a spin ground state triplet (S=1). The electron orbital transition between the triplet excited state ^3E and the triplet ground state ^3A are separated by 1.945eV (637 nm) with an excited state life time of 13 ns [31],

while at least two metastable singlet states ^{1}A and ^{1}E exist between ^{3}E and ^{3}A with a life time of approximately 150~300 ns. The energy level diagram is shown in Fig. 1-5.
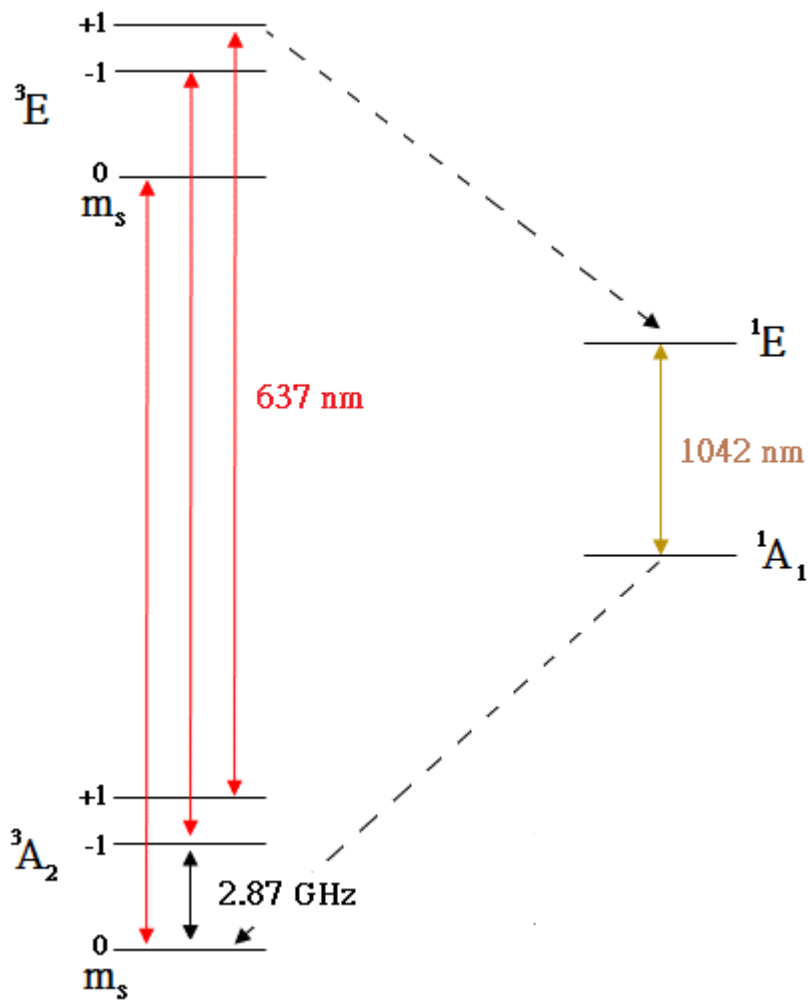
Fig. 1-5 Electron energy diagram of the NV centers with photon and phonon induced transitions. Radioactive transitions are marked with solid arrows and non-radioactive transitions are marked with dashed arrows.

There are two decay channels from the excited state ^{3}E: the spin preserved channel from ^{3}E to ^{3}A with emission of a photon, and the non-radiative spin-selective channel from ^{3}E via the singlet metastable state ^{1}A to ^{3}A which causes the $m_s = \pm 1$ excited sublevels to decay to the $m_s = 0$ ground sublevel. Thus, the net effect after a few optical pumping cycles is spin polarization to the $m_s = 0$ state. In addition, when the spin starts at the $m_s = \pm 1$ sublevel of ^{3}A and gets excited to ^{3}E, and then goes to ^{1}E, the electron spends 150~300 ns in this metastable ^{1}E state which results in lower fluorescence compared to the case when the triplet spin starts at $m_s = 0$.

The electron spin Hamiltonian of NV$^-$ is given by:

$$H_{\text{spin}} = D(S_z^2 - \frac{1}{3}[S(S+1)]) + E(S_x^2 - S_y^2) + \gamma B \cdot S \tag{1.5}$$

with D the zero field splitting (ZFS) of 2.87 GHz at the microwave range, E the strain term, γ the electron gyromagnetic ratio, and B the external magnetic field. Without the presence of a magnetic field, the energy of the $m_s = \pm 1$ states are intrinsically higher than the $m_s = 0$ state since there is nonzero ZFS.

There is also hyperfine coupling between electron and the nearby nuclei with nonzero spins such as $^{14}_{7}$N, $^{15}_{7}$N, and $^{13}_{6}$C leading to sublevels with less than 4% of the zero field splitting [32].

1.6 Electron spin resonance in diamond

For small (< 1027 Gauss) axial magnetic fields or non-axial magnetic fields, the m_s=0 to the m_s=-1 transitions of a NV center can be treated as an independent two-level spin quantum system:

$$|\psi(t)\rangle = C_0(t)|0\rangle + C_1(t)|-1\rangle, \tag{1.6}$$

where $|\psi(t)\rangle$ is the spin wave function, and $C_0(t)$ and $C_1(t)$ are the respective probability amplitudes of the $|0\rangle$ and $|-1\rangle$ states. The corresponding Schrödinger equation is

$$|\dot{\psi}(t)\rangle = -\frac{i}{\hbar} H |\psi(t)\rangle \tag{1.7}$$

with

$$H = H_0 + H_1, \tag{1.8}$$

where H_0 and H_1 correspond to the unperturbed and perturbed part of the Hamiltonian. In terms of spin states, we can write H_0 as

$$H_0 = \hbar\omega_0|0\rangle\langle 0| + \hbar\omega_1|-1\rangle\langle -1| \tag{1.9}$$

and write H_1 as

$$H_1 = -(m_{01}|0\rangle\langle -1| + m_{10}|-1\rangle\langle 0|)H(t), \tag{1.10}$$

where $m_{01} = m_{10}{}^* = \langle 0|m|-1\rangle$ is the matrix elements of the magnetic dipole moment and H(t) is the field at the NV center. Here we assume the magnetic field is linearly polarized to the x-axis. The driving field can be expressed as

$$H(t) = B\cos(vt), \tag{1.11}$$

where B is the driving field amplitude and v the driving frequency. By inserting the two states wave function into the Hamiltonian, we get

$$\dot{C}_0 = -i\omega_0 C_0 + i\Omega_R e^{-i\varphi}\cos(vt)\, C_1(t) \tag{1.12}$$

$$\dot{C}_1 = -i\omega_1 C_1 + i\Omega_R e^{i\varphi}\cos(vt)\, C_0(t), \tag{1.13}$$

where the Rabi frequency Ω_R is defined as

$$\Omega_R = \frac{|m_{10}|B}{\hbar} \tag{1.14}$$

and φ is the dipole phase

$$|m_{10}| = m_{01}e^{i\varphi} \tag{1.15}$$

Employ the assumption of slow varying amplitude

$$c_0 = C_0 e^{i\omega_0 t} \tag{1.16}$$

$$c_1 = C_1 e^{i\omega_1 t} \tag{1.17}$$

with initial condition $C_0(0) = 1$ and $C_1(0) = 0$, we get the solution for the two level

spin system:

$$c_0 = [\cos\left(\frac{\Omega t}{2}\right) - \frac{i\Delta}{\Omega}\sin(\frac{\Omega t}{2})]e^{i\Delta t/2} \qquad (1.18)$$

$$c_1 = [\frac{i\Omega_R}{\Omega}e^{i\varphi}\sin(\frac{\Omega t}{2})]e^{i\Delta t/2}, \qquad (1.19)$$

where Δ is the frequency detuning $\Delta \equiv (\omega_1 - \omega_0) - \nu$, and Ω is the generalized Rabi

frequency $\Omega = \sqrt{\Omega_R{}^2 + \Delta^2}$. Note that the rotating wave approximation (neglecting

counter rotating terms proportional to $e^{\pm i(\omega_1 - \omega_0 + \nu)t}$) has been used under the condition of

low driving field. When the driving field is close to the transition frequency, the rotating

wave approximation can not hold and the numerical solution has to be used instead. The

probability of spin being in the $|-1\rangle$ state is then given by

$$P_{-1}(t) = C_1(t)^2 = [\frac{\Omega_R}{\Omega}\sin\left(\frac{1}{2}\Omega t\right)]^2, \qquad (1.20)$$

The Rabi flopping diagram is shown as Fig. 1-6.
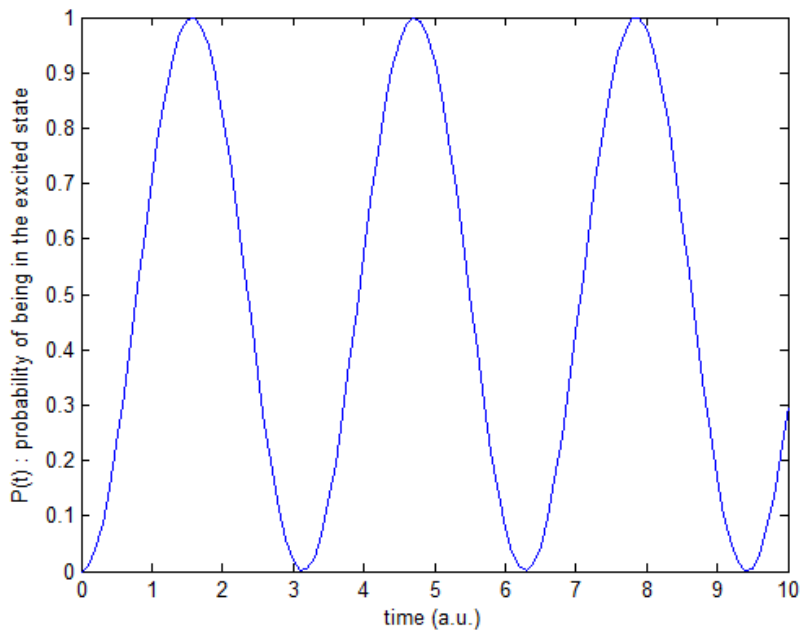
Fig. 1-6 Example of Rabi flopping of two levels quantum system. The time evolution of the quantum two levels system resembles a sinusoidal functions.

The spin state may be "rotated" by different phase angles in the Bloch sphere by applying the driving microwave field for some specific time. The simplest pulsed ESR experiment is free induction decay. After initializing the spins of the system to the $|0\rangle$ state, the $\pi/2$ microwave pulse is applied to rotate the spin to a state in the x-y plane as shown in Fig. 1-7.
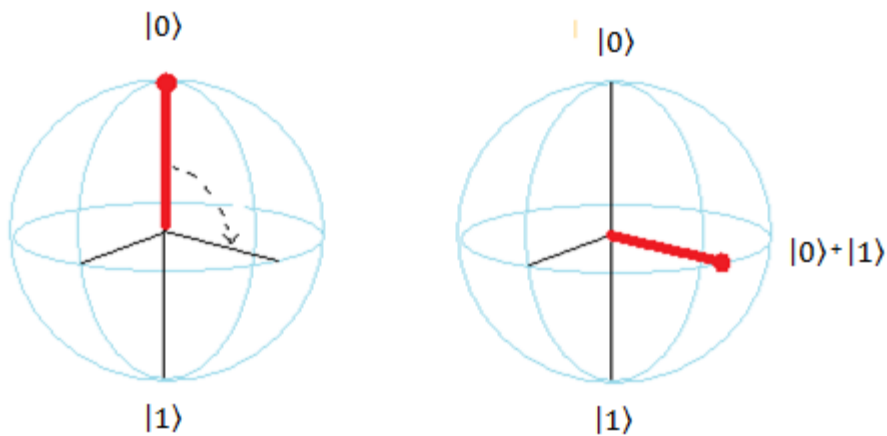
Fig. 1-7 Spin rotation of $\pi/2$ in Bloch sphere. The spin initially at the $|0\rangle$ state rotates to a mixed state between the $|0\rangle$ and the $|1\rangle$ state on the x-y plane.

The spin ensemble system is left to develop for an adjustable time τ, after that, the signals generated by the spin states are read out with the results of decaying signals due to dephasing. The purpose here is to measure the spin dephasing time during the interval τ. The detected signals decay due to inhomogeneous broadening and spin-spin relaxation. An alternative way to monitor the spin interaction for longer time is to apply a Hahn echo pulse sequence. Basically, the Hahn echo pulse add an extra microwave π pulse in addition to a $\pi/2$ pulse to refocus the inhomogeneously broadened spins in the x-y plane. The pulse sequences for FID and Hahn echo for ESR experiments are shown in Fig. 1-8.
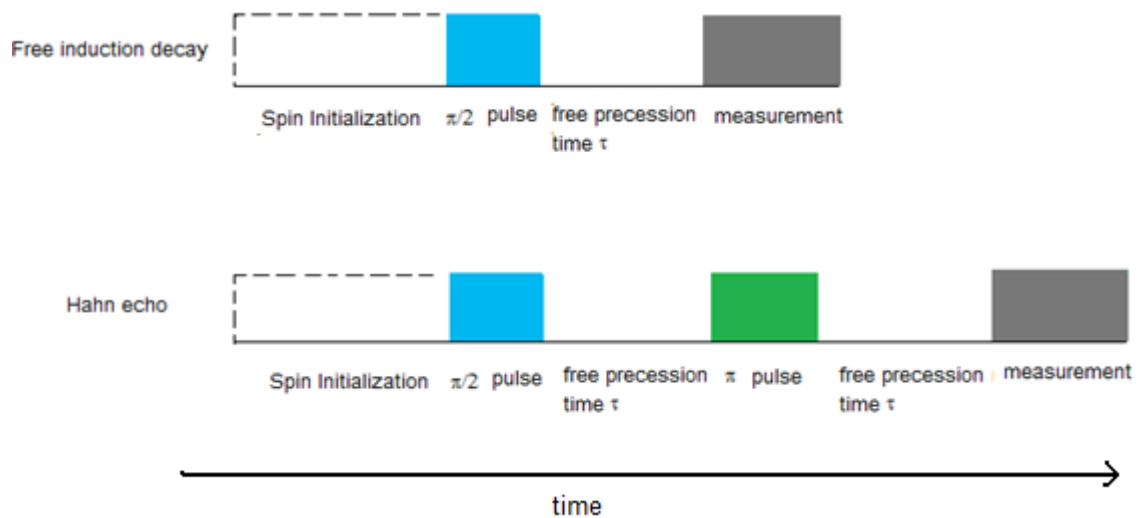
Fig. 1-8 Schematic diagram of different pulse ESR experiments. Free precession time τ is varied during the ESR experiment. The ESR signals are measured with solenoid coils.

For optically detected magnetic resonance (ODMR) of NV centers in diamonds, the spin initialization process is achieved by pumping NV centers with green lasers for at least ten times the duration of NV center excited state life time. In addition, the green laser is also used as a probe for the fluorescence readout of the spin state. The pulse sequence of ODMR experiments of Rabi flops and echo of NV centers in diamonds are shown in Fig 1-9.
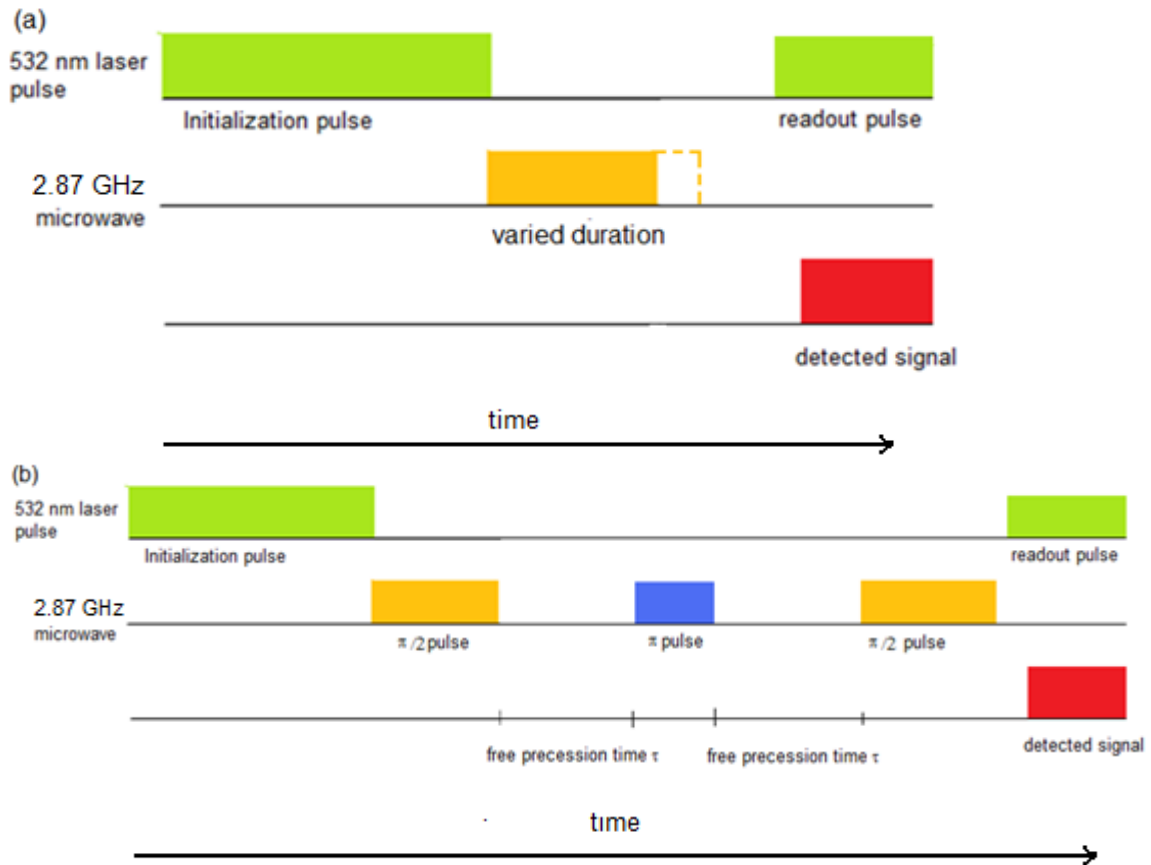
Fig. 1-9 Pulse sequence of ODMR used for NV centers. (a) Rabi oscillation (b) Hahn echo pulse sequence. The readout of ODMR signals are achieved by counting the fluorescence photons emitted by NV centers with the readout 532 nm laser pulse.

The spins in the system after the first π/2 pulse precess at slightly different speed and begin to spread out, and then the π pulse flips the precession plane and those precess farther now return faster to their initial projection. As a result, spreading spins refocus at time equal to the time delay between π and π/2 pulses are then refocused as shown in Fig. 1-10. Finally, magnetic signals that reverse sign (or change in amplitude) between the first

and second waiting time can be detected without inhomogeneous broadening. However, DC or slowly varying magnetic fields cannot be detected by this method.
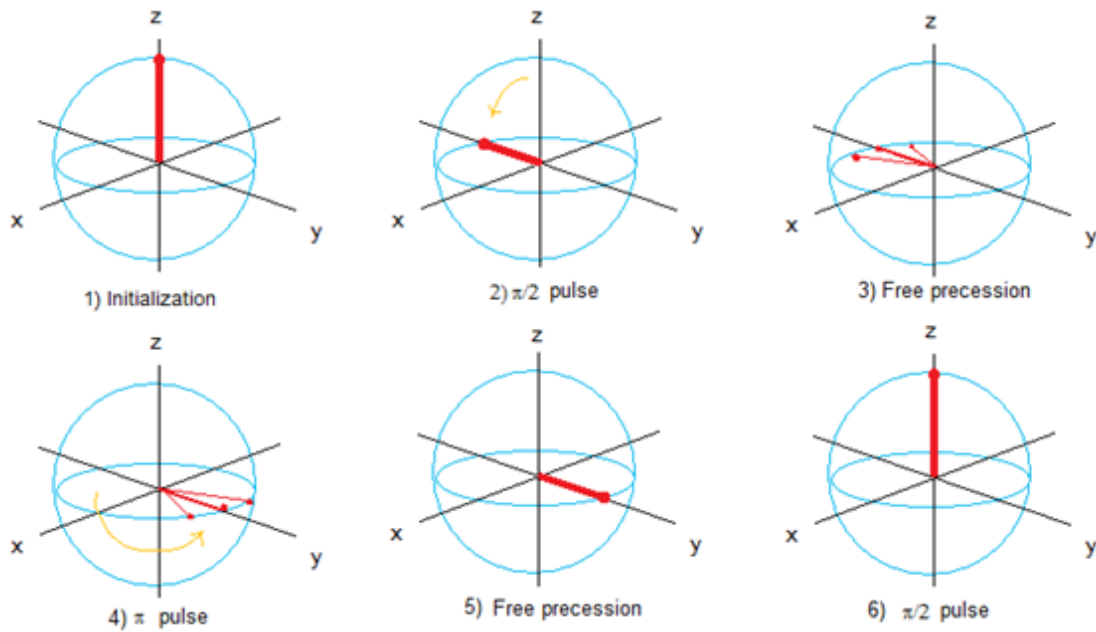
Fig. 1-10 Schematic diagram of NV spin during Hahn echo pulse. Both initialization and the readout of NV spin are achieved with illumination 532 nm laser.

1.7 Relaxation in diamond

When an electric field E is applied to a diamond, the resulting dielectric polarization P_f can be decomposed into the sum of the almost instantaneous electron polarization P_{in} and the slower dipole polarization $\Delta P(t)$:

$$P_f = P_{in} + \Delta P(t) \tag{1.21}$$

The instantaneous polarization P_{in} results from the fast displacement of electrons with respect to the nuclei. With a high frequency dielectric constant ε_h, the instantaneous polarization P_{in} can be calculated as:

$$P_{in} = E\varepsilon_0(\varepsilon_h - 1), \tag{1.22}$$

where ε_0 is the vacuum permittivity.

After polarization decay, the final polarization P_f can be expressed as:

$$P_f = E\varepsilon_0(\varepsilon - 1), \tag{1.23}$$

where ε is the static dielectric constant. For simplest 1st order kinetics, $\Delta P(t)$ is inversely proportional to a time constant τ :

$$\Delta P(t) = [(P_f - P(t))/ \tau]\Delta t \tag{1.24}$$

By solving the differential equation with given boundary conditions, we can obtain the time dependent equation for polarization:

$$P(t) = P_f - [(P_f - P_{in})e^{-\frac{t}{\tau}}] \tag{1.25}$$

For most of the experiments results in semiconductors, physical quantities cannot be simply described by equation (1.25). Instead, an empirical general form of dielectric relaxation to approximate measured results is contained in Kohlrausch-Williams-Watts relaxation function (or called stretched exponential function):

$$P(t) = P_f - [(P_f - P_{in})e^{-(\frac{t}{\tau})^\beta}], \qquad (1.26)$$

where β is a constant. The Kohlrausch-Williams-Watts relaxation function could also be found in the photocurrent quenching and recovery experiments reported in this dissertation in Chapter III. Kohlrausch-Williams-Watts type fluorescence decay also occurs in some crystalline solids like porous silicon or CdSe-ZnSe [33]. Whether it is due to a time dependent decay rate or a superposition of several exponential decays still remains unclear [34]. The fact that the Kohlrausch-Williams-Watts relaxation function exists in many natural materials suggests a common property, related to the charge-trapping kinetics.

Usually FID signals detected from diamonds are reported as an exponential decay in time, and there are two different intrinsic relaxation times of a spin ensemble, spin-lattice relaxation time (T1) and spin-spin relaxation time (T2). T1 characterizes the time needed for the longitudinal component of spin relative to external magnetic field to recover back to its thermal equilibrium state, whereas T2 characterizes the time for transverse component of the spin, sometimes called coherence, to decay toward zero. In general, the simple 1st order longitudinal spins relaxes according to

$$S_l(t) = S_{l,eq} - [S_{l,eq} - S_l(0)]e^{-\frac{t}{T_1}}, \qquad (1.27)$$

and the simple 1st order transverse spins decay according to

$$S_t(t) = S_t(0)e^{-\frac{t}{T_2}}. \qquad (1.28)$$

However in reality, the NV centers' relaxation time is often presented in the form of Kohlrausch-Williams-Watts relaxation function. As a result, the longitudinal NV spins actually relax according to

$$S_l(t) = S_{l,eq} - [S_{l,eq} - S_l(0)]e^{-(\frac{t}{T_1})^\beta} ,$$ (1.29)

and the transverse NV spins decay according to

$$S_t(t) = S_t(0)e^{-(\frac{t}{T_2})^\beta} .$$ (1.30)

For NV centers in the presence of the ESR defect centers like the substitutional nitrogen centers or the charged vacancies, T1 and T2 are mainly affected by these electron spin centers and can be shortened by implanting high concentration nitrogen defect centers. In addition, the index constant β is also dependent on the NV centers' concentration. For shallowly implanted NV centers near the surface, additional surface can shorten T1 and T2 even more. In ultrapure crystals, T1 is mainly limited by phonons and T2 is mainly limited by interactions with ^{13}C isotope in the lattice.

1.8 The photons autocorrelation function of diamond

In general, there are three different types of light sources differing by their intensity fluctuation: laser or coherent light, thermal light, and single photon emitter light as shown in Fig. 1-11. To distinguish among these, the photons autocorrelation function, or the second order coherence $g^{(2)}(\tau)$ is used, given by

$$g^{(2)}(\tau) = \frac{\langle I(t+\tau)I(t)\rangle}{\langle I(t)\rangle^2},$$ (1.31)

where I(t) stands for the light intensity at time t. The $g^{(2)}(\tau)$ can be measured experimentally and used to calculate the light source's fluctuation to determine its coherence type.
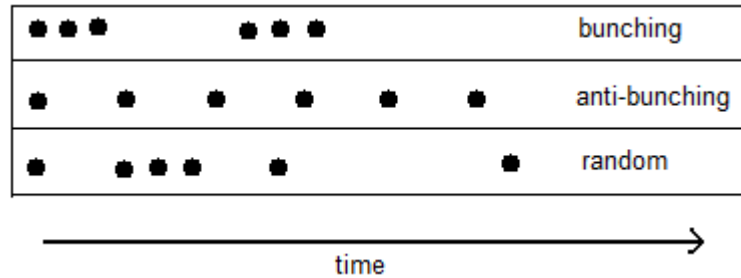
Fig. 1-11 Photons detection as a function of time and its classification.

If $g^{(2)}(0) > 1$, the light source is thermal light and shows "bunching" behavior.

And if $g^{(2)}(0) = 1$, the light source is laser-like and photons are randomly distributed as in a Poisson distribution. If $g^{(2)}(0) < 1$ which arises from single photon sources used for quantum communication and shows "anti-bunching". $g^{(2)}(\tau)$ can be measured by Hanbury Brown and Twiss experiment that utilizes an 50% beam splitter and a tunable time delay unit as Fig. 1-12 below.
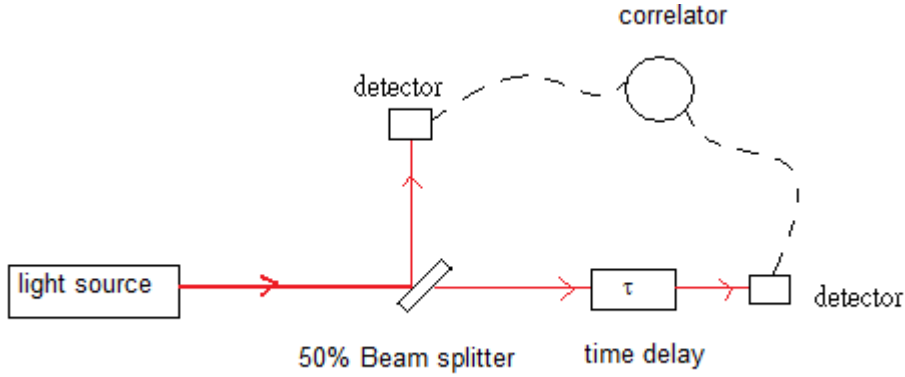
Fig. 1-12 Hanbury Brown and Twiss experiment setup.

NV centers in diamond are single photon emitters, and $g^{(2)}(\tau) < 1$ is observed with low NV concentration diamond. Since the photons statistics of NV centers is discrete and non-classical, quantum optics approach is employed here to describe the NV fluorescence behavior. If there are n fluorescence photons from NV centers in diamond, the photons are in a Fock state $|n\rangle$, where $n = 0$ or 1. The intensity of fluorescence can then be described in terms of $\langle n \rangle$, since the photo intensity is proportional to number of photons. When $\tau = 0$, the second order coherence $g^{(2)}(0)$ in terms of quantum optics notation reads:

$$g^{(2)}(0) = \frac{\langle a^+ a^+ a a \rangle}{\langle a^+ a \rangle^2}, \tag{1.32}$$

27

where a^+ is the creation operator and a the annihilation operator of the Fock states. With algebraic equations of the creation operator and the annihilation operator:

$$a^+|n\rangle = \sqrt{n+1}|n+1\rangle \tag{1.33}$$

$$a|n\rangle = \sqrt{n}|n-1\rangle \tag{1.34}$$

By substituting the equations (1.33) and (1.34) into (1.32), we were able to derive the second order coherence $g^{(2)}(0)$ in terms of n:

$$g^{(2)}(0) = 1 - \frac{1}{n} \tag{1.35}$$

Given experimental second order coherence $g^{(2)}(0)$ data from NV centers in a nanodiamond, we then can easily determine the number of NV centers in the specific nanodiamond by calculating n from equation (1.35).

CHAPTER II

THE NV CENTERS OPTIMIZATION[1]

2.1 NVs production in bulk diamond

To create a substitutional nitrogen impurity with an adjacent carbon vacancy (NV) in diamonds, there are two different ways:

(1) Ion Implantation

To produce the NV^- centers in type IIA pure diamonds, diamonds are implanted with nitrogen ions to create both nitrogen impurities and vacancies. In this work, a 2 MeV ion implanter has been used to create a large amount of vacancies per injected nitrogen ion in an electronic grade type IIA diamond.

(2) Electron Irradiation

For type IB diamond, the intrinsic nitrogen contents is around 75 ~200 ppm, and thus vacancies are required in these kind of diamond to form the NV centers. In this work, a transmission electron microscopy (TEM) JEOL-2010 has been used to create vacancies on type IB diamonds with an energy of 200 keV.

---

[1] Reprinted with permission from "Size-reduction of nanodiamonds via air oxidation" by T. Gaebel, C. Bradac, J. Chen, J.M. Say, L. Brown, P. Hemmer, J.R. Rabeau, Diamond & Related Materials **21**, 28 (2012). Copyright 2011 Elsevier B.V.

2.1.1 Ion implantation experiment

Ion implanter consists of an ion source, accelerator, and a target chamber. The ion source emits ions proportional to the excitation current applied. After ionization, the ions are accelerated and pass through mass/charge selector to filter out the unwanted charged ion. Then, the selected ions are accelerated by high DC voltage and pass through series of focusing magnets until impinging onto the sample mounted in the target chamber as Fig. 2-1.
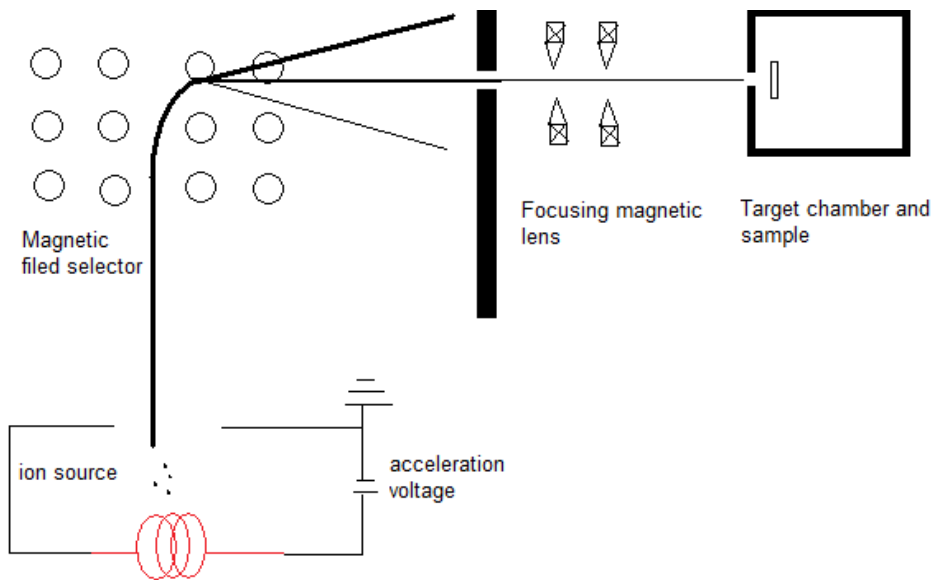
Fig. 2-1 Schematics of an ion implanter.

The ion implanter used in this work is Dynamitron electron beam particle accelerator (IBA Industrial, formerly Radiation Dynamics) which is capable of giving an implantation energy from 300keV to 50MeV. Before ion implantation, diamonds are ultrasonicated in acetone solution for 30 minutes. Then 10 MeV $^{14}_{7}N^{-}$ ions are implanted into diamonds with a flux of $3.2 \times$ ions/s $\cdot$ cm^2.

2.1.2 Electron irradiation experiment

A TEM is a microscope using electrons and electromagnetic lenses instead of photons and optical lenses. The Rayleigh resolution for a lens is given by

$$\Delta l_r = \frac{1.22\lambda}{D},$$ (2.1)

where Δl_r the spatial resolution, λ the wavelength, and D is the diameter of the lens' aperture. In the case of electrons, the de Broglie wavelength of the electrons is 1.23 nm for electrons with a kinetic energy of 1 eV, and this wavelength enables nanometer resolution of a TEM.

The basic components of TEM consist of a filament (electron gun), magnetic lens, apertures, a vacuum chamber, and a charge coupled device (CCD) camera as Fig. 2-2. In this work, high energy electrons from the TEM are used as a vacancy creation source for NV center production.
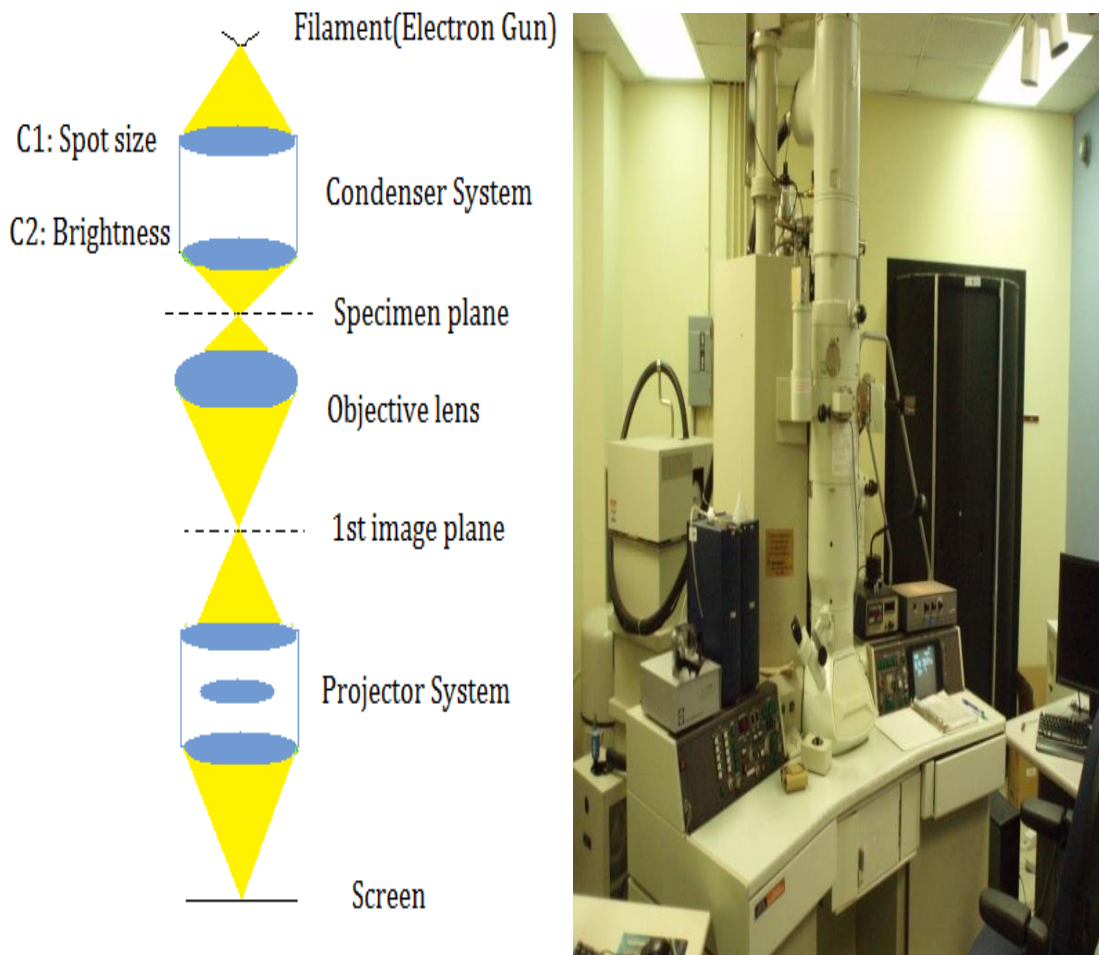
Fig. 2-2 TEM components and TEM (JEOL JEM-2010).

The TEM used in this work is JEOL JEM-2010 with LaB6 filament. A diamond sample with thickness less than 0.5 mm are cleaved to fit in the 3mm TEM sample holder, and then are clamped between two Molybdenum grids (SPI 4260M-MB) and mounted onto a single-tilt heating holder (Gatan model 628). The stage can reach temperatures up to 1000℃. The beam current density for irradiation is between 75~120 pA/cm^2 with 200 keV voltage, and the beam spot size on the TEM phosphor screen is 1~2 cm in diameter

with a magnification set to be 100 kX for highest flux. Since the actual magnification is about 75% of that on the screen, the magnification is around 75 kX. Then the total electron dose is calculated by

$$\text{dose} = J \times t \times {A_{screen}} \Big/ {M_{film}^2},\qquad (2.2)$$

where J the current density, t the irradiation time, A_{screen} the spot area on the screen, and M_{film} is the actual (linear) magnification on film.

2.1.3 Simulation of ion implantation

Ion implantation is the process where electric field accelerated ions are injected into materials to imbed impurities. The vacancies in diamond are the empty sites that carbon atoms were "kicked out" of by the recoil of the implanted ions. To produce the NV^- centers in type IIA diamonds, diamonds are implanted with nitrogen ions to create both nitrogen impurities and vacancies.

For the simulation of ions and vacancies' spatial distribution after ion implantation, a free academic sharing software "Stop and Range in Matter (SRIM)" made by Dr. James F. Ziegler was used in Fig. 2-3. To optimize the simulation, there are a few parameters in this Monte Carlo simulation could be chosen: the atomic number of the implanting ions and the implanted material, the implantation energy, the implanted material density, and the implanted material displacement energy.

Those parameters for the nitrogen ion implantation experiments in diamond are: nitrogen ion atomic number 7 and implanted carbon atomic number 6, the density of diamond 3.52 g/cm³, and the displacement energy of carbon atoms in diamond lattice 45eV [35].
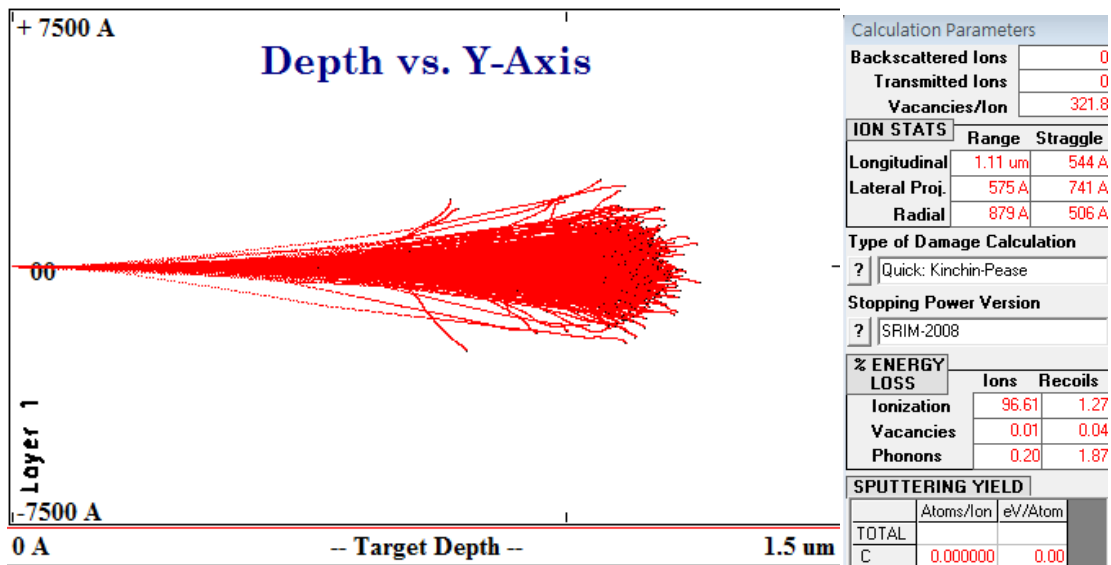
Fig. 2-3 The depth simulation of 1000 implanted nitrogen atoms in diamond for 2 MeV implantation.

There are several important simulated results that can be used for further analyzin: the vacancies created per ion, the longitudinal range of ion, the straggle distance of the

implanted material, the phonons ratio of energy loss per stopped ion. The implanted ions

and vacancy concentration versus implanted depth is shown in Fig. 2-4 and Fig. 2-5.
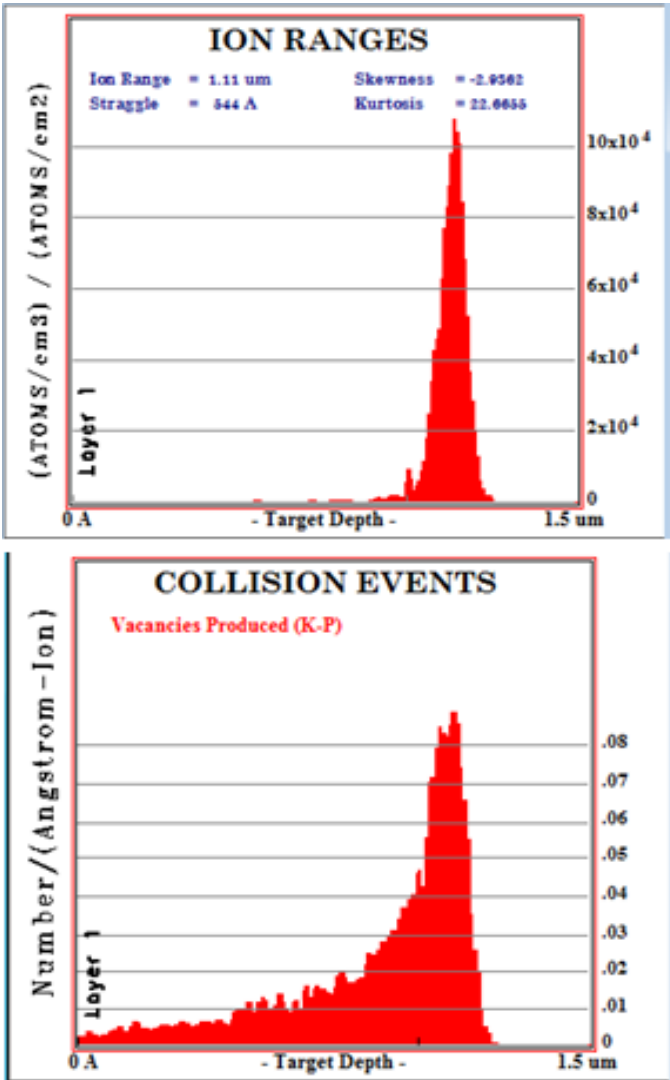
Fig. 2-4 Nitrogen and vacancy concentration simulation of 2 MeV implantation by SRIM. (Top) Ion range simulation (Bottom) Collision events simulation.
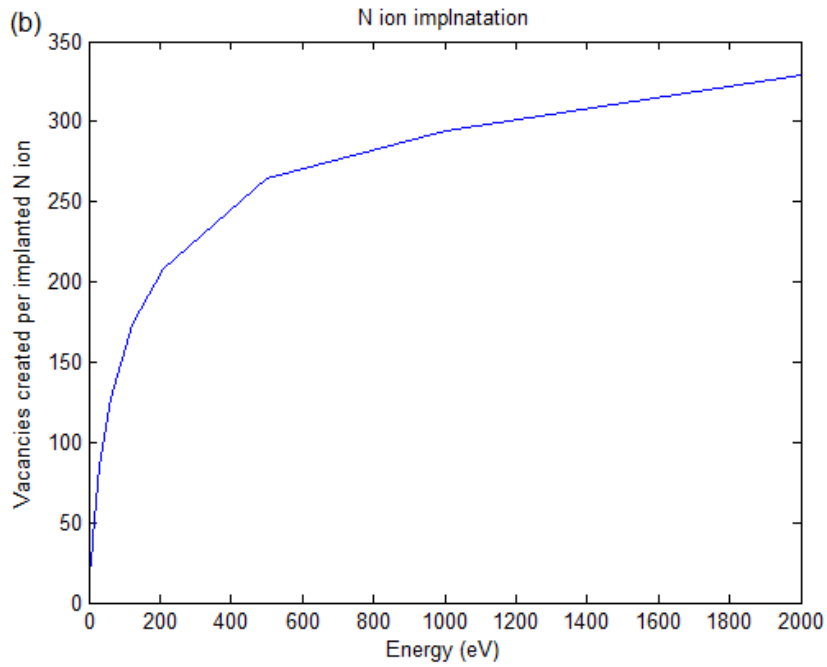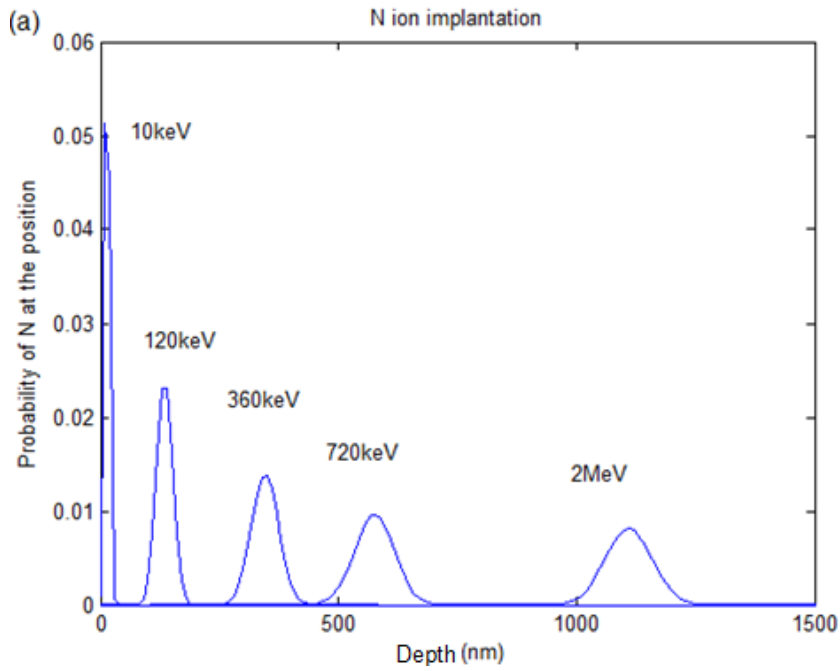
Fig. 2-5 The implantation depth and created vacancies versus the implantation energy. (a) Nitrogen number as a function of depth for different implantation energies (b) vacancies created per ion with different implantation energies based on SRIM simulation.

2.1.4 Annealing process

After ion implantation/ electron irradiation experiments, the diamonds are boiled with mixed acid solution (sulfuric acid : nitric acid : perchloric acid =1 : 1 : 1) at 90°C for 3.5 hours in a condenser system to remove the surface graphite, some of the amorphous carbon atoms, and other contamination. In order to diffuse the vacancies and form the NV centers, the acid cleaned diamonds are then heated up in the vacuum chamber at around 800C in 10^{-6} torr for 3 hours (the heating rate is 20°C /min). Finally, the diamonds are ultrasonicated in acetone for 10 minutes to remove the remaining surface residues.

2.1.5 Simulation of annealing process

Diffusion describes random motions of particles that causes the particles to move from regions of high concentration to regions of low concentration with a net effect that the particles slowly fill out the entire mobile space as shown in Fig. 2-6.
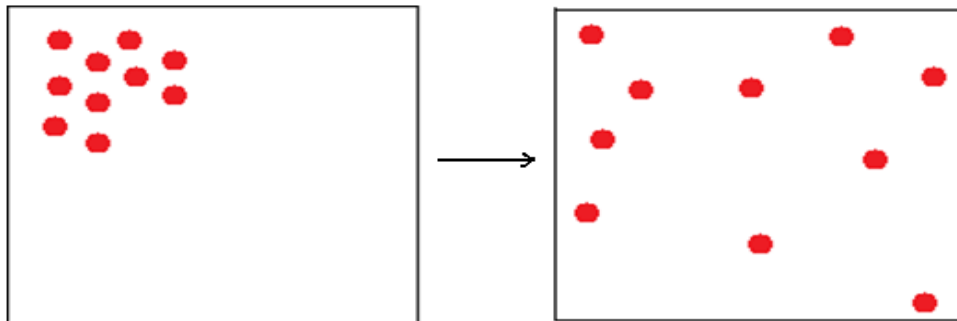
Fig. 2-6 Diffusion process. From left to right: particles diffuse from a smaller volume with higher concentration to a larger volume with lower concentration.

The diffusion process can be described by Fick's Law:

1st law

$$J(r, t) = -D\nabla C(r, t),$$ (2.3)

and 2nd law

$$\frac{\partial C(r, \ t)}{\partial t} = -\nabla \cdot J(r, \ t),$$ (2.4)

where J is the particles flux vector, D the diffusion rate coefficient, C is the concentration of particles. Combining these two equations, we obtain Fick's equation:

$$\frac{\partial C(r,t)}{\partial t} = D\nabla^2 C(r, t) \ .$$ (2.5)

The vacancies and nitrogen impurities diffuse in diamond beyond a certain temperature and the local NV centers concentration will change according to the spatial distribution of vacancies and nitrogen.

The diffusion coefficient is a function of temperature given by

$$D = D_0 e^{-\frac{E_m}{k_B T}},$$ (2.6)

where D_0 is a constant depending on material, E_m is the migration barrier energy of a diffusing particle, k_B is Boltzman's constant, and T is temperature. For simulation of the vacancies diffusion process in diamond, the leading diffusion coefficient value is reported to be 3.69×10^8 nm^2/s with the migration barrier of the vacancy between 0.42- 2.8 eV [36]. Here 1.7 eV is elected to simulate the vacancy diffusion in this work. Similarly, the

diffusivity of nitrogen at different temperatures can be found in [37] stating that there are two migration channels of nitrogen, the vacancy assisted migration energy of 4.5 eV and the self-diffusion migration energy of 6.3 eV. Compared to the vacancies, the nitrogen atoms remain static below 2200K, and the vacancy assisted nitrogen become mobile when the temperature higher than 1750K. The simulation of vacancy and nitrogen diffusion processes are shown as Fig. 2-7.
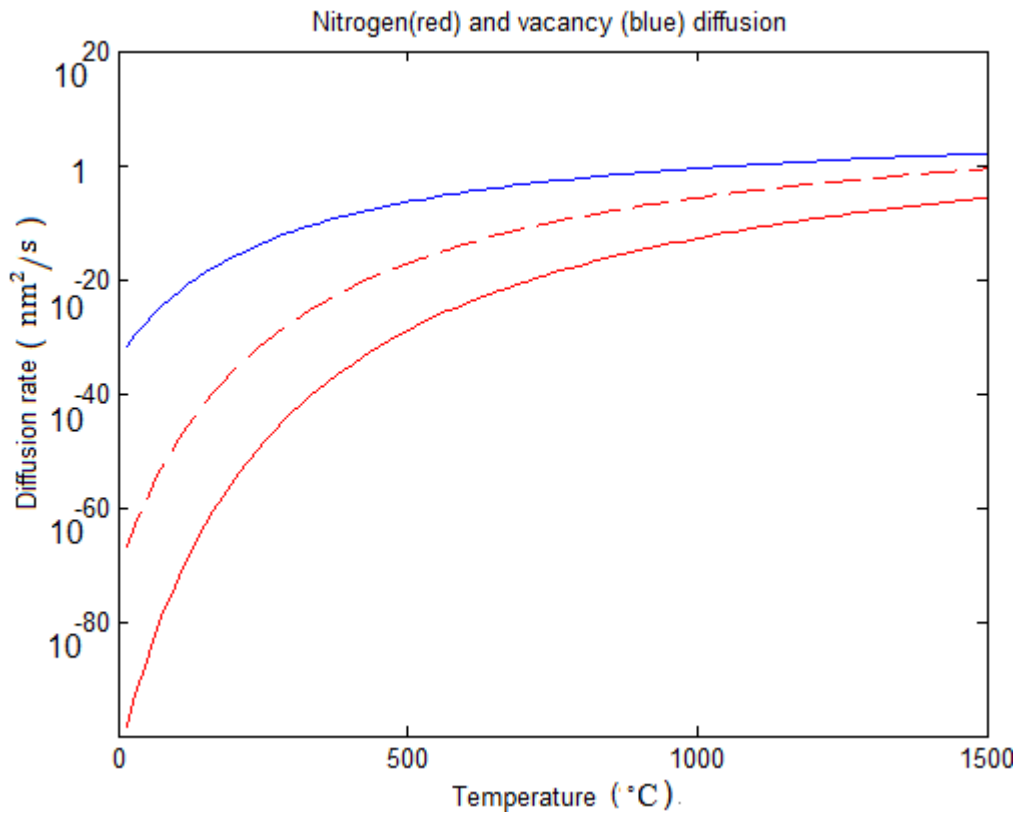
Fig. 2-7 The vacancy and nitrogen diffusion coefficient as a function of temperature. (dashed line for vacancy assisted nitrogen) The vacancies are mobile above 873 K and substitutional nitrogen atoms are mobile above 1750 K.

To include reasonable source term in Fick's equation to model the diffusion process during ion implantation, an additional Gaussian distributed source term is introduced. With an assumption that the implantation is cylindrically symmetric, we get

$$\frac{\partial C(z,\ t)}{\partial t} = D\frac{d^2 C(z,t)}{dz^2} + \frac{\Gamma}{\sigma\sqrt{2\pi}}e^{-\frac{z^2}{2\sigma^2}}\ , \tag{2.7}$$

where $\Gamma = \text{flux} = \frac{\text{number}}{\text{nm}^2\cdot\text{sec}}$, and σ is the Gaussian standard deviation parameter which is related to the implant straggle depth.

The modified dynamic diffusion process can be solved by applying the following two boundary conditions:

$$C(\pm\infty, t) = 0\ , \tag{2.8}$$

$$\frac{\partial C(0,\ t)}{\partial z} = 0\ , \tag{2.9}$$

where we define z=0 at the mean implantation depth displaced below the diamond surface according to the SRIM simulation. These boundaries equations set the concentration at infinity to be zero and the concentration to a local maximum at the mean implantation depth. (Note that the straggle is only approximately Gaussian for high energy implants as there is as significant tail for smaller depths) By Gaussian-fitting the room temperature ion implanted data from SRIM simulation as a source term in the modified Fick's equation (3.4), the dynamic solution can be obtained at different temperatures as shown in Fig. 2-8.

It was reported [38] that there is a graphitization threshold for ion implantation in diamond independent of ion species and implantation energy. A diamond crystal transforms into graphite when concentration of vacancies exceed 10 V/nm^3 and will not turn back to diamond after annealing.
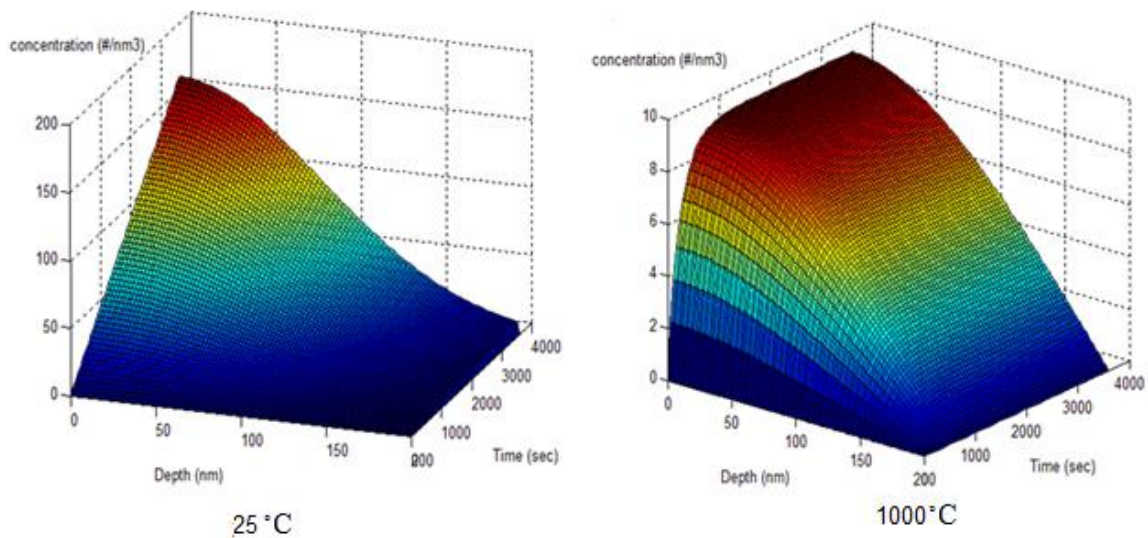
Fig. 2-8 The vacancies concentration as a function of depth and time at different temperatures. The simulation is for a 2 MeV nitrogen implantation with total dose $= 100$ N/nm^2 . Note that the concentration of vacancies stays below graphitization threshold for temperature higher than $1000°C$.

In order to maximize the yield of NV centers, the implantation of nitrogen should be done at the maximum possible dose to produce the most nitrogen and vacancies without breaking the graphitization threshold. Therefore, the implantation rate and the temperature

which determines the local vacancy concentration has to be chosen to stay below graphitization threshold. With the diffusion simulation in this work, the optimum parameters were determined to meet this requirement and are shown in Fig. 2-9.
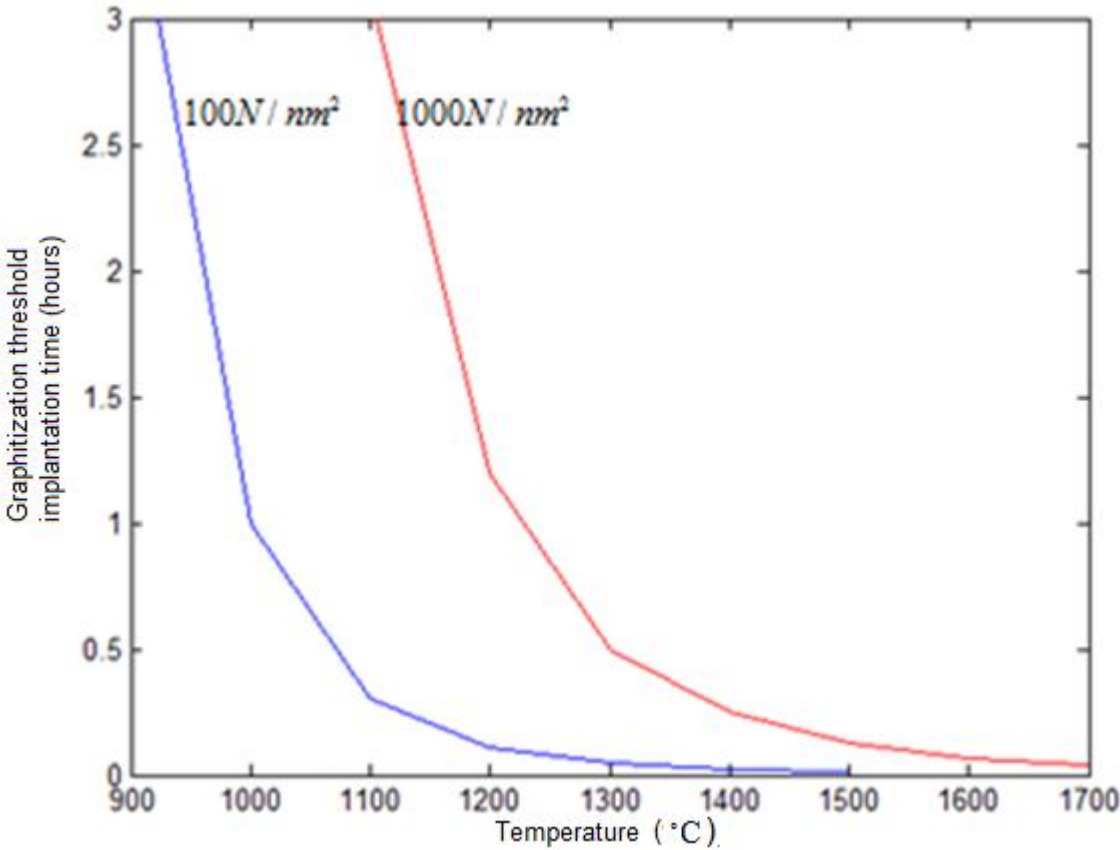
Fig. 2-9 The minimum implantation time to prevent graphitization versus temperature for various doses. (2 MeV nitrogen implantation)

The vacancies in 1B nitrogen-rich diamond or in nitrogen implanted diamond undergo these reactions:

Electrons are excited from nitrogen to the conduction band by heat or optical excitation and can be captured by vacancies

$$V + e^- \leftrightarrow V^- \qquad (2.10)$$

In addition for T> 600°C

$$V + N \rightarrow NV \qquad (2.11)$$

At high temperature of with optical illumination

$$NV + N \leftrightarrow NV^- + N^+ . \qquad (2.12)$$

The nitrogen atoms in the diamonds act like electron donors enabling free electron transport. In nitrogen rich diamonds, the negative charged vacancy centers V^- (ND1) are the dominant defects and its concentration can be an order of magnitude more than the concentration of the neutral vacancy centers V^0 (GR1) .

The nitrogen concentration in high pressure high temperature diamonds is dependent on the growth sector [39]. In addition, the yield of the NV^- centers is 10~40 times greater than the yield of NV^0 in 1B diamond after electron irradiation and annealing [40]. It is also observed that the NV center yield is reduced by vacancy-interstitial recombination which often appears in the type IIA diamonds and doesn't occur in nitrogen rich diamond [41].

The first explanation of the creation mechanism of the NV centers in 1B diamond was done by G. Davies in 1992 [42]:

$$\frac{d[V^-]}{dt} = -r_c \frac{[V^-]}{r} + r_c[V] , \qquad (2.13)$$

$$\frac{d[V]}{dt} = -(r_c + r_a)[V] + r_c \frac{[V^-]}{r},$$ (2.14)

$$\Delta[V] + \Delta[V^-] = \Delta[NV^-],$$ (2.15)

where r_c is the reaction rate of charge conversion, r_a the decay time due conversion of vacancies to NV or other defects during annealing,

and r the equilibrium ratio of $[V^-]/[V]$. Davies calculated neutral vacancy concentration by converting the optical absorption line to the concentration with

$$O_{GR1} = f_{GR1}\,[V]$$ (2.16)

and fitted his experimental data. The converting coefficient he used $\frac{f_{ND1}}{f_{GR1}} = 4$ is contrary to what is experimentally found later: $f_{ND1} = 4.8 \times 10^{-16} \text{meV} \cdot \text{cm}^2$ [43] and $f_{GR1} = 6 \times 10^{-17} \text{meV} \cdot \text{cm}^2$ [44]. In addition, the growth of negatively charged divacancy V_2^- in irradiated 1B diamond above 600C reported by Joseph Kiprono [45] is unaware in Davies' work, where Davies assumes that all the vacancies form the NV centers. In this work, the new dynamic model including both NV center and V_2^- centers formation will be discussed in the following.

Assume that the negatively charged divacancy V_2^- forms via the following reaction

$$V + V^- \rightarrow V_2^-$$ (2.17)

instead of capturing an electron from a neutrally charged divacancy center. (there is no neutrally charged divacancy observed in 1B diamond [46])   Also assume that the formation of NV^- centers involves the diffusion and reaction of the neutral vacancy only, since the charged vacancy doesn't diffuse [40]. Based on the two assumptions, the re-fitting of the 750℃ annealing data of 1B diamond by G. Davies [15] is done in Fig. 2-10

with the up-to-date experimental optical absorption coefficient and mutual charge conversion coefficient. The new second order kinematics for the simulation reads:

$$\frac{d[V]}{dt} = -(a \cdot r_v + r_c)[V] - (1-a)r_v[V][V^-] + r_c \frac{[V^-]}{r}, \tag{2.18}$$

$$\frac{d[V^-]}{dt} = -r_c \frac{[V^-]}{r} - (1-a)r_v[V][V^-] + r_c[V], \tag{2.19}$$
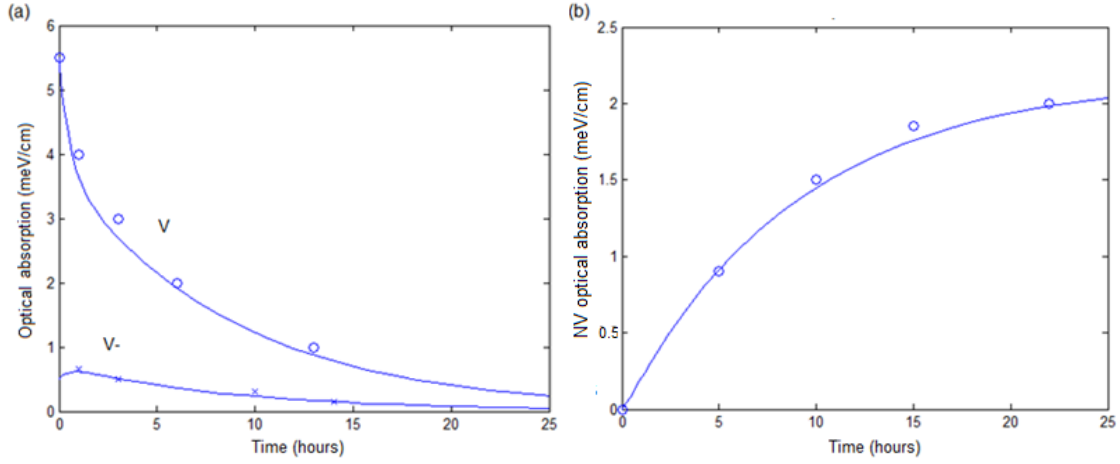
Fig. 2-10 Re-fitting of the NV optical absorption data during 750°C annealing. The sample is a 1B diamond irradiated with 2 MeV electrons to a dose of 0.5 x 10^{16}e/cm^2. (a) ND1 and GR1 with parameters: a=0.9, r_v= 0.2, r_c=0.7, and r =0.6 . The strength of optical absorption A is derived by integrating the absorption coefficient μ(E) (measured in cm^{-1}) at photon energy E (measured in meV) over the zero-phonon line: A = ∫ μ(E)dE. (b) NV line with parameter b= 0.84 and $f_{nv} = 1.35 \times 10^{-16}$ meV · cm^2.

$$\frac{d[NV^-]}{dt} = b \cdot a \cdot r_v[V], \tag{2.20}$$

where r_c the charge conversion rate, r_v the first order vacancy reaction rate, r the equilibrium ratio of $[V^-]/[V]$, a is the ratio of vacancies trapped by any sink, and b is the

ratio of the vacancies involved in [NV⁻] formation to the vacancy trapped by any sink. In addition, the equation for temperature dependence of reaction rate is used

$$r_v = r_{v0}e^{-\frac{E}{k_B T}}$$
(2.21)

with E the activation energy of 2.3eV for the vacancies captured in any sink reaction [42]. For the vacancies created by electron irradiation, the conversion between electron irradiation dose and vacancy concentration is 2 vacacnies/electron·cm [40]. Using these equations and the fitted parameters for the simulation of 750℃ annealing of 1B diamond above, the growth dynamics of NV center for 30 minutes isochronal annealing at different temperatures can be simulated and the result gives an excellent agreement with the work by G. Davies [15] as shown in Fig. 2-11.
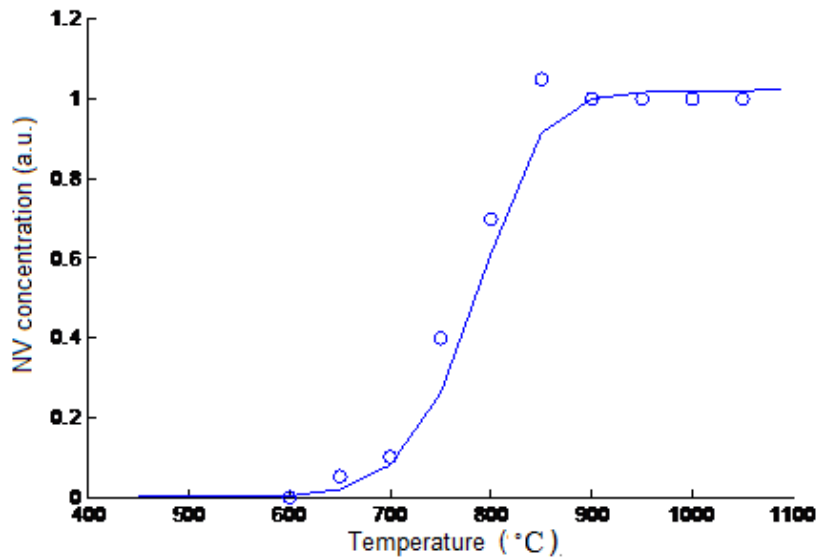
Fig. 2-11 The simulation of the NV center growth after 30 minutes isochronal annealing. The sample is a 2 MeV electron irradiated 1B diamond with a dose of $5 \times 10^{17} e/cm^2$. The parameter used here is $r_{v0} = 1.25 \times 10^7$. (it is assumed that 70% of the initially created vacancies are V⁻).

Given the initial implantation or irradiation dose, the annealing temperature and time to get the maximum NV yield can be calculated by the same simulation as shown in Fig. 2-12.
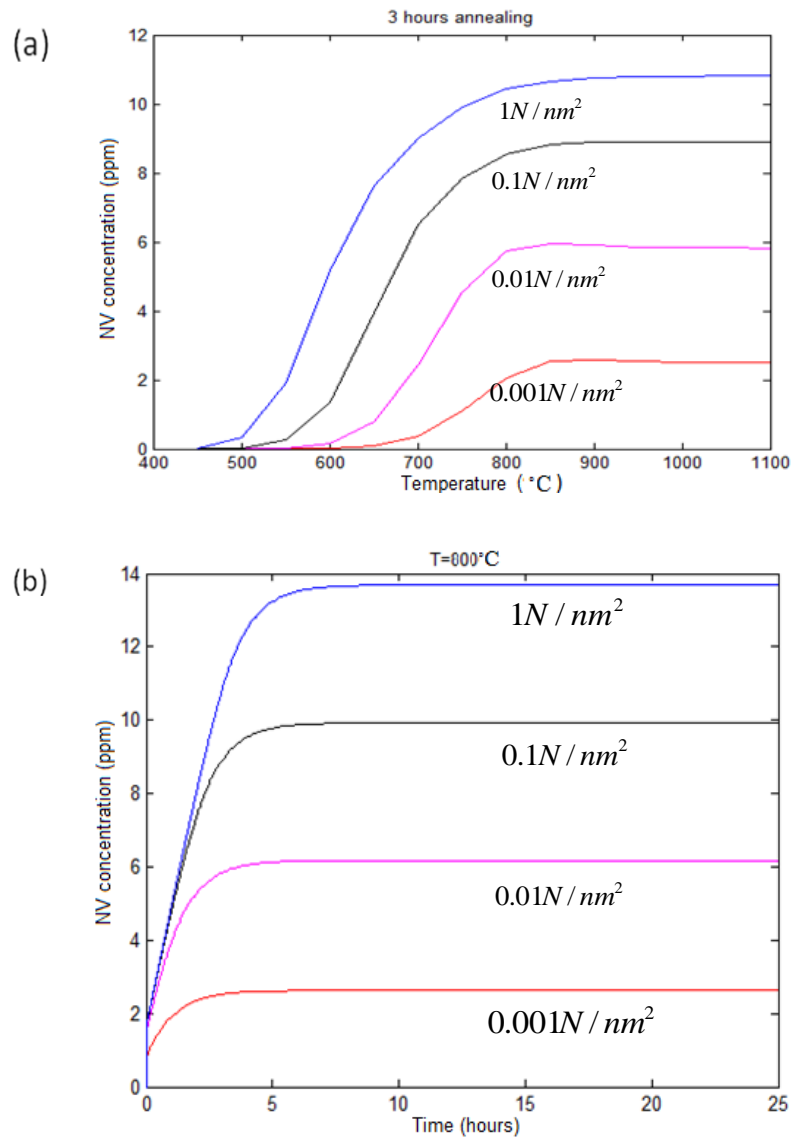
Fig. 2-12 NV concentration with different nitrogen implantation doses as a function temperature and time. (a) different annealing temperature for 3 hours annealing (b) different annealing time at 800℃.

2.1.6 NV center yield optimization in bulk diamond

To characterize the NV centers in diamond, a home-built ODMR setup as shown in Fig. 2-13 has been used to measure the NV centers' concentration, ESR line shape, and Rabi frequency.
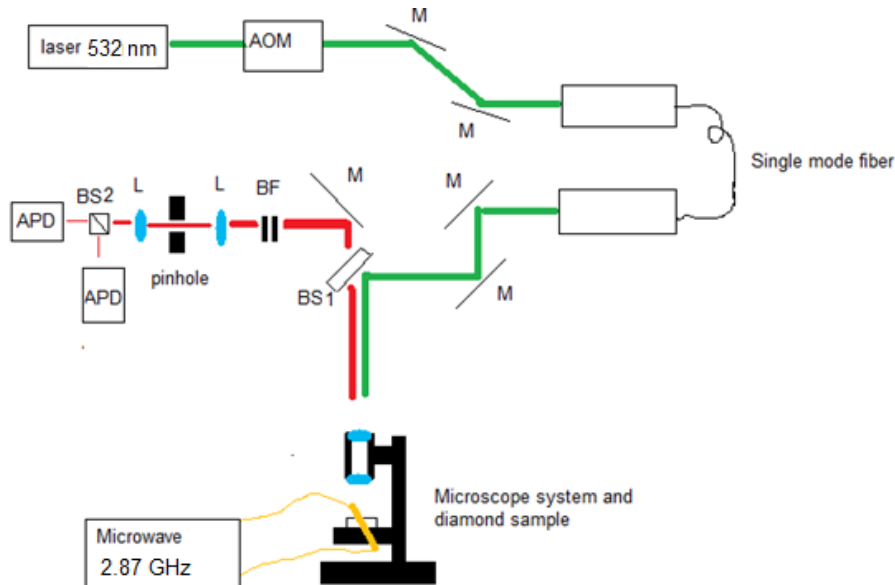
Fig. 2-13 The ODMR experimental setup. AOM is the acoustic optical modulator, M are the mirrors, BS1 is a 5% reflectance dichroic beam splitter, BF is a 630 nm longpass filter, L are the convex lenses with focal length 15cm , BS2 is a 50%-50% beam splitter, and APD is the avalanche photodiode.

The measured linear relationship between photon counts rate and laser power is shown in Fig. 2-14. The fluorescence photon count rate (with the background counts subtracted) at each pixel is in proportional to the local NV concentration and the laser

power. The actual NV center concentration might be estimated by dividing this fluorescence count rate by the single NV center photon count rate. The pixel size for the measurement in this experiment is around 0.25 μm^2 with 2.36 mW 532nm excitation laser.
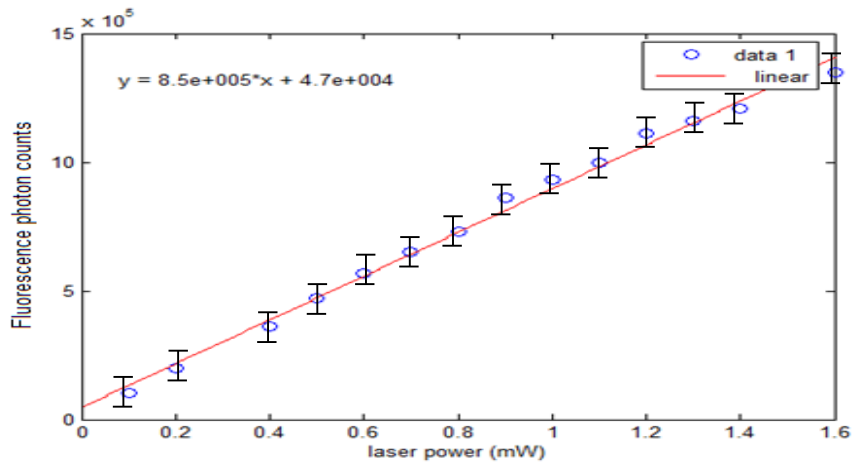
Fig. 2-14 Fluorescence photons counts versus 532 nm CW laser power. The sample is a diamond with less than 0.1% 13C isotope and is implanted with nitrogen to a dose of 0.1 N/nm^2. The signals noise is around 1% in the measurement. The estimated number of NV centers per pixel is 29.

The photon count rates measured at different implanted nitrogen dosage spots is displayed in Fig. 2-15 where the count rates are normalized to the same laser intensity 20μW. It can be seen that the photon count rate saturates above a doses of $0.1 \ ^N/_{nm^2}$ and has higher counts for nitrogen-rich diamonds. The vacancy concentration reach

graphitization threshold when nitrogen implantation dose is larger than $10 \ ^{N}/_{nm^2}$

explains the decrease of fluorescence intensity beyond the dose of $10 \ ^{N}/_{nm^2}$.
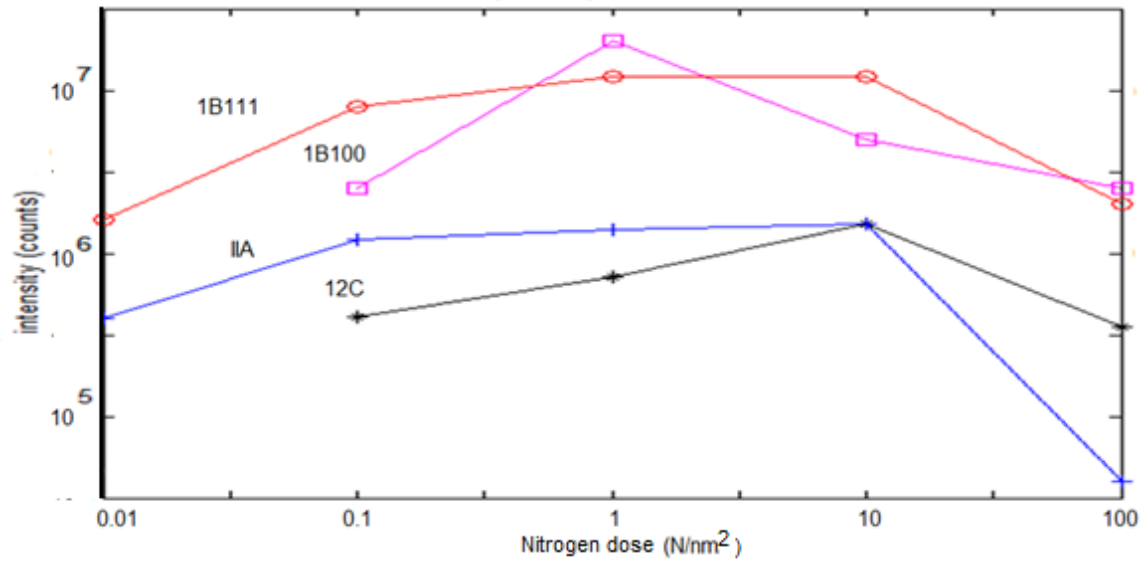
Fig. 2-15 Fluorescence counts versus 2 MeV-implanted nitrogen doses for different diamonds. IIA is a pure diamond with natural abundance of ^{13}C isotope (1.1%). 12C is a diamond with less than 0.1% ^{13}C isotope. 1B100 and 1B111 are nitrogen-rich type IB diamonds with growth sectors along 100 and 111 crystal directions.

To measure Rabi of the NV centers, the pulse sequence in Chapter I has been applied here. The laser pulses used for spin initialization and optical readout have been added to the ordinary ESR pulse in the free induction decay and Hahn echo pulse experiments. Laser illumination are synchronized with the microwave pulse by Data
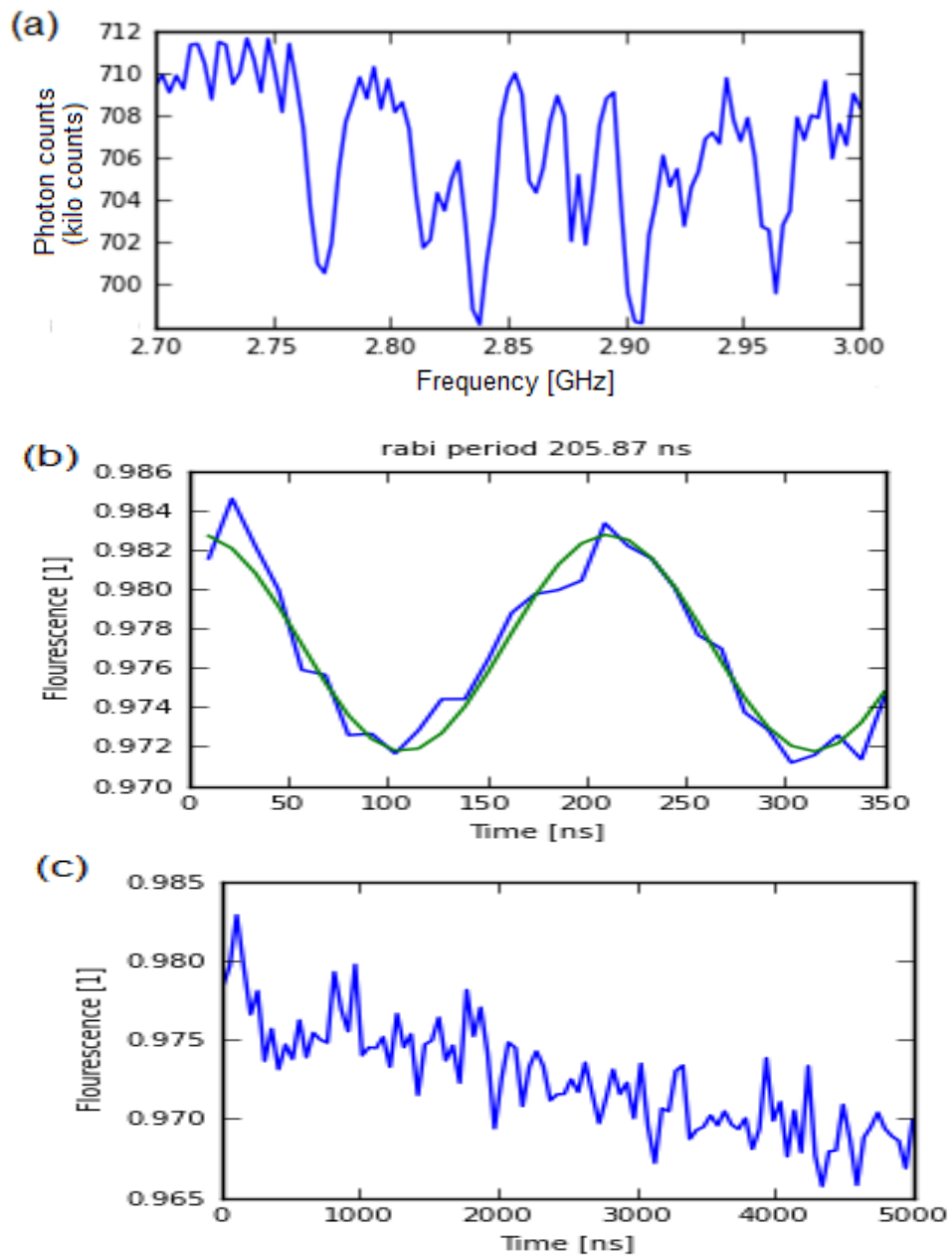
Fig. 2-16 The ODMR of a single NV center. (a) ESR line shape (b) Rabi oscillation with normalized fluorescence (c) Hahn echo measurement with normalized fluorescence. (exponential fitted value of T2 is around 17μs).

timing generator (Tektronix DTG 5274). The measured ODMR results are shown in Fig. 2-16.

In addition, the T2 measurements of a 7.5keV nitrogen implanted diamond sample with different dose in HP Labs is shown in Fig 2-17. The minimum detectable magnetic field can be estimated in the shot noise limit [40] by

$$\delta B \propto \frac{1}{\sqrt{T_2 \cdot C_{NV^-}}}$$ (2.22)

where C_{NV^-} is the concentration of NV centers. By substituting the concentration of NV centers with the measured photon counts, the optimum dose for best magnetic sensitivity in can be determined to be around 0.4 N$/nm^2$.

2.2 Reducing nanodiamond size

The use of colour centres in diamond has attracted considerable interest in a range of research fields including quantum technology and biomedical imaging. Colour centres can serve as single photon sources [48] or bright labels for bio tracking [49]. The nitrogen-vacancy centre (NV) in particular, with its unique optical and spin properties, made possible recent demonstrations such as high resolution magnetometry [50,51], sub diffraction limit optical microscopy [52,53], and quantum information technology [54,55]. Some of these applications only require the unique optical and magnetic properties of NV centres, while other applications also require controlled modification of nanodiamond material properties. For instance, reducing the size of the nanodiamond, or increasing the colour centre concentration for brighter emission can be crucial for bio-related
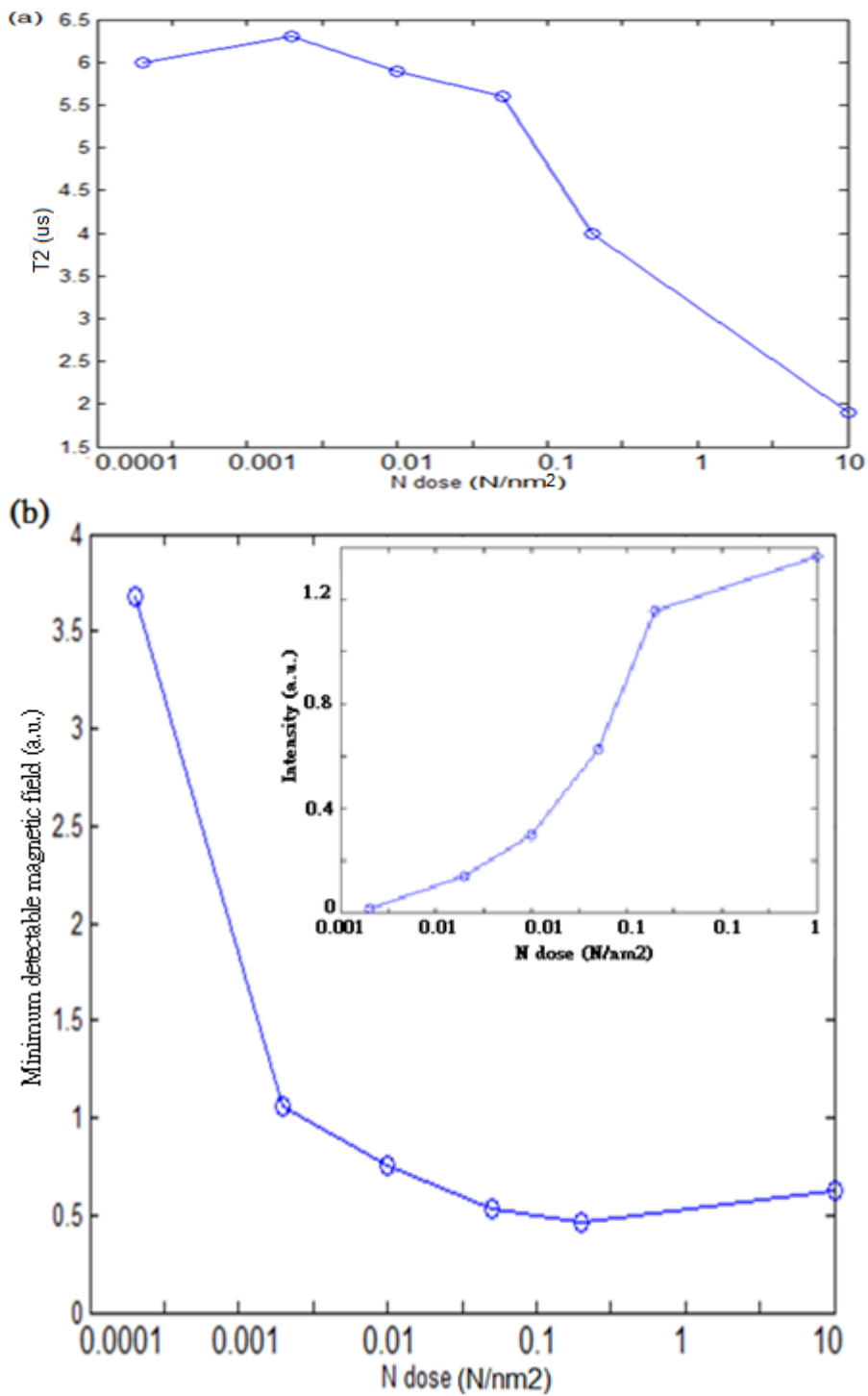
Fig. 2-17 The T2 and minimum detectable magnetic field at different doses. The sample is a type IIA diamond implanted with 7.5 keV nitrogen from HP Labs (a) The T2 measurement (b) The calculated magnetic sensitivity. (Inset) The fluorescence intensity.

applications. De-agglomeration of nanodiamonds can be achieved using a milling process with zirconia beads [56]; size reduction has been demonstrated using plasma etching [57], or thermal treatment [58].

In this work, we characterize the size of nanodiamonds and effects on nitrogen-vacancy centers caused by air oxidation of NDs by using a combined atomic force/confocal microscopy system. The average height reduction of individual crystals as measured by atomic force microscopy was 10.6 nm/h at 600°C due to air oxidation in ambient air. The oxidation process also modifies the surface including removal of amorphous carbon, graphite, and organic material which leads to a decrease in background fluorescence.

The diamond nanocrystals (Microdiamant, MSY 0-0.1 μm) with a mean size of 50 nm ranging from 0 to 100 nm as measured by an atomic force microscope (AFM), were dispersed on a glass cover slip (Menzer-Glaser). The cover slip was laser scribed with a 5 x 5 grid consisting of 50×50 μm^2 squares (Fig. 2-18). This enabled the identification of the same nanodiamond sites over consecutive oxidation steps.

The sample fluorescence was simultaneously measured with a confocal sample-scanning fluorescence microscope (100× oil immersion objective lens, NA 1.4), excitedwith a 532 nm CW diode pumped solid-state laser (Coherent, model: Compass 315-M100), and a commercial atomic force microscope (NT-MDT Ntegra) (sketch of the setup in Fig. 2-20a). Intensity autocorrelation curves were measured with a Hanbury Brown and Twiss interferometer setup consisting of 2 avalanche photodiodes (Perkin
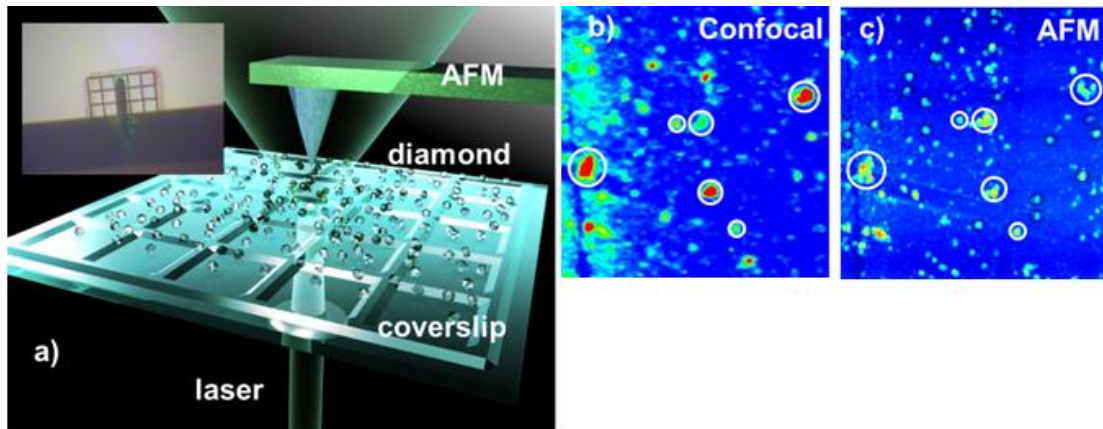
Fig. 2-18 Experimental setup of NDs characterization. (a) shows an artistic view of the confocal beam incident from the bottom and through the glass coverslip combined with the AFM tip probing the sample from above. The inset is a photograph of the sample from directly above, one can see the laser scribed grid and the AFM cantilever. (b) is a confocal intensity map of the sample and (c) shows the corresponding AFM Height map. The scan area is 50 x 50 μm.

Elmer) and a correlator (Picoquant).

The oxidation process was carried out in a tube furnace (Lenton thermal designs) in air at atmospheric pressure. The sample consisted of diamond nanocrystals dispersed on a glass coverslip and placed on a metal holder inside the furnace. The furnace temperature was stabilized before the sample being inserted into the heated region. The annealing time was measured from the instant the thermocouple mounted in contact with the metal holder with the same temperature reading as the internal furnace sensor. All annealing cycles were performed at 600°C.

2.2.1. NDs preparation

To preparation the nanodiamonds (NDs) for optimum deaggregation before size characterization, NDs were mixed with sulphuric acid (98%, 9 ml) and nitric acid (70%,

1 ml) and then refluxed for 3 days at 70℃. The mixture was centrifuged and ultrasonicated, then refluxed again with a fresh acid mixture. The nanodiamonds were washed with distilled water then refluxed with NaOH(0.1 M, 8 ml; 1 h, 90℃), washed, then refluxed with HCl (0.1 M, 8 ml). The nanodiamond–acid mixture was washed with distilled water and ultrasonicated (1 h). The sample was diluted by addition of distilled (20 ml) and ultracentrifuged (for 1 hour with acceleration of 100,000 g). This procedure was repeated three times, and the resulting pellet containing individual diamond grains was used for all the experiments. After preparation, the NDs were dropped on the glass cover slip mentioned above and left to dry.

2.2.2. Photons antibunching in NDs

The NDs were all treated with a preliminary 2 h heating step at 600℃ to remove the relatively large amount of non-diamond carbon, as well as other impurities on the sample. The fact that the surface tended to have a high proportion of sp^2 was confirmed in the etch rate measurements: where an increased etch rate was measured in the early stage of annealing (see Fig. 2-20 b). This can be explained by the higher etch rate of sp^2 compared to sp^3 carbon [59]. Fig. 2-19 shows the spectra for a NV centre taken before and after annealing. Before the treatment a broad unstructured fluorescence ranging from 550 nm to 800 nm was observed, which we attribute to a high graphite content at the surface of the nanodiamond (spectra is similar to [60], which is attributed to surface defects and graphite). After 1h of heating, the spectral features originating from NV are much more pronounced. Subsequent annealing cycles do not change the spectra in a noticeable way.
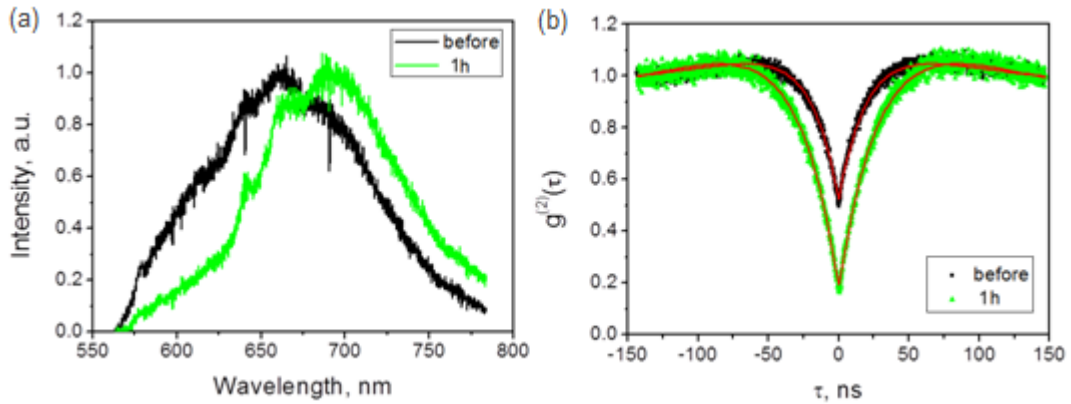
Fig. 2-19 Normalised spectra and autocorrelation $g^2(\tau)$ of one NV site. (a) Normalised spectra of one NV site following the oxidation steps. The black line is the spectra without air oxidation, and the green one shows the spectra after 1h air oxidation. (b) shows the corresponding autocorrelation $g^2(\tau)$ curves. Note that the contrast of the antibunching feature increases.

The autocorrelation curve shows in a similar way an increase in the visibility of the antibunching dip, which means that the background fluorescence level decreased after the first air oxidation step. This also supports our assertion of the preferential removal of graphitic and other non-diamond carbon material in the early oxidation stage [60], after which the etching is almost exclusively of diamond.

2.2.3. NDs size measurement

A histogram of the height of individual crystals was acquired from the AFM measurements after consecutive annealing steps which gave an indication of the average change in size as a function of anneal time. The height values were obtained by fitting 2-dimensional Gaussians to individual crystals on the AFM image after subtracting the background height offset.
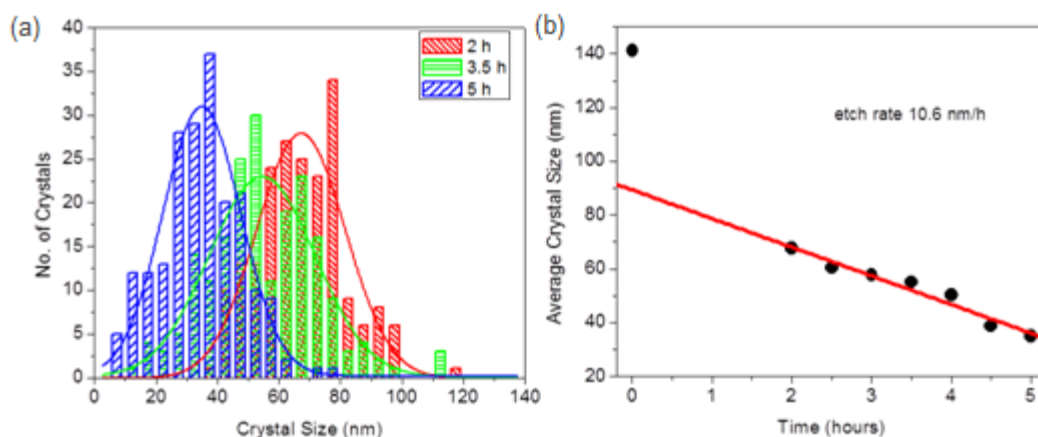
Fig. 2-20 Size reduction as a function of time of nanodiamonds treated in air at 600℃. (a) Histograms of the nanodiamond sizes after a specific oxidation time. These distributions are measured consecutively on the same sample. The solid lines are Gaussian fits to the size distribution. (b) The mean of the size distributions plotted over time. A linear fit (solid line) indicates an etch rate of 10.6 nm/h.

By fitting Gaussians to the height distributions we are able to infer a "mean" crystal size after each step. In Fig. 2-20 (b) the mean sizes are plotted as a function of time and fitted with a line to give the average etch rate. Note that the first step from 0 to 2 h shows a dramatic reduction in crystal size. As discussed, this is due to the rapid etching of non-diamond carbon on the surface and this point is excluded from the linear fit made from 2 hour onward at which point the etch rate is constant. The fit indicates an etch rate of 10.6 nm/h and was determined from 7 consecutive oxidation steps, each one lasting 30 min at 600℃. Figure 2.20 (a) shows the resulting histograms of nanodiamond sizes for 3 different steps within the heating cycles.

When examining the size reduction behaviour of individual crystals, one can see that the etch rate varies somewhat. This effect is visible in Fig. 2-21 where 3 nanodiamonds were tracked over three air oxidation steps. Two of the crystals shrink consistently in

height, but one stays quite constant around 50 nm. However, the relatively crude measure of the X and Y cross sections (i.e. the width of the crystal) of this particular nanodiamond as a function of time does show a reduction. The main reason for this is an anisotropy in the etch rate for different crystallographic planes/surfaces as already observed in CVD diamond samples [61] and natural diamond [62].
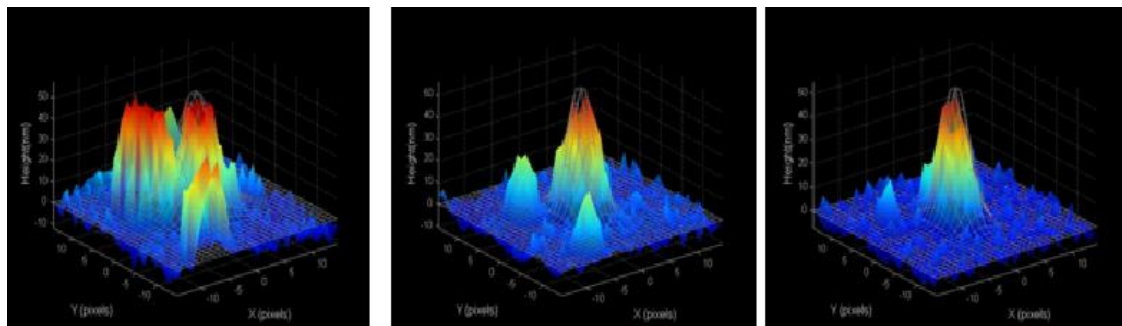
Fig. 2-21 3-dimensional AFM images of the same nanodiamonds following the oxidation steps. The crystal at the centre is not experiencing a reduction in height as much as the other 2 crystals.

More interestingly, with our experimental apparatus, we can now study the size of individual nanodiamond particles hosting NV defects. To do this, we need a confocal image of the nanodiamonds and a corresponding AFM image of the same region. In Fig. 2-22 these images were put together for the untreated sample and two oxidation steps. Not surprisingly one can observe the annihilation of NV defects via air oxidation as layers of carbon are taken away eventually exposing and removing the NV defects themselves.
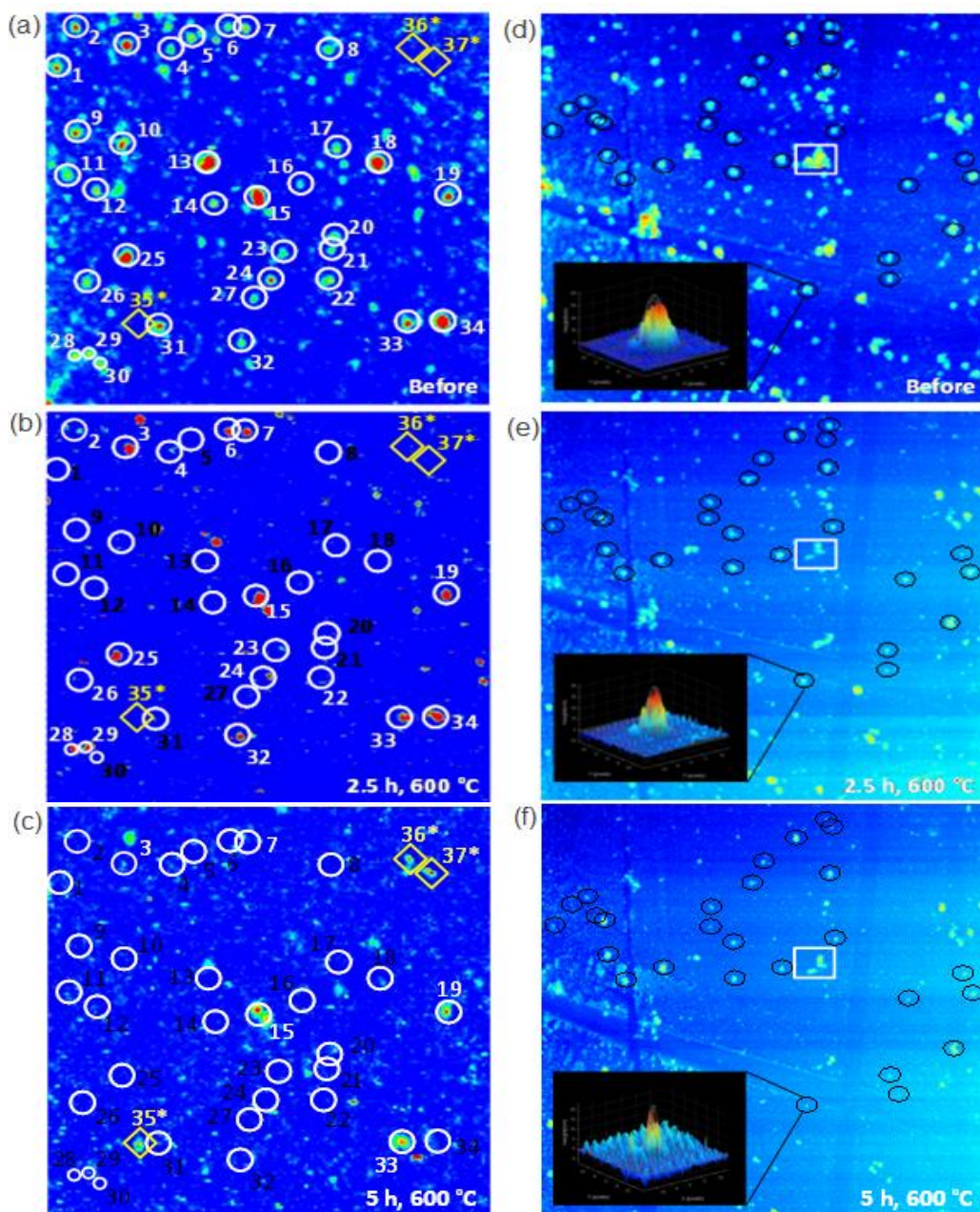
Fig. 2-22 Confocal and AFM images taken after consecutive oxidation steps. (a) confocal image taken before oxidation; the numbered circles indicate some of the NV centres we selected for the analysis. (b) confocal image after annealing the sample in the furnace in air for 2.5 hours at $600\,°C$; the black-numbered circles indicate NV centres which annihilated. (c) confocal image after annealing the sample in the furnace for another 2.5 hours at $600\,°C$. The *-numbered diamonds indicate NV centres which were created by the heating process due to vacancy diffusion to existing N_s sites. (d) AFM image taken before oxidation; the circles indicate some of the crystal we selected for the analysis. (e) AFM image after annealing the sample in the furnace for 2.5 hours at $600\,°C$. (f) AFM image after annealing the sample in the furnace for another 2.5 hours at $600\,°C$. The insets show the reduction in size for the highlighted crystal. The square box shows an example of diamond crystals from being clustered together to being isolated.

With these results we can determine the size distribution of the nanodiamonds hosting NV centers (see Fig. 2-23). Even though the size distribution of the powder used is specified to be ranging from 0 to 100 nm we can find particles up to 170 nm in height. This may be due to aggregation of the nanodiamonds. The air oxidation and the resulting shrinking of the nanodiamonds help to get rid of the aggregates, as shown in Fig. 2-23 the smallest nanodiamond that we observed in this study which still hosted an NV was 8 nm in height. To increase the probability of ending up with even smaller nanodiamonds containing NVs, one needs to increase the starting concentration of available NVs, which can be done by implanting the diamond powder with electrons or ions [32].
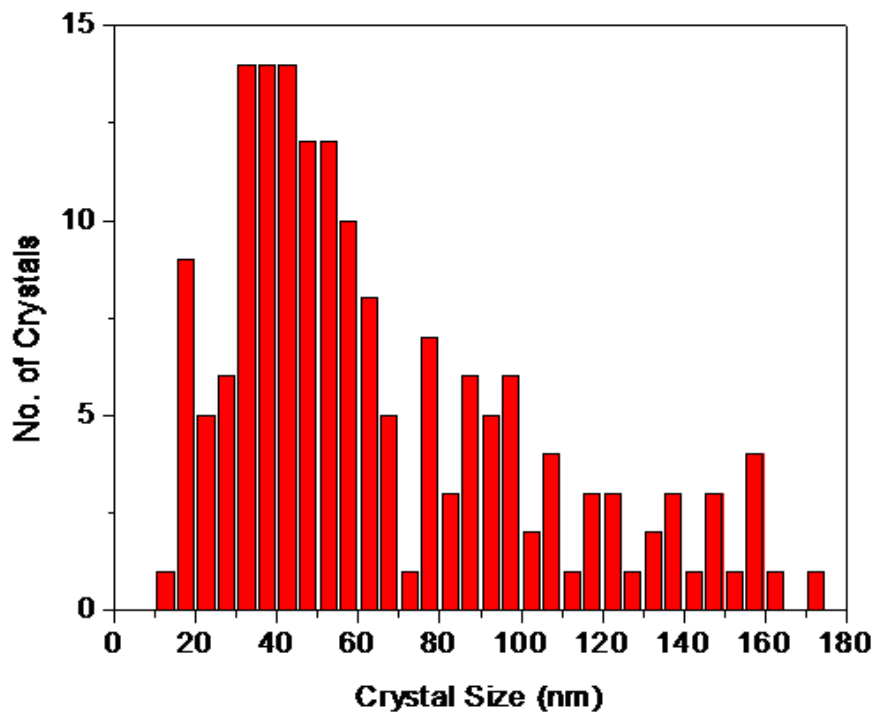
Fig. 2-23 The size distribution of the NDs hosting NV centers.

CHAPTER III

OPTICAL QUENCHING AND RECOVERY OF

PHOTOCURRENT IN SINGLE-CRYSTAL DIAMOND

3.1 Overview

We report the observation of optical quenching of photocurrent in diamond using simultaneous excitation by pulsed and continuous wave lasers, at several wavelengths. The quenched photocurrent showed a recovery related to the external bias voltage, pulsed optical power and wavelength. The recovery of the quenched photocurrent provides information on the nature of the electron trap states in diamond.

With a wide bandgap, high thermal conductance and broadband optical transmittance, diamond has found numerous applications in opto-electronics such as electron emitters [63], windows for high power devices [64], and x-ray photon detectors [65]. Like silicon, diamond can also be doped with various impurities such as boron or phosphorus to create p- or n-type semiconductors [66]. In addition, diamond point defects, such as the nitrogen vacancy (NV) color centers, have applications in the research towards quantum computing [67][68][69], quantum optics [70], and quantum electronics [71][72]. It is thus of paramount importance to investigate photoelectric properties of diamond in greater detail.

Diamond contains a variety of impurities and defects, which can be selectively photo-excited by light of different wavelengths. Also, the photocurrent transient decay rate

depends strongly on the excitation wavelength [73][74] and is often sample-specific. Recent studies of photocurrent focused on the quantum efficiency in nanocrystalline diamond for deep ultraviolet wavelength illumination [75] [76]. Optical excitation and quenching of photocurrent were reported in boron doped epitaxial type IB diamond films with two continuous wave (CW) light sources at different wavelengths [77]. Thus, previous studies are limited in scope.

Herein, we studied optical quenching of photocurrent and photocurrent recovery in bulk undoped IIA diamond. A CW 532 nm laser was found to quench the photocurrent excited by pulsed lasers of various wavelengths, including 532 nm. In addition, the quenched photocurrent was found to be proportional to the CW laser intensity. We also found that the quenched photocurrent recovered when the CW laser was removed and the recovery time was found to be dependent on bias voltage, pulsed laser wavelength, and pulsed laser intensity.

3.2 Experimental methods

The sample studied is a chemical vapor deposition (CVD) IIA single crystal diamond with intrinsic nitrogen concentration of ~ 1 ppm. The sample was irradiated with relativistic electrons and annealed with the initial goal of creating the nitrogen-vacancy (NV) centers; we note that such treatment reduces the concentration of interstitial defects [78] and suppresses surface conduction [79]. For photocurrent measurements, titanium gold electrodes with a gap of 20 μm were deposited onto the surface and a bias voltage of up to 60 V was applied across the electrodes. The photocurrent was either excited with a 532 nm pump pulsed laser (Spectra Physics Q-switched Nd-YAG laser DCR-11 with ~10

ns pulses at 10 Hz repetition rate and 135 mJ pulse energy) or with a tunable dye laser (Quanta Ray PDL-2; pumped by the Nd-YAG laser). The pulsed laser beams were focused to a 20 μm diameter spot in the gap between electrodes, carefully avoiding illumination of the electrodes.
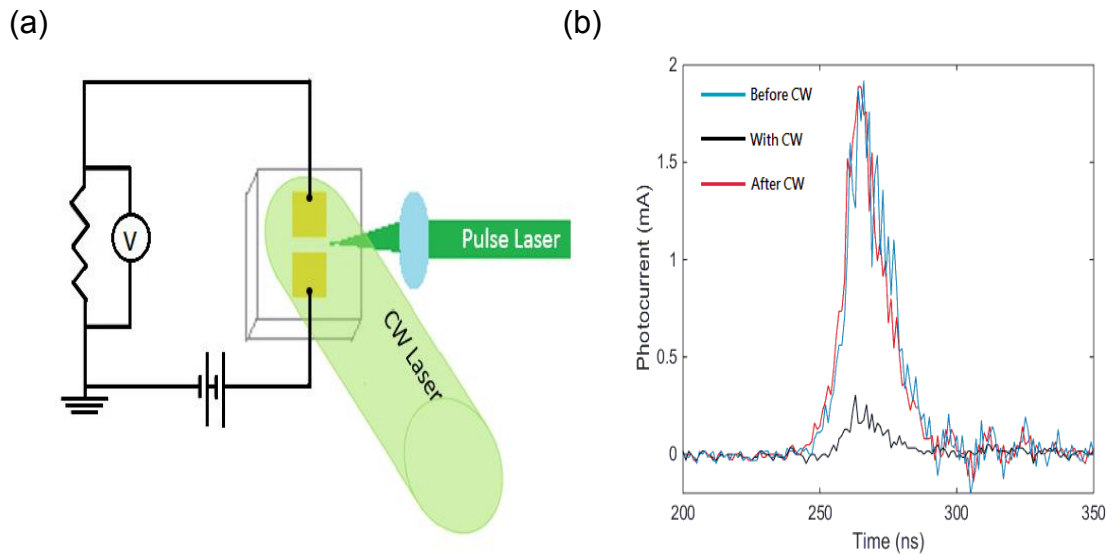
Fig. 3-1 The experimental setup and the time trace of photocurrent produced by 532 nm pulsed laser illumination. (a) The experimental setup. The dye-laser light or the light from the doubled YAG was focused through lens to the side of the diamond where the electrodes were deposited so as not to illuminate the electrodes, while a collimated CW 532 nm laser directly illuminates the whole electrode region. (b) The time trace of photocurrent produced by 532 nm pulsed laser illumination. Blue line: photocurrent with 532 nm pulsed light before turning on CW 532 nm laser. Black line: photocurrent with both 532nm pulsed laser and CW 532 nm laser co-illumination. Red dots: photocurrent with pulsed dye laser alone after shutting off the CW 532 nm laser for 30 seconds.

3.3 Results

The photocurrent resulting from pulsed laser illumination of the sample was

measured using an oscilloscope with a 50 ohm termination. Illumination with 532 nm pulsed light alone induces a pulsed photocurrent of duration ~30 ns. When the sample was co-illuminated with both a collimated 532 nm CW laser at 0.75 W and with the pulsed laser, as shown in Fig. 3-1(a), the photocurrent was quenched by up to 90%. After the CW laser was switched off, the pulsed laser excited photocurrent recovered gradually within about a minute as shown in Fig 3-1(b).

To investigate the dynamics of optical quenching of the photocurrent, we used a quenching/recovery sequence, the timing diagram of which is shown in Fig. 3-2 (top). Initially, the photocurrent induced by the pulsed laser alone is monitored. Then after 10 s the CW laser is switched on, and after another 20 s it is switched off. During the entire sequence a bias voltage of 60 V is applied. The photocurrent induced by the pulsed laser is plotted versus elapsed time in Fig. 3-2 (bottom) for different CW laser powers. To enhance the signal-to-noise ratio, the plotted photocurrent is integrated over the laser pulse duration. The spurious electrical background signal due to the Q-switch trigger pulse was subtracted from the signals. As seen in the graph, the photocurrent amplitude dropped during CW laser illumination and then gradually recovered after removing the CW laser.

The photocurrent quenching effect is approximately linear in CW laser power over the range of powers studied, although there is a slight nonlinearity near the highest and lowest laser powers, as shown in Fig. 3-2 (Inset). The recovery time constant is independent of either the CW laser power or exposure time, but does depend on the voltage and pulsed laser power as discussed below.
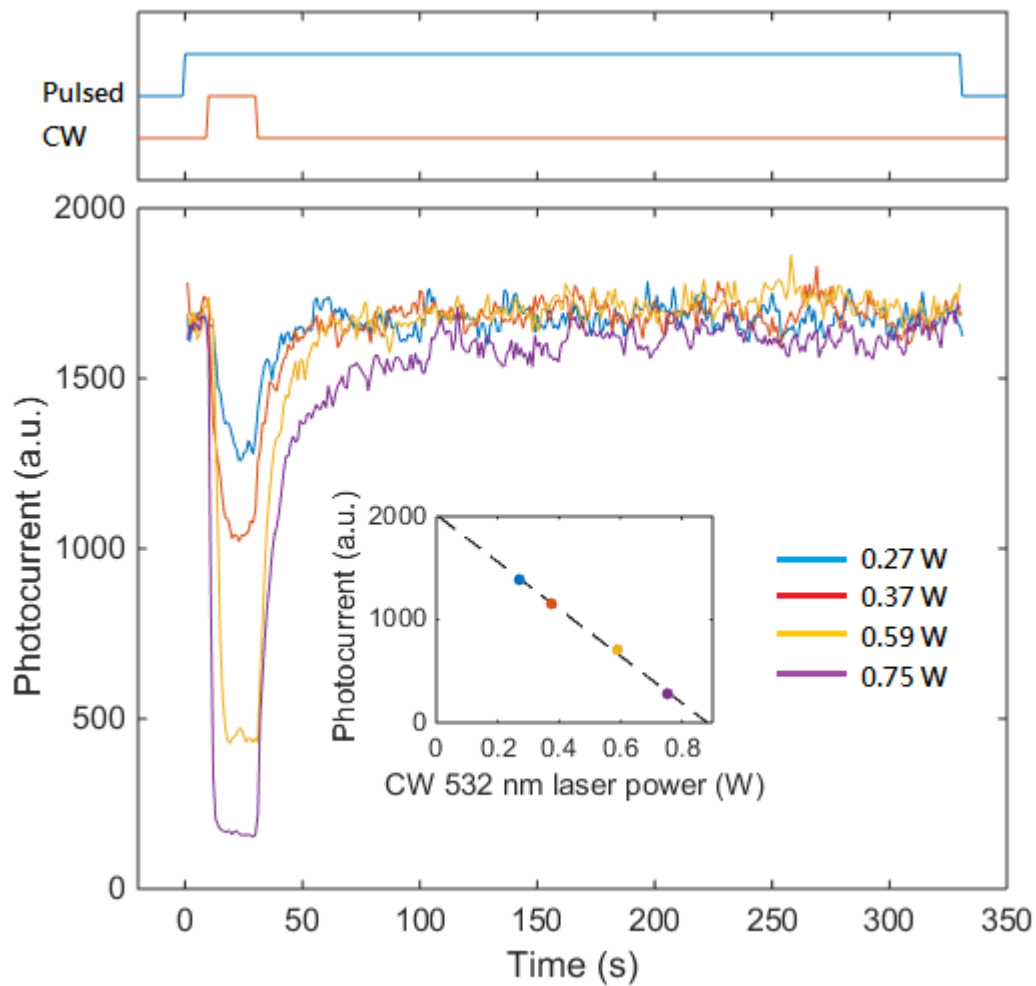
Fig. 3-2 Optical quenching of pulsed photocurrent with CW laser. (Top): Timing for the photocurrent suppression and recovery measurement. The 532 nm pulsed dye laser remained on throughout this experiment, whereas the 532 nm CW laser was only on for 20 seconds. (Bottom): Photocurrent versus elapsed time for different CW 532 nm light powers. Photocurrent suppression by an order of magnitude is observed at the highest laser power. (Inset): Dependence of quenched photocurrent on CW 532 nm laser optical power. The near linear dependence suggests a one-photon process.

3.4 Discussion

The nearly linear dependence of photocurrent quenching on CW laser power suggests

a simple physical explanation: transitions from defect ground state to the conduction band

excited by a single photon provided by the CW laser, followed by electron falling into a trap state. In this scenario, the number of trapped electrons is linearly proportional to total number of incident CW laser photons until equilibrium is reached where the rate of optically induced trapping matches that of the intrinsic trap decay. In other words, the CW laser continuously depletes the defect's ground state population, which is stored in the trap states. Thus, the optical quenching of the photocurrent is linear in the CW laser power until saturation is reached (more than 90% quenching based on our data).

We suggest that photocurrent recovery from quenching may be due to multi-photon excitation of the electrons from the trap state with the pulsed laser light. The CW laser is not intense enough to excite significant numbers of electrons from the trap state at the same rate as the pulse laser.

The photocurrent recovery process as a function of time after removing the CW 532 nm light was fitted with a stretched exponential of the form (Kohlrausch function),

$$I(t) = I_0 \left(1 - e^{-\left(\frac{t}{\tau}\right)^{\beta}} \right)$$
(3.1)

, where $I(t)$ is the time dependent photocurrent, t is the elapsed time since the moment when CW light was turned off , τ is the recovery time constant, and β is a constant. The stretched exponential form as shown in Fig. 3-3 is consistent with the previous studies of transient photocurrent discharging and charging in diamond [80]. Stretched-exponential
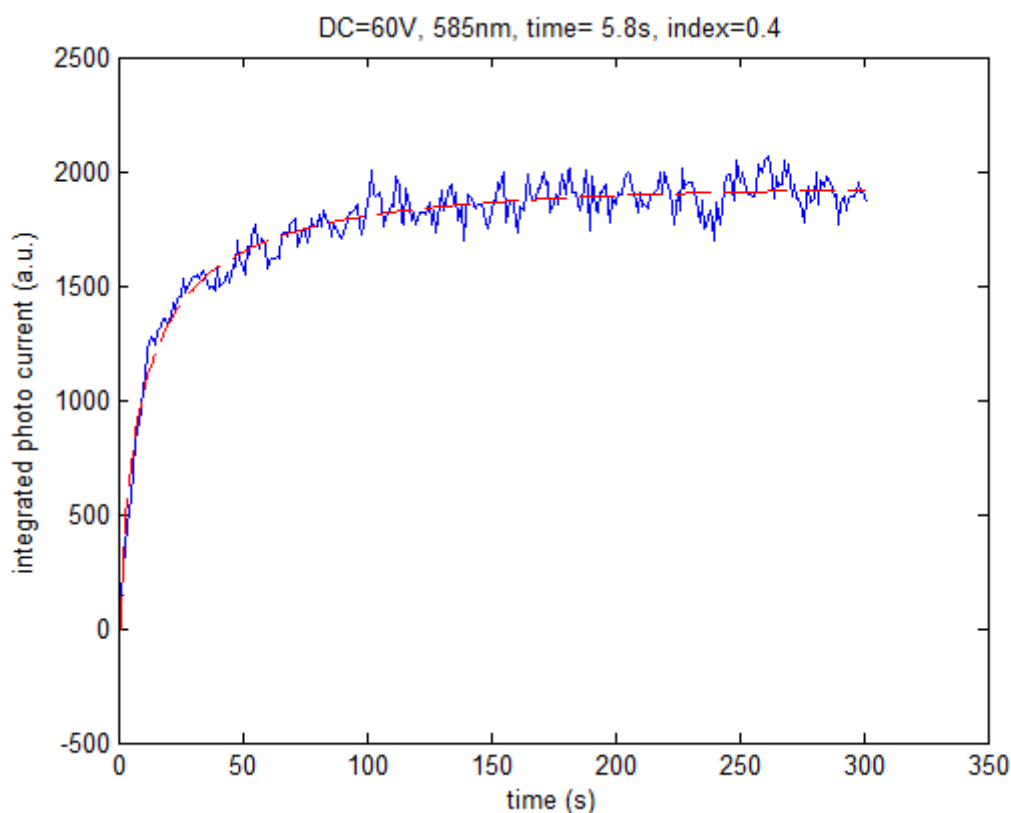
Fig. 3-3 Photocurrent recovery fitted with stretch exponential. The photocurrent was measured with 585 nm pulsed laser excitation and a DC bias at 60 V. The integrated photocurrent is plotted as a function of elapsed time.

fluorescence decay also occurs in some crystalline solids like porous silicon or CdSe-ZnSe [81]. Whether it is due to a time dependent decay rate or a superposition of several exponential decays is still unclear [82]. The fact that the stretched exponential form exists in many materials suggests a common property, related to the charge-trapping kinetics.

The recovery time constant τ is plotted as a function of the DC bias voltage in Fig. 3-4(a) for two pulsed-laser excitation wavelengths: 532 nm and 585 nm. The recovery times at 60 V were 0.8 s and 5.84 s, respectively. At 630 nm, the recovery time takes

68

several hours. The recovery dynamics were found to obey the stretched exponential function with β=0.3~0.9. In general, longer wavelength and smaller voltage results in higher β. The photocurrent recovery time also depends on pulsed laser power, as shown in Fig. 3-4(b) for 532 nm light. The recovery time shortens with increasing pulsed-laser intensity implying that the pulsed laser depopulates the trap. However, even at high pulsed light power, the time dependence of photocurrent recovery still fits better to a stretched exponential function rather than a simple exponential function.
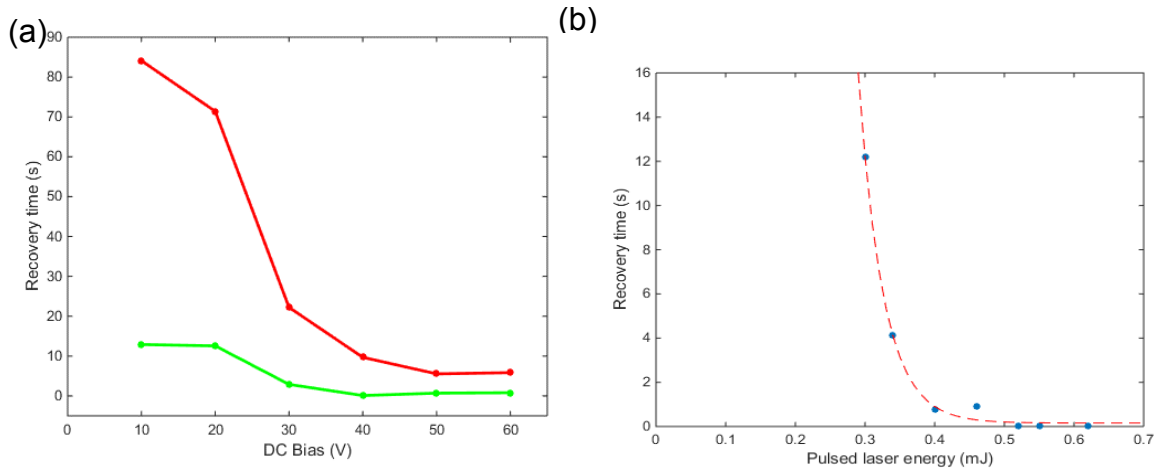
Fig. 3-4 The characteristic recovery time vs DC bias voltage and pulsed laser power. (a): Fitted characteristic recovery time as a function of bias voltage for red and green pulsed lasers. Red: 585 nm laser, and green: 532 nm laser. (b): The characteristic recovery time vs pulsed laser power.

In general, photocurrent density can be expressed as

$$j = en\mu V/d \qquad (3.2)$$

, where *j* is the current density, *e* is the unit charge, *n* is the carrier density, μ is the carrier mobility, and *d* is the sample thickness. In terms of the photon flux, the equation of photocurrent reads

$$j = e\mu\tau\eta\varphi(1 - R)\alpha\,V/d \qquad (3.3)$$

, where τ is the excitation life time, η the photon to electron quantum efficiency, φ the photon flux, R the reflectivity, and α the absorption coefficient. In this work, the photocurrent magnitude in diamond is found to be proportional to the bias voltage, as shown in Fig. 3-5. In addition, due to wavelength dependent optical absorption coefficient and surface reflectivity, the photocurrent magnitude depends strongly on excitation wavelength. On the other hand, we found that the photocurrent recovery time shortens non-linearly but monotonically with increasing bias voltage, suggesting that the higher photocurrent at higher bias voltage depopulates the electron traps faster. This is in contrast to previously reported diamond transient photocurrent decay [73][80] that is voltage independent.

To exclude the possibility of thermal quenching of photocurrent due to heating induced by the CW laser, we varied the delay time between the CW laser turn-on and the pulsed laser turn-on. No correlation was found between delay time and recovery time, which rules out laser-heating effects. Another possible explanation of photocurrent quenching would be that the CW laser shortens the excited state lifetime analogous to what stronger irradiance does to metal enhanced fluorescence [83]. However this can be ruled out by the fact that the pulsed photocurrent time dependence (on the nanosecond time scale) does not change when the CW laser is applied.
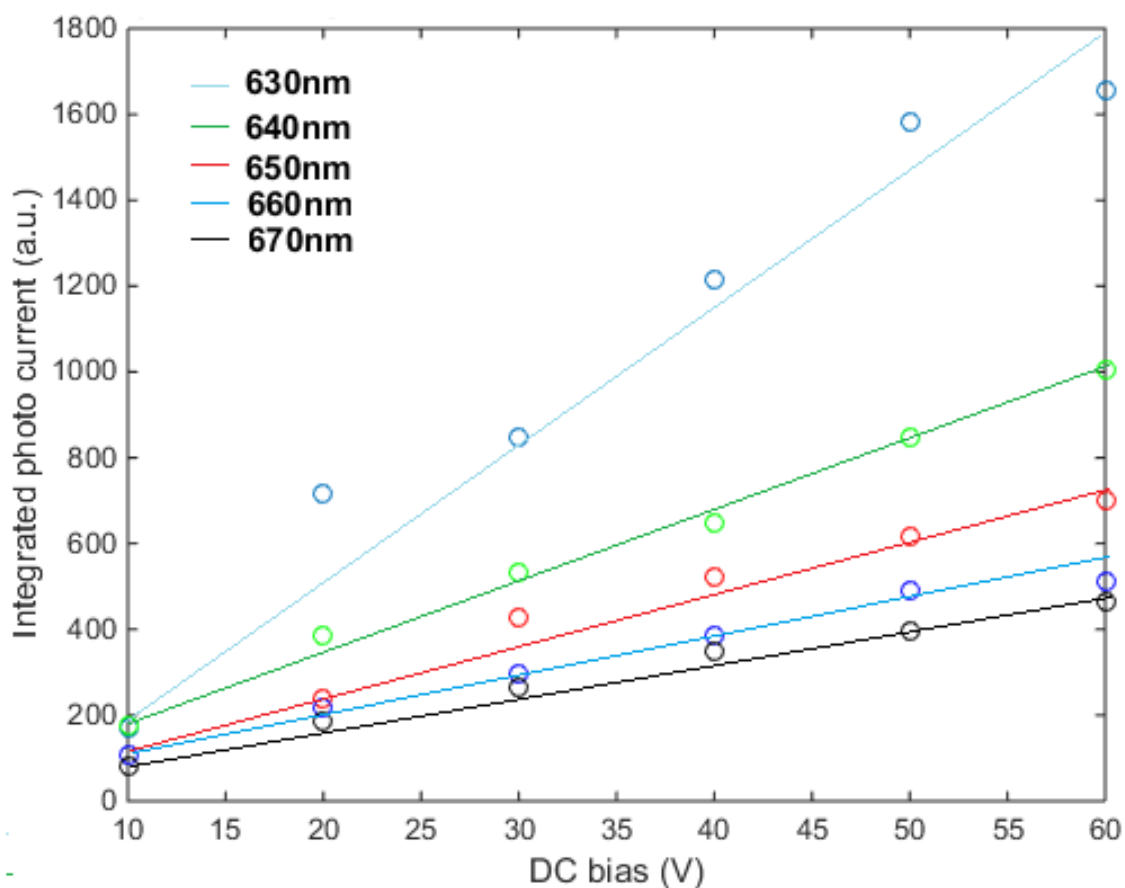
Fig. 3-5 Photocurrent versus DC bias at different wavelengths. Color lines: cyan 630 nm, green 640 nm, red 650 nm, blue 660 nm, and black 670 nm. Linearity can be clearly seen on curve. In addition, the photocurrent-voltage slopes are wavelength dependent.

In our conduction-band-trap model, we assume that substitutional nitrogen atoms are the electron donors. These are the the dominant defects in the type IIA diamond investigated here. For the trap, a system with an intermediate state must exist. This comes from an observation with laser pulses of two colors (red 630 nm and green 532 nm). When a red laser pulse is applied a few nanoseconds after the end of a green laser pulse at a bias

of 60 V, the recovery rate is 3.7 times faster than with green pulse excitation alone. However applying a red pulse alone gives a very slow recovery time of 92 minutes. This can be explained if the trap can only be populated to an intermediate state by green light, but from there it can be excited to the conduction band by red light. A schematic diagram of the proposed model is shown as Fig. 3-6.

In summary, we studied the optical quenching and recovery of photocurrent in a bulk type IIA single-crystal diamond. A nearly linear dependence with a negative slope was observed between the quenched photocurrent and the CW laser power before saturation. Notably, the maximum quenching was as large as 90 %. The recovery time dependence on external bias voltage, light intensity, and wavelength were also investigated in this work. From these data we suggest a model wherein the nitrogen P1 center is being ionized by a single green photon, and the electron trap state can in turn be ionized by two or more photons. Furthermore, the observations are consistent with the trap having a metastable excited state that can only be populated by green excitation but which can then be ionized by absorption of red light.
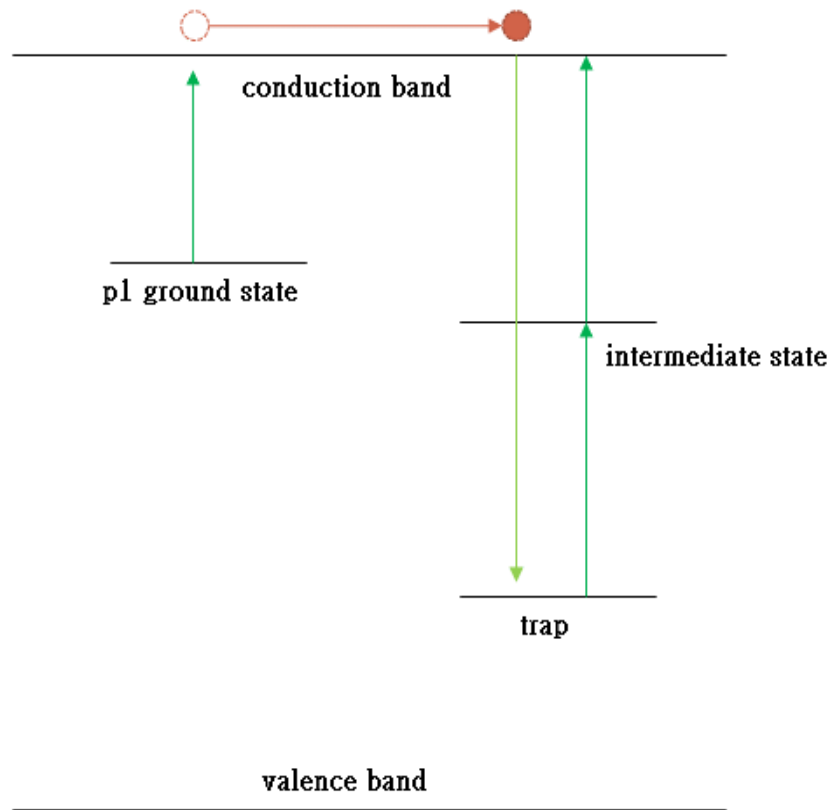
Fig. 3-6 Schematics of proposed electronic trap model.

Of future interest would be a detailed study of the quenching and recovery mechanism, and the exact level structure of the trap. Recently, photocurrent detection of magnetic resonance (PDMR) in the ground-state of the NV- centers was reported [84], however, with a large background of background unrelated to the NV- centers. We are currently investigating whether the quenching effect reported here may be used to increase

the contrast of PDMR, opening the way to practical applications of this detection technique.

CHAPTER IV

PRECISE QUBIT CONTROL BEYOND

THE ROTATING WAVE APPROXIMATION[1]

4.1 Overview

Ultrafast and accurate quantum operations are required in many modern scientific areas - like quantum information processing, quantum metrology and magnetometry. Optimal control theory provides tools to design such operations by finding the best way to transform the system from the initial to the desired state. These quantum gates are often realized as rectangular or Gaussian radio frequency pulses, but their accuracy is limited if the RF amplitude is comparable with the transition energy when the rotating wave approximation (RWA) breaks down. Here we report the theoretical design and experimental implementation of pulses, which do not suffer these limitations. We realized the most common used quantum gates - the Haddamard ($\pi/2$ pulse) and NOT (π pulse) gates with fidelities $F_{\pi/2}^{exp} = 0.95$ and $F_{\pi}^{exp} = 0.99$, respectively, in an excellent agreement with the values expected from the theory. Moreover, we demonstrate that with

---

[1]Reprinted with permission from "Precise qubit control beyond the rotating wave approximation" by Jochen Scheuer, Xi Kong, Ressa S Said, Jeson Chen, Andrea Kurz, Luca Marseglia, Jiangfeng Du, Philip R Hemmer, Simone Montangero, Tommaso Calarco, Boris Naydenov and Fedor Jelezko, New Journal of Physics 16, 093022 (2014). Copyright 2014 IOP Publishing Ltd and Deutsche Physikalische Gesellschaft

these pulses magnetic resonance experiments are possible also beyond the RWA. Since our method is general, we believe that it could find a wide application in quantum computing, quantum optics and broadband magnetometry.

Strong driving of spins allows to increase the number of qubit operations before detrimental effects of decoherence take place, and it may further increase the badnwidth of spin based magnetometers. For the implementation of the new pulses we used the electron spin associated with a single Nitrogen-Vacancy (NV) center in diamond, due to its remarkable properties: the optical spin initialization and readout at room temperature, coherent spin control via microwaves (MW), and the milliseconds coherence time [85][86]. This system is very promising as a nano-scale high ultrasensitive magnetometer [51][87][88] and solid state qubit [89][90]. Strongly driven dynamics of the NV has been already observed using conventional pulses on resonance [91] achieving nanosecond spin flips and a possibility for improvement has been proposed [92].

Here we demonstrate a precisely controlled strong single electron spin rotations using numerically optimized microwave fields. We realize the two most important single spin gates, without necessarily resorting to the standard RWA condition. Moreover, the rotations performed are faster than that of the Rabi oscillation while using the same MW amplitude. To achieve this we employ a practical optimal control method, namely chopped random-basis (CRAB) quantum optimization algorithm [93][94]. The CRAB~algorithm numerically designs and optimizes the microwave controls. In contrast to the previous proposed iterative method for robust fast entanglement generation using weak control

fields in diamond [95], our current algorithm uses a simple derivative-free direct search method to perform a multivariable function optimization [94], and hence offers more computational flexibility such as parallel numerical optimizations.

4.2 Experiment methods

The NV consists of a substitutional nitrogen atom and an adjacent vacancy with a triplet ground state (S=1) and a strong optical transition, where single centers can be addressed. Moreover, its fluorescence depends on the electron spin state, allowing to perform coherent single spin control [96][97]. The ground state Hamiltonian in the presence of MW control $\Gamma_x(t)$, can be written as:

$$\frac{\hat{H}}{h} = D\hat{S}_z^2 + \omega_z\hat{S}_z + \sqrt{2}\Gamma_x(t)\hat{S}_x \tag{4.1}$$

, where D $\approx$ 2.87 GHz is the NV's electron zero-field splitting (ZFS), and ω_z is Zeeman splitting due to a constant magnetic field B_z [92]. It is important to mention here that the Hamiltonian is necessarily written in the lab frame since the control amplitude is comparable to the Larmor frequency of the spin, i.e. $\left\{ \left| \Gamma_x(t) \right| \right\} \sim \omega_L$ (where $\omega_L = D - \omega_z$), and hence the counter-propagating term of the control can not be neglected [91]. To fulfill this condition and to work with the approximated two-level spin system of $|m_s = 0\rangle$ and $|m_s = -1\rangle$, we apply a magnetic field $B_z = 1017.3\,G$ (101.73 mT) and set the working transition frequency to $\omega_L = 30$ MHz, see also Fig. 4-1 (a).

We first perform Rabi oscillations at different MW amplitudes and observed the spin

dynamics, Fig. 4-1(c). When the driving field $\Omega < \omega_L/2$, the system is in the RWA regime and nice harmonic signal is obtained (Fig. 4-1(c), lower right inset). However, if $\Omega > \omega_L/2$ then the signal is anharmonic as shown in (Fig. 4-1(c), upper left inset) and precise control over the spin rotations is difficult [91].

To perform a desired spin rotation which follows the Schrödinger equation, $\frac{d}{dt}|\psi(t)> = -i\hat{H}|\psi(t)>$ (assuming =1), we optimally engineer the control $\Gamma_x(t)$, such that at the final time T, the state fidelity between the final spin state $|\psi(t)>$ and the target $|\psi_T>$ is maximized. The fidelity F is defined as [98]:

$$F = \sqrt{\langle \psi_{target}|\rho_{CRAB}|\psi_{target}\rangle} \tag{4-2}$$

with ψ_{target} and ρ_{CRAB} being respectively the target and the expected after the CRAB pulse state.

Our method designs the control $\Gamma_x(t)$ by correcting an initial guess $\Gamma_0(t)$ with an optimized continuous function g(t), following $\Gamma_x(t) = \Gamma_0(t)g(t)$ [93, 94]. In this work we use a constant initial guess $\Gamma_0 = 1$. The correcting function g(t) can be expanded into a Fourier-like basis,

$$g(t) = \frac{1}{2N\lambda}\sum_{n=1}^{N}\{a_n \sin(\omega_n t) + b_n \cos(\omega_n t)\} \tag{4-3}$$

, where N denotes a number of frequencies. We note here that the range of frequencies

(ω_1, ω_n) directly corresponds to the real bandwidth of the apparatuses limited by the MW amplifier. The additional function $\lambda(t)$ is used to force the control boundary such that $\Gamma_x(t) = 0$ for t = 0. We choose the bounding function $\lambda(t) = h^p/(h^p - (t - h)^p)$

, where h=T/2. Using this function we can vary the rising and falling times of the MW control by adjusting the even-numbered parameter p qualitatively. A direct search simplex algorithm (Nelder-Mead) is then applied to find the set of CRAB parameters

$\{a_n, b_n, \omega_n\}$ which minimizes a figure of merit, $\mathcal{F} = 1 - f + c_f max\{|\Gamma_x(t)|\}$

, where $f = |\langle \psi(t)|\psi_T \rangle|^2$. We incorporate a quantity c_f to limit the control amplitude during optimization.

The numerical optimization is initiated by setting some parameters obtained from the experimental preparations and apparatus calibrations: the measured Larmor transition ω_L, the maximum control amplitude $\{|\Gamma_x(t)|\} = \Omega$, and the CRAB frequency range. We fix the control time (the same as the desired rotation time) to be faster than the extrapolated rotation time if the RWA would be valid, e.g. for the spin π-rotation we have$T < 1/2\Omega^{-1}$, where Ω is the extrapolated Rabi frequency (see Fig. 4-1(c)). However, the π-rotation time can not be faster than the optimal time of the theoretical bang-bang control, $T_\pi^{Bang} = \pi/\sqrt{(\pi\omega_L)^2 + (2\pi\Omega)^2}$ [99].
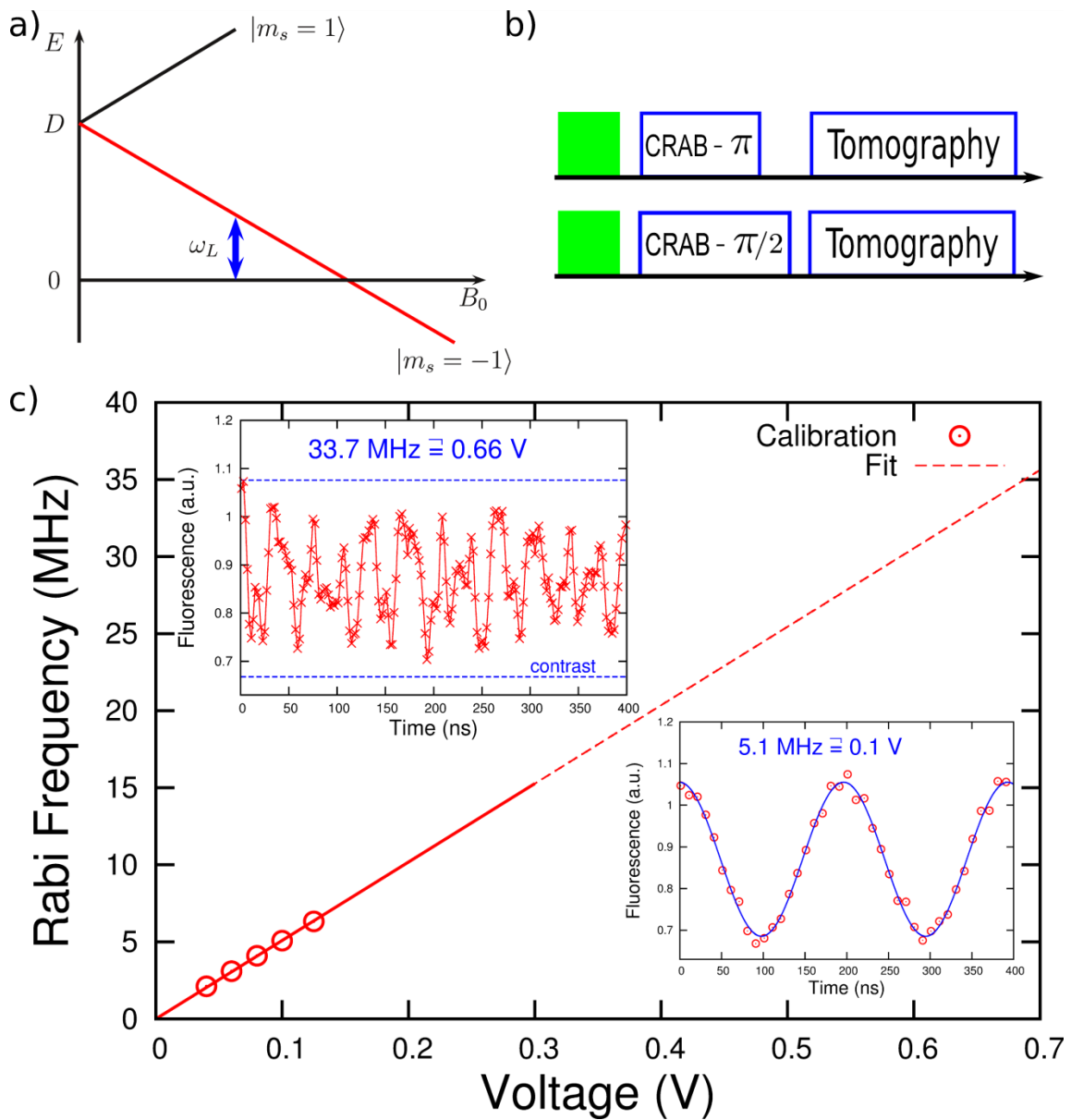
Fig. 4-1 NV energy levels diagrams, pulse sequence for state tomography, and Rabi frequency versus MW amplitude. (a) Energy of the $|m_s\rangle$ state of the NV center as function of the applied static magnetic field B_0. $\omega_L \sim$ MHz is the frequency of the transition we used in our experiments. (b) Schematic representation of the pulse sequences for the density matrix tomography. At beginning and at the end we always apply a laser pulse to polarize the NV in $|m_s = 0\rangle$ and then to read out the state of the electron spin. Experimental implementation of CRAB π (a) and $\pi/2$ (b) pulses. The tomography is performed by applying $\pi/2$ pulses along the x and y axis of the rotating frame. (c) Rabi frequency as a function of the MW amplitude. The markers denote the region where harmonic behavior is observed as shown in the lower left inset. The line is a linear fit, its dashed part shows the region where the spin dynamics is anharmonic (upper right inset).

To obtain the optimized pulse for one target rotation, we do the following steps:

(1) Perform the parallel simplex search algorithm with an S number of random initial values of the CRAB parameters for j small positive real numbers of $\{c_f^j\}$, and k positive small integers $\{N_k\}$, typically $\{c_f^j\} \in (0.01, 0.5)$, and $\{N_k\} \in (3, 7)$.

(2) Obtain from step 1, $(S \times j \times k)$ sets of CRAB parameters, than construct $(S \times j \times k)$ numbers of control pulses $\{\Gamma_x(t)\}$.

(3) Investigate the numerical values of $\mathcal{F}$ and max $\{|\Gamma_x(t)|\}$ for each pulse, and pick the best one out of $(S \times j \times k)$ pulses which satisfies $\mathcal{F} \leqslant k_f$ and max $\{|\Gamma_x(t)|\} \leqslant k_\Gamma$. The preset quantities k_f and k_Γ are the numerical infidelity and the maximum control amplitude, respectively. If the best pulse can not be obtained, return to step 1 with different values of $\{c_f^j\}$ and increase $\{N_k\}$.

For one target state rotation, we run the Nelder-Mead simplex search algorithm in parallel for few randomized initial values of the CRAB parameters $\{a_n,\ b_n,\ \omega_n\}$, and adaptively change the limiting quantity c_f at a fixed value of N until we find the best parameters, hence obtaining the numerically optimized control. The typical computational time required to meet the experimentally acceptable fidelity is approximately less than 30 min. This allows one to perform a single optimization run in just a decent commercial personal computer. Hence, it is feasible in the future to apply our numerical CRAB optimization in standard close-loop control system involving directly the control apparatuses. For both cases of π-rotation and π 2-rotation we set the parameters as the following: N = 5, S = 30, $\omega_L = g_0 = $ max $\{|\Gamma_x(t)|\} = 30$ MHz, and $\omega_n \in (10, 100)$ MHz. We

present the best obtained CRAB parameters for each rotation in Table. 4-1.

Table. 4-1 The optimal CRAB parameters obtained via the Nelder–Mead simplex algorithm for π- and π 2-rotations.

π -rotation			$\pi/2$-rotation		
$T = 15.4071$ ns, $p = 60$, $c_f = 0.35$			$T = 7.7036$ ns, $p = 38$, $c_f = 0.23$		
a_n	b_n	ω_n (GHz)	a_n	b_n	ω_n (GHz)
$a_1 = -5.4865$	$b_1 = 0.2812$	$\omega_1 = 0.0201$	$a_1 = 2.1123$	$b_1 = 9.6205$	$\omega_1 = 0.0149$
$a_2 = 2.4803$	$b_2 = 1.8823$	$\omega_2 = 0.0415$	$a_2 = -5.5973$	$b_2 = -28.736$	$\omega_2 = 0.0401$
$a_3 = -0.5404$	$b_3 = 5.8533$	$\omega_3 = 0.0513$	$a_3 = -9.7577$	$b_3 = -3.9425$	$\omega_3 = 0.0464$
$a_4 = 1.5659$	$b_4 = -2.212$	$\omega_4 = 0.0687$	$a_4 = 26.346$	$b_4 = 5.4267$	$\omega_4 = 0.0664$
$a_5 = 1.4673$	$b_5 = 3.6469$	$\omega_5 = 0.0892$	$a_5 = -10.421$	$b_5 = 7.2445$	$\omega_5 = 0.0909$

Here we used CRAB controls to implement the two most important single-qubit rotations - flipping the qubit (NOT-gate, π pulse) and creating superposition between the qubit states (Hadamard gate, $\pi/2$). The experimental realization of these rotations is shown schematically in Fig. 4-1(b). Since the spin system has to be treated in the lab frame, its dynamics is more complicated. Fig. 4-2 shows the calculated trajectory of the spin movement during the CRAB-π pulse.

In order to determine the fidelity of the final state in respect to the target state we

performed a state tomography. For this purpose we evaluated all three components of the

Bloch vector. The z-component is measured directly from the fluorescence level. The x-

and y-components have to be projected into the measurable z-component.
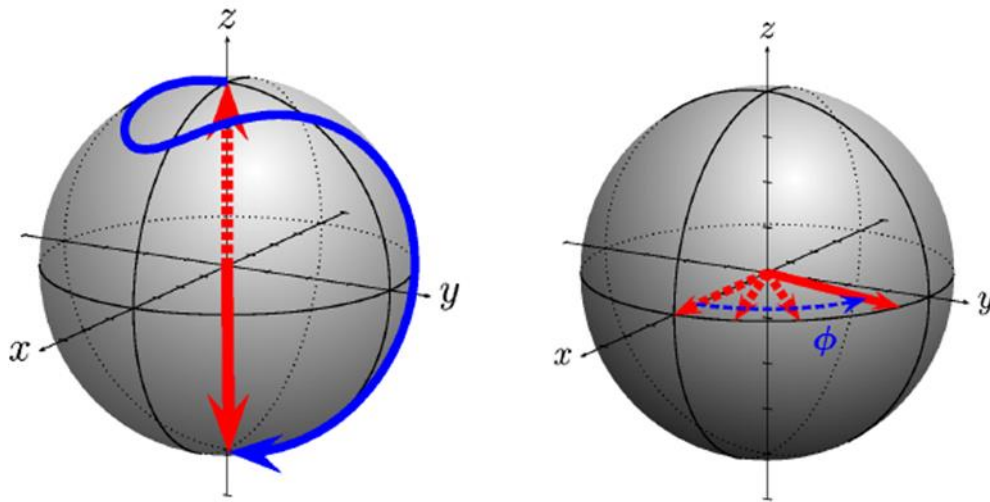
Fig. 4-2 The spin magnetization trajectory after application of the CRAB pulse. (left) The trajectory of the spin magnetization (blue curve) during the application of the CRAB π pulse. The initials state is $|m_s = 0\rangle$ (red dashed arrow) and the target state is $|m_s = -1\rangle$ (red solid arrow). The points have been calculated using the Schrödinger equation. (right) After the CRAB $\pi/2$ the spin magnetization lays in the xy plane of the lab frame, parallel to the x axis. Then it rotates around the z with an angular velocity ω_L (Larmor frequency), acquiring a phase $\varphi = e^{-i\omega_L t}$.

This is done by applying a MW with different phases and measure Rabi oscillations

or in other words: rotate the Bloch vector around the x axis to determine the y-component

and vice versa, as shown in Fig. 4-3. The density matrix of a single qubit can be written
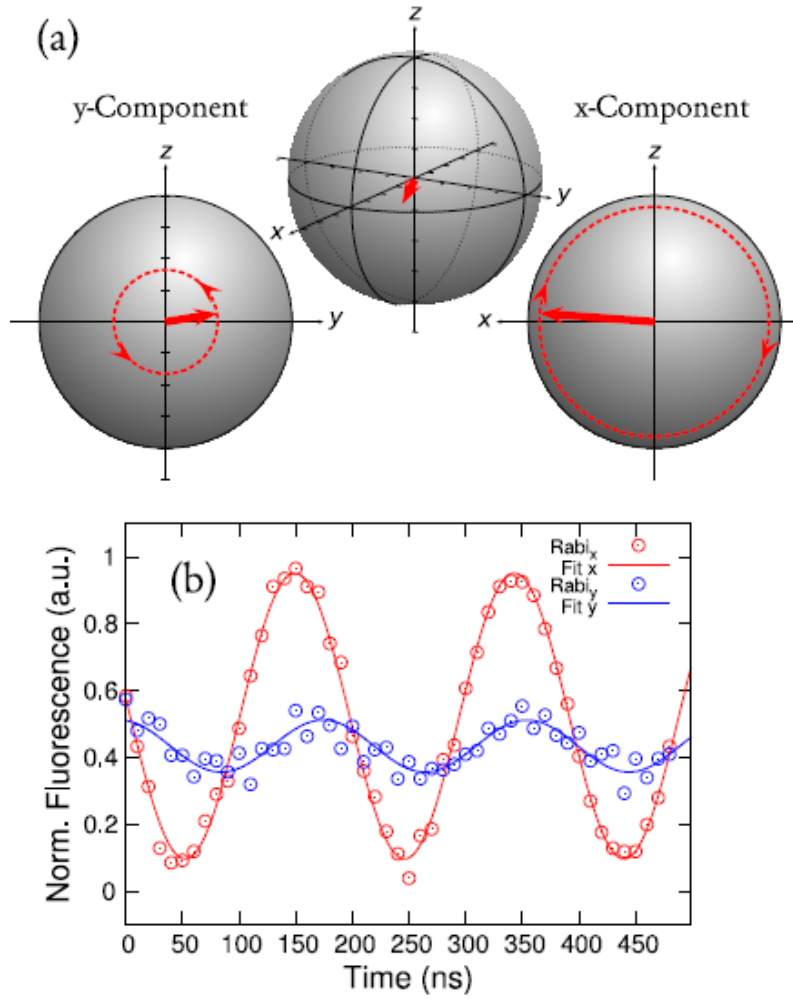
Fig. 4-3 State tomography. (a) The state is characterized by performing Rabi oscillations by rotating the spin around the x- and y-axis. The z-component can be observed by measurement without application of a microwave. With the amplitude and the z-component the x- and y-component can be calculated simply using the Pythagorean theorem. (b) Measurement data of the state tomography after the CRAB-π 2-pulse.

as

$$\rho = \frac{1}{2}\begin{pmatrix} 1+z & x+iy \\ x-iy & 1-z \end{pmatrix} \tag{4.4}$$

In this definition, x, y and z have values between -1 and 1. The first point of the

measurements Rabi$_x$ (1) and Rabi$_y$ (1), where no MW was applied, can be understood

as the z-component. The three components of the Bloch vector are calculated following

$$z = \text{Rabi}_x(1) + \text{Rabi}_y(1) - 1 \tag{4.5}$$

$$y = \sqrt{(2Amp_y)^2 - z^2} \tag{4.6}$$

$$x = \sqrt{(2Amp_x)^2 - z^2} \tag{4.7}$$

where *x*, *y* and z are the three components of the Bloch vector and Amp$_{x,y}$ are the

amplitudes of the Rabi oscillations rotating around the y, x-axis respectively. In formula

(4.6) and (4.7), values for x and y were set to 0 if the uncertainty was greater than the

actual value. Another possibility to obtain the x- and y-component is to calculate Rabi$_x$

($\pi/2$) and Rabi$_y$ ($\pi/2$) respectively.

To normalize the data we performed an additional, bare Rabi measurement. The

normalization is done by Rabi$_x$ (1) = (rawdata(1) − (y_0 − A)) 2A, where A is the amplitude

and y_0 is the offset of the normalization measurement. In order to calculate the fidelity

between the experimental state ρ and the target state $|\Psi\rangle$ the definition for pure states is

used: $F = \sqrt{\langle \Psi|\rho|\Psi\rangle}$ which in this case is equivalent to the general definition F =

$\text{tr} \sqrt{\sqrt{\sigma}\rho\sqrt{\sigma}}$ [98].

Due to experimental limitations we had to wait for 100 ns between the CRAB-pulse

and the Rabi measurement, hence the target state after the time evolution on the *x*, *y* plane

becomes

$$|\Psi(t)\rangle = e^{-\frac{i}{2}\sigma_z \omega_L t}|\Psi(0)\rangle \tag{4.8}$$

with the Pauli matrix σz and the Larmor frequency ω_L.

For the error calculation of the fidelity, the noise of the Poisson distributed photon collection and fitting errors were taken into account. The error was determined by using the general law of error propagation [100]:

$$\Delta F = \sum_{k=1}^{N} \left(\frac{\partial F}{\partial f_k}\right)^2 var(f_k) + 2 \sum_{l=1}^{N-1} \sum_{m=l+1}^{N} \left(\frac{\partial F}{\partial f_l}\right) \left(\frac{\partial F}{\partial f_m}\right) covar(f_l, f_m) \qquad (4.9)$$

The pulses optimized by the CRAB algorithm is a superposition of ten periodic functions. In the experiment, these pulses are synthesized directly by an arbitrary waveform generator (AWG, Tektronix AWG7122C) with a sampling rate of 24 GS s−1 and then sent to an amplifier (Mini-Circuits, ZHL-42W-SMA).

The pulse shapes measured via an oscilloscope (Tektronix, TDS6804B) are displayed in Fig. 4-4. Optical measurements were obtained via a self-made confocal microscope, the AWG triggered both the acousto-optic modulator for laser pulse control and the photon-count card (FastComtec P7887).

4.3 Results and discussion

We performed a density matrix tomography in order to determine the quality of the optimized pulses. The two off-diagonal elements have been measured by applying a $\pi/2$ along the x and y axis of the rotating frame, followed by a laser pulse for read out (see also Fig. 4-2, right). For the diagonal elements the MW pulses have been omitted. After the CRAB-π pulse theoretically expected and the experimentally measured density matrices are:

$$\rho_{theory}^{\pi} = \begin{pmatrix} 0 & 0 \\ 0 & 1 \end{pmatrix}, \quad \rho_{exp}^{\pi} = \begin{pmatrix} 0.01 & 0.04 - 0.04i \\ 0.04 - 0.04i & 0.99 \end{pmatrix} \quad (4.10)$$
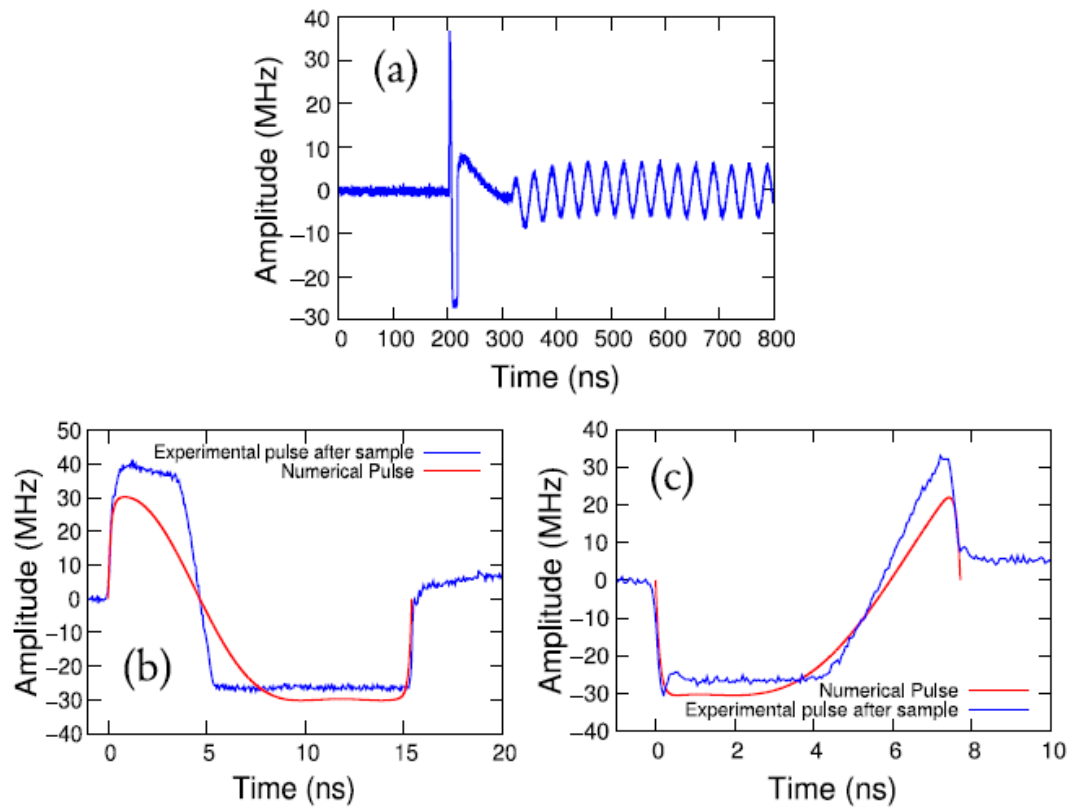
After the $\pi/2$ pulse we expect:

Fig. 4-4 Pulse shapes. (a) Oscilloscope measurement of the signal after the diamond sample with the standard sinusoidal microwave after 100 ns delay to measure Rabi oscillations for the state tomography. (b) CRAB-π pulse (blue) in comparison to numerical pulse (red). (c) CRAB-$\pi/2$ pulse (blue) in comparison to numerical pulse (red).

$$\rho_{theory}^{\pi/2} = \begin{pmatrix} 0.5 & 0.5 \\ 0.5 & 0.5 \end{pmatrix} \tag{4.11}$$

This is the state of the system directly after the MW pulses. However, due to technical limitations the measurement can be performed only after some time $t_{evol} = 100$ ns. During this time the spin rotates in the xy plane in the lab frame and acquires a phase $\varphi = e^{-i\omega_L t}$ (see Fig. 4-2, right). The density matrix after t_{evol} is then:

$$\rho_{theory}^{\pi/2} = \begin{pmatrix} 0.5 & 0.06 - 0.5i \\ 0.06 + 0.5i & 0.5 \end{pmatrix} \tag{4.12}$$

From the tomography we obtain:

$$\rho_{exp}^{\pi/2} = \begin{pmatrix} 0.43 & 0.08 - 0.43i \\ 0.08 + 0.43i & 0.58 \end{pmatrix} \tag{4.13}$$

The expected fidelities of the CRAB pulses are $F_{theory}^{\pi} = 0.9986$ and $F_{theory}^{\pi/2} = 0.9545$, whilst from the experiment we obtain $F_{exp}^{\pi} = 0.993$ and $F_{exp}^{\pi/2} = 0.959$. All these values are calculated using eq. 2 with respect to the corresponding target state. We find an excellent agreement betweeen the theoretical prediction and the experimental result. The discrepancy between the two can be explained by deviation from the ideal pulse shape due to the limited bandwidth of the MW amplifier.

The pulses we have developed in this study are important not only for quantum information processing, but also for most of the pulsed Nuclear Magnetic Resonance (NMR) and Electron Spin Resonance (ESR). Although they were not specifically developed as gates, but just to transfer the spin from $|m_s = 0>$ to some desired state.

Nevertheless they are very robust and can be used for magnetic resonance as we show below. One of the most important NMR (and ESR) pulse sequence consists of a single $\pi/2$ pulse, where the spin magnetization is rotated from the z-axis to the xy plane in the rotating frame. The spins then precess and can be detected by the NMR detector resulting in the Free Induction Decay (FID).

The Fourier transform of the latter provides the spectrum of the sample [101][102]. Since we drive the electron spin very fast ($\Omega = \omega_L$), we can performed this experiment both in the lab and in the rotating frame. All sequences begin with a laser pulse. In the first experiment (Fig. 4-5 top) we start with a CRAB $\pi/2$, which rotates the spin magnetization around the x axis of the lab frame. After a free evolution time τ we apply another CRAB $\pi/2$ pulse to rotate the spin back to the z axis and we then read out optically the spin state. The signal oscillates with the Larmor Frequency ω_L (see also Fig. 4-2, right). The next experiments are the same, but the second pulse has much lower amplitude and the system is effectively in the rotating frame. If the phase of the MW is $\varphi = 0$, the phase acquired during the free evolution period τ increases and the signal again oscillates with ω_L (Fig. 4-5 bottom, blue curve). However, if the phase of the second pulse is $\varphi = e^{i\omega_L t}$, than the phase increment is compensated and it "follows" the spin in the xy plane. In this case the observed FID (Fig. 4-5 bottom, black markers) is identical with the one measured in the rotating frame. Thus we can on demand "switch" between the lab and rotating frames.
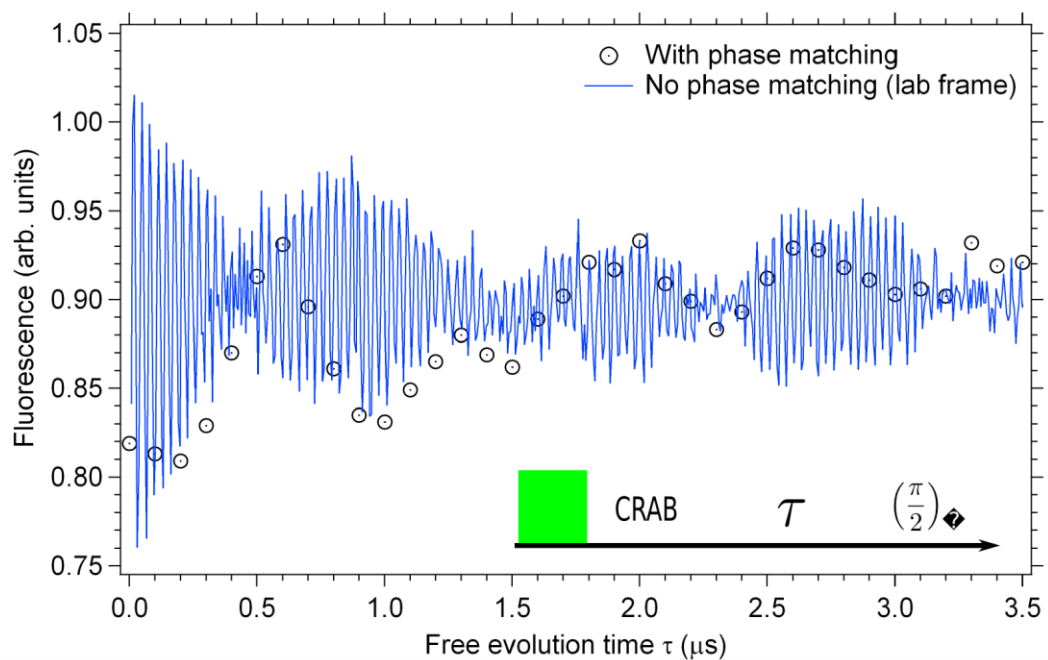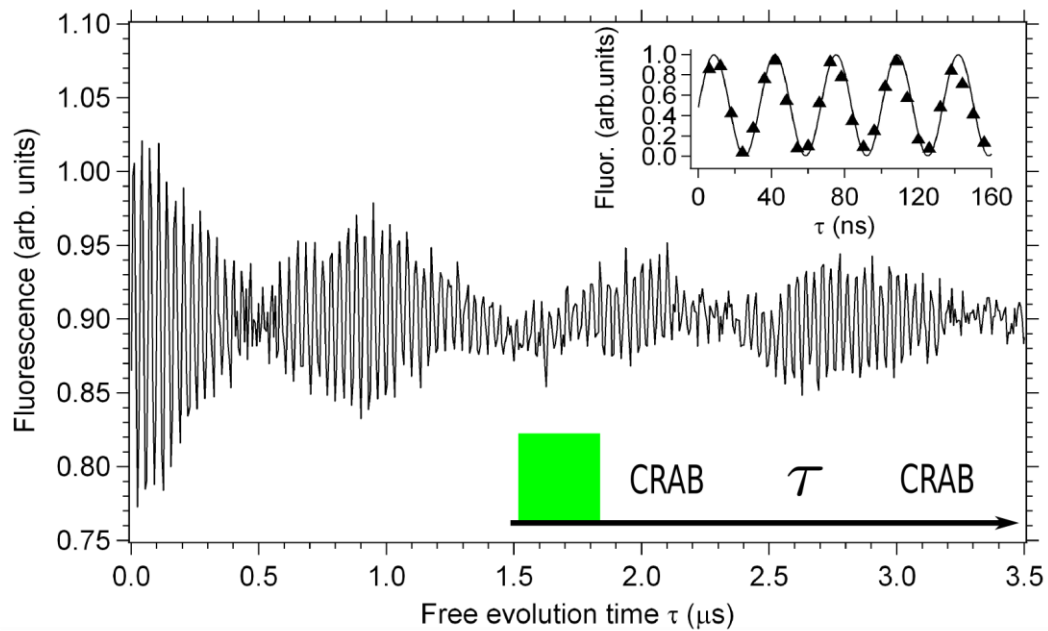
Fig. 4-5 Free induction decays - experimental data. (top) FID measured by using two CRAB $\pi/2$ pulses. The inset shows the first 160 ns of the signal (markers) and a the calculated fidelity with respect the $|m_s = 0\rangle$ state. (bottom) FID measured by using a CRAB $\pi/2$ pulse and a low power pulse with fixed phase (blue curve) and increased phase (markers) for each point (see text for more details). The lower frequency component ~2 MHz is probably due to coupling to a distant ^{13}C nuclear spin.

Another important method in the magnetic resonance is the Hahn echo [103], which has found a wide application in ERS and NMR. It is the basis of all dynamical decoupling techniques and has been recently implemented for AC magnetometry [51,86]. The Hahn echo pulse sequence is depicted in figure 4a. The CRAB-$\pi/2$ pulse rotates the initial magnetization in the xy plane, where it evolve for a time τ_0 when a CRAB-π pulse is applied. After a time τ the spin state is transformed to the z axis by a CRAB-$\pi/2$, where it is read out by a laser pulse. In this experiment all static inhomogeneous shifts (and fluctuation on the time scale of the coherence time T_2) are effectively canceled out. Usually it is performed in the rotating frame using rectangular (sometimes Gaussian) pulses, but here, due to the large MW amplitude, we work in the lab frame. The spin signal oscillates with the Larmor frequency of the NV transition (in this case $\omega_L = 120$ MHz) is shown in Fig. 4-6(b). The envelope of the echo corresponds to the echo measured in the rotating frame at same magnetic field.

In summary, we have developed a novel method for precise spin qubit rotations in the ultrafast driving regime where the standard pulses are not applicable. We designed our qubit gates by using the quantum optimization algorithm CRAB and find an excellent agreement with the experimental implementation. Moreover, we demonstrate that it is possible to perform the basic magnetic resonance experiments in this conditions, where the rotating frame approximation breaks down. To our knowledge, this is the first demonstration of magnetic resonance in the laboratory frame. Our results reported here could find a wide application for quantum computation and broadband magnetometry.
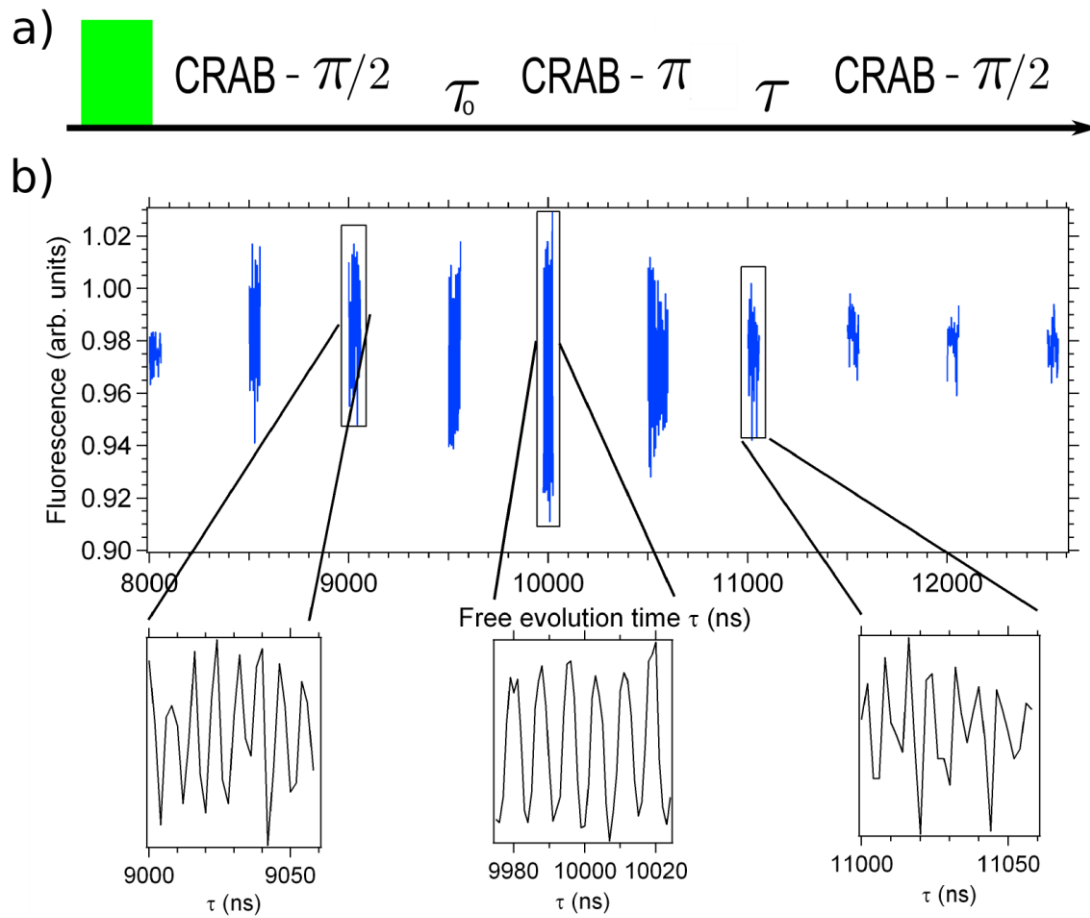
Fig. 4-6 The Hahn echo experiments. (a) The pulse sequence for the Hahn echo. (b) Parts of the Hahn echo of a single NV in the lab frame (blue curves). This signal oscillates with the Larmor frequency ($\omega_L = 120$ MHz here), as shown in the three insets.

CHAPTER V

CONCLUSION

With the ability to optically detect the electric field, magnetic field, strain force, and temperature, the NV centers in diamonds are the choice for all-purpose detectors. In addition, various kinds of super resolution imaging has been implemented with nanodiamonds. Furthermore, a diamond as a candidate for next generation quantum computer has showed great potential. Therefore, the characterization and detailed study of diamonds becomes a priority in science. In this dissertation, quantum engineering in diamond, yield optimization of bulk and nano-sized diamonds, study of the trapped electronic structure, and fast qubit control are discussed in detail.

For optimization of the NV centers yield, maximum production recipe of the NV centers in bulk diamonds are found by both experiments and simulation: implantation at a dose of 10 N/nm^2 and annealing temperature beyond 850℃ would give the maximum yield. For best magnetic sensitivity, the optimum dose of nitrogen implantation is found to be 0.4 N/nm^2 with anneal temperature beyond 1000℃. It can also be concluded that hot irradiation/implantation at temperature above 1000℃ should lead to better magnetic sensitivity than room temperature irradiation/implantation followed by 1000℃ annealing. In addition, the enhancement of optical performance and size reduction of the NV centers in nanocrystals via air oxidation at 600℃ is demonstrated.

For diamond electron-trap characterization, we studied the optical quenching and recovery of photocurrent in a bulk type IIA single-crystal diamond. We found that the pulsed laser excited photocurrent shows optical quenching of photocurrent up to 90% when a CW laser is applied. In addition, the quenched photocurrent recovers after removing the CW laser and the photocurrent-time recovery curve fits to a stretched exponential curve. The recovery characteristic time depends on external bias voltage, the CW light intensity, and the wavelength. From these data we propose a model to explain the photocurrent quenching phenomena that a pulsed laser excites both the P1 centers and the trap, whereas the CW laser only pumps the P1 centers to the trap. The study of the optical quenching of photocurrent provides valuable information about the charge-trap mechanism in diamonds.

For precise and fast spin control, we have designed a novel method for precise spin qubit rotations in the strong driving regime where the standard pulses are not applicable. We report an experimental implementation of a control method based on quantum optimal control theory which does not suffer from such restriction. We demonstrate the most commonly used single qubit rotations, i.e.π 2- and π-pulses, beyond the RWA regime with high fidelity $F_{\pi/2}^{exp} = 0.95$ and $F_{\pi}^{exp} = 0.99$, respectively. They are in excellent agreement with the theoretical prediction. Furthermore, we perform two basic magnetic resonance experiments both in the rotating and the laboratory frames, where we are able to deliberately 'switch' between the frames, to confirm the robustness of our control

method. Our method is general, hence it may immediately find its wide applications in magnetic resonance, quantum computing, quantum optics, and broadband magnetometry.

In summary, these approaches promise to significantly speed up the development of diamond application such as quantum imaging, bio-sensing, photoelectric, and quantum computation which makes diamonds the most interesting candidate for quantum engineering.

REFERENCES

[1] S. Inwood. *The Forgotten Genuis: The Biography of Robert Hooke 1635- 1703* (MacAdam, San Francisco,2003)

[2] G. Binnig, C. F. Quate, C. Gerber, Phys. Rev. Lett. **56**, 930 (1986)

[3] R. C. Jaklevic, J. Lambe, A. H. Silver, and J. E. Mercereau. Phys. Rev. Lett. **12**, 159 (1964)

[4] A. Gruber, A. Drabenstedt, C. Tietz, L. Fleury, J. Wratchtrup, and C. von Borczyskowski, Science **276**, 2012 (1997)

[5] D. Budker and M. Romalis, Nature Physics **3**, 227 (2007)

[6] F. Dolde, H. Fedder, M. W. Doherty, T. Nöbauer, F. Rempp, G. Balasubramanian, T. Wolf, F. Reinhard, L. C. L. Hollenberg, F. Jelezko & J. Wrachtrup, Nature Physics **7**, 459 (2011)

[7] Ovartchaiyapong, K. W. Lee, B. A. Myers & A. C. Bleszynski Jayich, Nature Communications **5**, 4429 (2014)

[8] G. Kucsko, P. C. Maurer, N. Y. Yao, M. Kubo, H. J. Noh, P. K. Lo, H. Park & M. D. Lukin, Nature **500**, 54 (2013)

[9] S. Arroyo-Camejo, M. Adam, M. Besbes, J. Hugonin, V. Jacques, J. Greffet, J. Roch, S. W. Hell, and F. Treussart, ACS Nano **7**, 10912 (2013)

[10] E. H. Chen, O. Gaathon, M. E. Trusheim, and D. Englund, Nano Lett. **13**, 2073 (2013)

[11] M. Pfender, N. Aslam, G. Waldherr, P. Neumann, and J. Wrachtrup, Proc. Natl. Acad. Sci. U.S.A. **111**, 14669 (2014)

[12] P. Neumann, J. Beck, M. Steiner, F. Rempp, H. Fedder, P. R. Hemmer, Jörg Wrachtrup, Fedor Jelezko, Science **329**, 542 (2010)

[13] L. Childress, J. M. Taylor, A. S. Sørensen, and M. D. Lukin, Phys. Rev. Lett. **96**, 070504 (2006)

[14] A. Beveratos, R. Brouri, T. Gacoin, A. Villing, J. Poizat, and P. Grangier, Phys. Rev. Lett. **89**, 187901 (2002)

[15] G. Davies and M. F. Hamer, Proc. R. Soc London. A **348**, 285 (1976)

[16] S. J. Yu, M. W. Kang, H. C. Chang, K. M. Chen, and Y. C. Yu, J. Am. Chem. Soc **127**, 17604 (2005)

[17] J. R. Rabeau, A Stacey, A. Rabeau, S. Prawer, F. Jelezko, I. Mirza, and J. Wratchtrup, Nano Lett. **7**, 3433 (2007)

[18] S. Osswald, G. Yushin, V. Mochalin, S. O. Kucheyev, and Y. Gogotsi, J. Am. Chem. Soc **128**, 11635 (2006)

[19] V. Pichot, M. Comet, M. Fousson, C. Baras, A. Senger, F. Le Normand, and D. Spitzer, Diam. Relat. Mater. **17**, 13 (2008)

[20] S. Yugo, T. Kanai, T. Kimura, and T. Muto, Appl. Phys. Lett. **58**, 1036 (1991)

[21] International Diamond Laboratories. hpht- high pressure high temperature. Retrieved 2009, from http://www.diamondlab.org/80-hpht_synthesis.htm

[22] K. Iakoubovskii, M. V. Baidakova, B. H. Wouters, A. Stesmans, G. J. Adriaenssens, A. Ya. Vul' and P. J. Grobet, Diam. Relat. Mater. **9**, 861 (2000)

[23] M. E. Levinshtein, S. Rumyantsev, M. Shur, *Handbook series on semiconductors parameters*, *vol. 1*. (World Scientific, Singapore,1996)

[24] M. E. Levinshtein, S. Rumyantsev, M. Shur, *Properties of advanced semiconductor materials: GaN, A1N, InN, BN, SiC, SiGe,* (John Wiley & Sons, Hoboken, 2001)

[25] E. Rohrer, C.F.O. Graeff, C.E. Nebel, M. Stutzmann, H. Giittler, R. Zachai, Mater. Sci. Eng., B **46**, 115 (1997)

[26] G. Davies, S.C. Lawson, A.T. Collins, A. Mainwood, S.J. Sharp, Phys. Rev. B **46**, 13157 (1992)

[27] J.K. Kirui, J.A. van Wyk, M.J.R. Hoch, Diam. Rel. Mat. **8**, 1569 (1999)

[28] A.T. Collins, A. Dahwich, Diam. Rel. Mat. **13**, 1959 (2004)

[29] B. Naydenov, F. Reinhard, A. Lämmle, V. Richter, R. Kalish, U. F. S. D'Haenens Johansson, M. Newton3, F. Jelezko1 and J. Wrachtrup, Appl. Phys. Lett. **97**, 242511 (2010)

[30] T. Gaebel, M. Domhan, C. Wittmann, I. Popa, F. Jelezko, J. Rabeau, A. Greentree, S. Prawer, E. Trajkov, P. R. Hemmer and J. Wratchtrup, Appl. Phys. B **82**, 243

(2006)

[31] F. Jelezko and J. Wrachtrup, J. Physics.: Condens. Matter **18**, 807 (2006).

[32] J. R. Rabeau, P. Reichart, G. Tamanyan, D. N. Jamieson, S. Prawer, F. Jelezko, T. Gaebel, I. Popa, M. Domhan, and J. Wrachtrup, Appl. Phys. Lett. **88**, 023113 (2006)

[33] X. Chen, B. Henderson and K. P. O'Donnell, Appl. Phys. Lett. **60**, 2672 (1992)

[34] R. Chen, J. Lumin. **102–103**, 510 (2003)

[35] J. Koike, D. M. Parkin, and T. E. Mitchell, Appl. Phys. Lett. **60,** 12 (1992)

[36] X. J. Hu, Y. B. Dai, R. B. Li, H. S. Shen, and X. C. He, Solid State Commun. **122,** 45 (2002)

[37] A. Mainwood, Phys. Rev. B **49**, 7934 (1994)

[38] C. Uzan-Saguy, C. Cytermann, R. Brener, V. Richter, M. Shaanan, and R. Kalish Appl. Phys. Lett. **67**, 1194 (1995)

[39] R.C. Burns, Vesna Cvetkovic, C. N. Dodge, D. J. F. Evans, Marie-Line T Rooney, P. M. Spear, and C. M. Welbourn, J. Cryst. Growth **104**, 257 (1990)

[40] V.M. Acosta, E. Bauch, M. P. Ledbetter, C. Santori, K.-M. C. Fu, P. E. Barclay, R. G. Beausoleil, H. Linget, J. F. Roch, F. Treussart, S. Chemerisov, W. Gawlik, and D. Budker, Phys. Rev. B **80**, 115202 (2009)

[41] K. Iakoubovskii, S. Dannefaer, and A. Stesmans, Phys. Rev. B **71**, 233201 (2005)

[42] G. Davies, S. C. Lawson, A. T. Colins, A. Mainwood, and S. J. Sharp, Phys. Rev. B **46**, 13157 (1992)

[43] G. Davies, Physica B **273/274**, 15 (1999)

[44] K. Iakoubovskii, I. Kiflawi, K. Johnston, A. Collins, G. Davies, and A. Stesmans, Physica B **340/342**, 67 (2003)

[45] J. Kiprono (2008). Unpublished doctoral dissertation, University of Witwatersrand, Johannesburg, Gauteng, South Africa

[46] A.T. Collins, New Diamond Front. Carbon Technol. **17**, 47 (2007)

[47] J.M. Baker, Diam. Relat. Mater. **16**, 216219 (2007)

[48] R.Alleaume, F. Treussart, G.Messin,Y.Dumeige, J.F.Roch,A. Beveratos,R. Brouri Tualle, J.P. Poizat, P. Grangier, New J. Phys. **6** , 92 (2004)

[49] N. Mohan, Y.K. Tzeng, L. Yang, Y.Y. Chen, Y.Y. Hui, C.Y. Fang, H.C. Chang, Adv. Mater. **22**, 843 (2010)

[50] G. Balasubramanian, I. Chan, R. Kolesov, M. Al-Hmoud, J. Tisler, C. Shin, C. Kim, A. Wojcik, P. Hemmer, A. Krueger, T. Hanke, A. Leitenstorfer, R. Bratschitsch, F. Jelezko, J. Wrachtrup, Nature **455**, 648 (2008)

[51] J. Maze, P. Stanwix, J. Hodges, S. Hong, J. Taylor, P. Cappellaro, L. Jiang, M. Dutt, E. Togan, A. Zibrov, A. Yacoby, R. Walsworth, M. Lukin, Nature **455**, 644 (2008)

[52] E. Rittweger, K.Y. Han, S.E. Irvine, C. Eggeling, S.W. Hell, Nat. Photonics **3**, 144 (2009)

[53] P.C. Maurer, J.R. Maze, P.L. Stanwix, L. Jiang, A.V. Gorshkov, A.A. Zibrov, B. Harke, J.S. Hodges, A.S. Zibrov, A. Yacoby, D. Twitchen, S.W. Hell, R.L. Walsworth, M.D. Lukin, Nat. Phys. **6**, 912 (2010)

[54] P. Neumann, R. Kolesov, B. Naydenov, J. Beck, F. Rempp, M. Steiner, V. Jacques, G.Balasubramanian, M. Markham, D. Twitchen, S. Pezzagna, J. Meijer, J. Twamley, F. Jelezko, J. Wrachtrup, Nat. Phys. **6**, 249 (2010)

[55] P. Neumann, N. Mizuochi, F. Rempp, P. Hemmer, H.Watanabe, S. Yamasaki, V. Jacques, T. Gaebel, F. Jelezko, J. Wrachtrup, Science **320**, 1326 (2008)

[56] A. Kruger, F. Kataoka, M. Ozawa, T. Fujino, Y. Suzuki, A.E. Aleksenskii, A.Y. Vul, E. Osawa, Carbon **43**, 1722 (2005)

[57] C.L. Cheng, H.C. Chang, J.C. Lin, K.J. Song, J.K. Wang, Phys. Rev. Lett. **78**, 3713 (1997)

[58] O.A. Williams, J. Hees, C. Dieker, W. Jager, L. Kirste, C.E. Nebel, ACS Nano **4**, 4824 (2010)

[59] S. Osswald, G. Yushin, V. Mochalin, S. Kucheyev, Y. Gogotsi, J. Am. Chem. Soc. **128**, 11635 (2006)

[60] B.R. Smith, D.W. Inglis, B. Sandnes, J.R. Rabeau, A.V. Zvyagin, D. Gruber, C.J. Noble, R. Vogel, E. Osawa, T. Plakhotnik, Small **5**, 1649 (2009)

[61] C. J. Chu, C. Pan, J. L. Margrave, and R. H. Hauge, Diam. Relat. Mater. **4**, 1317 (1995)

[62] M. Wolfer, J. Biener, B. S. El-dasher, M. M. Biener, A. V. Hamza, A. Kriele, and C. Wild, Diam. Relat. Mater. **18**, 713 (2009)

[63] T. Yamada, A. Sawabe, S. Koizumi, J. Itoh and K. Okano, Appl. Phys. Lett. **76**, 1297 (2000)

[64] D. H. Douglas-Hamilton, E. D. Hoag, and J. R. M. Seitz, J. Opt. Soc. Am. **64**, 36 (1974)

[65] J. Bohon, E. Muller, and J. Smedley, J. Synchrotron Radiat. **17**, 711 (2010)

[66] E. Rohrer, C.E. Nebel, M. Stutzmanna, A. Flöter, R. Zachai, X. Jiang, C.-P. Klages, Diam. Relat. Mater. **7**, 879 (1998)

[67] T. H. Taminiau, J. Cramer, T. van der Sar,   V. V. Dobrovitski   & R. Hanson, Nat. Nanotechnol. **9**, 171 (2014)

[68] F. Dolde, V. Bergholm, Y. Wang, I. Jakobi, B. Naydenov, S. Pezzagna, J. Meijer, F. Jelezko, P. Neumann, T. Schulte-Herbrüggen, J. Biamonte & J. Wrachtrup, Nat. Commun. **5**, 3371 (2014)

[69] J. Scheuer, Xi Kong, R. S. Said, J. Chen, A. Kurz, L. Marseglia, J. Du, P. R. Hemmer, S. Montangero, T. Calarco, B. Naydenov and F. Jelezko, New J. Phys. **16**, 093022 (2014)

[70] H. Bernien, L. Childress, L. Robledo, M. Markham, D. Twitchen, and R. Hanson, Phys. Rev. Lett. **108**, 043604 (2012)

[71] N. Mizuochi, T. Makino, H. Kato, D. Takeuchi, M. Ogura, H. Okushi, M. Nothaft, P. Neumann, A. Gali, F. Jelezko, J. Wrachtrup & S. Yamasaki, Nat. Photonics **6**, 299 (2012)

[72] A. Brenneis, L. Gaudreau, M. Seifert, H. Karl, M. S. Brandt, H. Huebl, J. A. Garrido, H. L. KoppensFrank, A. W. Holleitner, Nat. Nanotechnol. **10**, 135 (2015)

[73] J. A. Elmgren and D. E. Hudson, Phys. Rev. **128**, 1044 (1962)

[74] R. G. Farrer and L. A. Vermeulen, J. Phys. C: Solid State Phys. **5**, 2762 (1972)

[75] K. J. Quintero, S. Antipov, A. V. Sumant, C. Jing, and S. V. Baryshev, Appl. Phys.

Lett. **105**, 123103 (2014)

[76] M. Liao, Xi Wang, T. Teraji, S. Koizumi, and Y. Koide, Phys. Rev. B **81**, 033304 (2010)

[77] M. Liao, Y. Koide, J. Alvarez, M. Imura, and J. Kleider, Phys. Rev. B **78**, 045112 (2008)

[78] D. J. Twitchen, M. E. Newton, J. M. Baker, T. R. Anthony and W. F. Banholzer, J. Phys. Condens. Mat. **13**, 2045 (2001)

[79] M. I. Landstrass and K. V. Ravi, Appl. Phys. Lett. **55**, 975 (1989)

[80] F. J. Heremans, G. D. Fuchs, C. F. Wang, R. Hanson and D. D. Awschalom, Appl. Phys. Lett. **94**, 152102 (2009)

[81] X. Chen, B. Henderson and K. P. O'Donnell, Appl. Phys. Lett. **60**, 2672 (1992)

[82] R. Chen, J. Lumin. **102–103**, 510 (2003)

[83] J. O. Karolin and C. D. Geddes, J. Fluoresc. **22**, 1659 (2012)

[84] E. Bourgeois, A. Jarmola, M. Gulka, J. Hruby, D. Budker, M. Nesladek, "Photoelectrical detection of electron spin resonance of nitrogen-vacancy centres in diamond", http://arxiv.org/abs/1502.07551

[85] J. Wrachtrup and F. Jelezko, J. Phys.: Condens. Matter **18**, S807 (2006)

[86] G. Balasubramanian, P. Neumann, D. Twitchen,M. Markham, R. Kolesov, N. Mizuochi, J. Isoya,J. Achard, J. Beck, J. Tissler, et al., Nat Mater **8**, 383(2009)

[87] J. M. Taylor, P. Cappellaro, L. Childress, L. Jiang,D. Budker, P. R. Hemmer, A. Yacoby, R. Walsworth,and M. D. Lukin, Nat. Phys. **4**, 810 (2008)

[88] G. Waldherr, J. Beck, P. Neumann, R. S. Said,M. Nitsche, M. L. Markham, D. J. Twitchen, J. Twamley,F. Jelezko, and J. Wrachtrup, Nat. Nano. **7**, 105 (2012)

[89] P. Neumann, N. Mizuochi, F. Rempp, P. Hemmer,H. Watanabe, S. Yamasaki, V. Jacques, T. Gaebel,F. Jelezko, and J. Wrachtrup, Science **320**, 1326 (2008)

[90] P. Neumann, et al., Nat. Phys. **6**, 249 (2010)

[91] G. D. Fuchs, V. V. Dobrovitski, D. M. Toyli, F. J. Here-mans, and D. D. Awschalom, Science **326**, 1520 (2009)

[92] M. Wubs, Chem. Phys. **375**, 163 (2010)

[93] P. Doria, T. Calarco, and S. Montangero, Phys. Rev.Lett. **106**, 190501 (2011).

[94] T. Caneva, T. Calarco, and S. Montangero, Phys. Rev. A **84**, 022326 (2011).

[95] R. S. Said and J. Twamley, Phys. Rev. A **80**, 032303(2009).

[96] A. Gruber, A. Drabenstedt, C. Tietz, L. Fleury,J. Wrachtrup, and C. von Borczyskowski, Science **276**, 2012 (1997).

[97] F. Jelezko, T. Gaebel, I. Popa, A. Gruber, andJ. Wrachtrup, Physical Review Letters **92**, 076401(2004).

[98] M.A.Nielsen and I.L.Chuang, *Quantum computation and quantum information* (Cambridge University Press, Cambridge,2000).

[99] U. Boscain and P. Mason, Journal of Mathematical Physics **47**, 062101 (2006).

[100] W. H. Gränicher, *Messung Beendet—was Nun?: Einführung und Nachschlagewerk für die Planung und Auswertung von Messungen* (Vieweg+Teubner Verlag, Wiesbaden, 1996)

[101] C. Slichter, *Principles of Magnetic Resonance* (Springer Science & Business Media, Berlin, 1996).

[102] A. Schweiger and G. Jeschke, *Principles of Pulse Electron Paramagnetic Resonance* (Oxford University Press, Oxford, 2001).

[103] E. L. Hanh, Phys. Rev. **80**, 580 (1950).